UNIVERSITY OF BIRMINGHAM

Thesis -

Thermometry and Thermodynamics within an Ultracold Mixture of ^{87}Rb and ^{41}K

Thomas Hewitt

September 2024

Abstract

Within this work, I put forward my experimental studies of the interactions in ultracold atomic mixtures, and their applications in quantum thermodynamics. I detail the key features and the progress made towards building a system which is capable of cooling quantum gases to absolute zero. In order to quantify the heat exchange of a system, knowledge of its temperature is required. Precise temperature measurements of systems with low numbers of ultracold atoms are of great importance in quantum technologies, but they can be quite resource intensive. We first utilised the experimental system to develop an adaptive Bayesian strategy, which processes data from both real and simulated release-recapture thermometry experiments of a single atom of ^{41}K in an optical tweezer at microkelvin temperatures. By adaptively choosing the release-recapture times, this strategy produces more reliable estimates, while converging faster to the real temperature compared to conventional methods. A simpler, non-adaptive *a priori* method produced competitive results when applied to real experimental data. In addition to this, the underlying Bayesian framework is not specific to our platform and can be adapted for various experiments. Following this, I move onto the studies of a quantum impurity system, which involved immersing the single atom in a bath of ultracold ^{87}Rb atoms. The K atom is trapped within a species-selective dipole potential, allowing for independent manipulation of the bath and impurity. I explore the characterisation and control of the interactions between the two subsystems. This was performed using Feshbach spectroscopy, where I detected several interdimensional confinement induced Feshbach resonances for the KRb interspecies scattering length. In addition to the

underlying free-space s-wave interactions, I detected a series of p-wave resonance features. I further determine how the resonances behave as the temperature of the bath and the dimensionality of the interactions change. Finally, I was able to screen the quantum impurity by tuning the wavelength of the species-selective tweezer, which adds another tool for control of the system. These results have a range of applications in quantum simulations of quantum impurity models and quantum thermodynamics.

Acknowledgements

To begin this thesis, I would like to extend my thanks to the multitude of people who have helped me throughout my PhD. Whether academically or through moral support, they mean a great deal to me.

I would first like to thank my supervisor Giovanni, who I would not be doing my PhD without. I have learnt a great deal about cold atoms and how to run a beast of an experiment due to his guidance. I'd next like to thank Jorge, who first inspired me to do my PhD and guided me throughout the first few months of my research by teaching me all the tricks of the machine. Throughout my PhD I have collaborated with many different people on different projects and would like to thank them for their time and assistance. This includes the two postdocs who assisted me directly with the experiment, Manan and Rahul. Others who lent a helping hand include Eric, whose experimental expertise was matched only by his singing ability, Anna, who knew these types of experiments inside and out, and Tom B who came all the way from France and provided much needed support over the course of the few months he was here. I was also lucky enough to collaborate with various other researchers to produce a couple of publications. I would like to thank the team from the University of Exeter, including Jonas, Jesus and Luis, where we worked together on single atom thermometry. I was even lucky enough to attend a couple of conferences with them to discuss these subjects in person. I also thank Yusuke from the Tokyo Institute of Technology on our paper regarding a single atom impurity.

Now, I'd like to thank the people I spent most of the time of my PhD with, they helped a great deal to stop me from going crazy in the lab. First is Aaron for keeping the lab livelier and being a reliable source of knowledge. Thanks to Tom E, who is so similar to me that a Stern-Gerlach experiment is required to differentiate us. Sym and James, thanks for keeping me sane at the end of my PhD and bringing some much-needed energy to the lab.

Next, I want to thank the PhD students from the rest of the Quantum Matter department. We certainly had some interesting and heated conversations at lunch, some exciting evenings out, and even went on some wonderful mental health holidays to Center Parcs. To Tabatha, my first pick for a quiz team, we certainly had a lot of experiences to vent about, from undergraduate to PhD. To Joe N, from Birmingham as well as my lab next door neighbour, and Joe K, my slime, pro dieter and detective, our trip to the YAO conference in Barcelona is probably the highlight of my PhD. To Stuart, an honorary member of our department, who always made the conversations at lunch far livelier. I'd like to also thank Jake, a fellow rogue-like liker and voice of reason, Joe B, who has given PhD students a voice and always has an interesting story to tell, and Caleb, a go to whenever I want to obsess over one of our hobbies. To Kostas, who may not have been the department long, but certainly left a huge impact. To Nat and Tom B, you may be newbies now, but you'll soon be the most senior PhD students in the department, so good luck with the rest of your PhDs. Also, thanks to Ellie and Carlton, you always had solid knowledge when I needed help.

Now I move onto a few non-Physics friends who helped tremendously in keeping me going. I'd like to thank Tom G, who's been there throughout the entire thesis writing process, your support has been invaluable. I'd also like to thank Fraser, Jacob, Jake, Dylan, Jack, Nyna and Misha who are friends I greatly enjoy spending time with, and generally make my weeks more exciting. I'd like to thank Gerda for putting a roof over my head and putting up with me for four years, you've cooked some of the best food I've ever eaten. Also, thanks to Orneste, we spent some very interesting years living together, from raising two sets of

kittens to some nerve-wracking driving experiences.

Last, but by no means least, I'd like to thank my parents, Gary and Clare, and my siblings, Sam and Emily, for their unending support throughout my PhD and the rest of my life. I don't think I would have achieved as much without them, and they've always been there when I needed them.

Contents

List of Figures

List of Tables

List of Acronyms

AOM Acousto-Optical Modulator

BEC Bose-Einstein Condensate

LASER Light Amplification by Stimulated Emission of Radiation

MOT Magneto-Optical Trap

PBS Polarisation Beam Splitter

PID Proportional-Integral-Differential

SST Species-Selective Tweezer

TA Tapered Amplifier

Chapter 1

Introduction

Throughout the last few decades, there has been a fixation in the shrinking of pre-existing technologies, with fields such as astronomy, biology and nanoscale physics looking to greatly benefit from such devices. We are now in an age in which we can start to work at the quantum level, in part thanks to advances in atomic physics, due to the ability to manipulate systems at the single atom level [1].

At the cutting edge is the study of thermodynamics at the quantum level, which necessitates changing our definitions of temperature, heat and work from those in the classical regime. I choose to focus on the area of quantum engines, which are pivotal in helping us understand quantum thermodynamics. In these systems, quantum information is produced by the controlled exchange of heat with the environment.

So far, most current studies have been purely theoretical [2–8], but my aim was to expand into the experimental domain as coherent quantum engines can generate substantially more power than stochastic ones [9]. Many studies have been performed by employing non-thermal or non-classical baths, which exhibit more efficient regimes and more powerful engines compared to the classical case [10–14]. Recent experimental examples closely related to my work include a non-thermal heat engine exploiting the BEC-BCS crossover [15], and

a quantum heat engine that demonstrates an Otto cycle using a single-ion [16].

In contrast to the previous examples, I worked to create a single atom quantum heat engine, wherein an atom is trapped at low enough temperatures in order for quantum effects to arise. I chose ultracold atomic mixtures as the platform of study, as this allows for the high control and flexibility required to realise the different thermodynamic transformations and subsequent cycles.

In order to inspect the properties of a quantum heat engine, one key parameter that needs to be monitored is the temperature of the system. Precise low-temperature thermometry is a very important tool for cold atom based quantum technologies. For my particular experiment this includes the study of thermalisation in closed quantum systems [17–19] with research moving towards the realisation of thermodynamic cycles [6, 8, 20]. The most common technique used to determine the temperature of cold atom samples is time of flight imaging, but this is not particularly useful when using optical tweezers, where only a few atoms are independently trapped [21–25]. In my research, I opted for the release-recapture thermometry technique [26–28] for the atoms in the tweezer. The main disadvantage of this method is that it requires numerous experimental repetitions to produce an accurate result, taking a large amount of time to collect data.

On the more theoretical side, the application of estimation-theoretic methods to low-temperature thermometry has been consolidated into the field of quantum thermometry [29, 30]. Most of the existing literature on quantum thermometry relies on *local* estimation theory, and adopts the (quantum) Fisher information $\mathcal{F}$ as the main parameter to be maximised [31]. For the ideal case (in the asymptotic limit of a large number of measurements i.e., $\mu \to \infty$), and for unbiased estimators, $\mathcal{F}$ controls the scaling of the signal-to-noise ratio of temperature estimates, as per $(T/\delta T)^2 \sim \mu \mathcal{F} T^2$. This is not the case for the experimental scenario, as you are limited to a *finite* number of measurements. Limited to tens or hundreds of shots, $\mathcal{F}$ is unlikely to capture the behaviour of optimal temperature estimates. A solution

to this is to employ a more general Bayesian framework [32–34].

Prior to this work, several experimental proposals had been put forward within quantum thermometry [19, 35–39], but the field is still mostly theoretical and more concerned with setting precision bounds [30]. The goal of my work was to take a more practical approach and exploit the theory to process my own experimental data. I adopt a Bayesian framework that provides precision bounds as in estimation theory, and also allows for the construction of optimal estimators from the outcomes of the measurements I take [40].

Following this, when attempting to construct the strokes of a quantum heat engine using quantum thermodynamic transformations, I realised many complexities arose due to the dimensionality of the system. This then lead me to treat the system as a quantum impurity system, with the following text taken from my publication in [41]. A quantum impurity system is composed of a subsystem with a few degrees of freedom, the *impurity*, interacting with a larger subsystem with potentially infinite degrees of freedom, the *bath*. This class of systems is represented by the three-term Hamiltonian

$$H = H_I + H_B + H_{IB}, \tag{1.1}$$

where H_I and H_B are the impurity and bath Hamiltonians respectively, with H_{IB} describing the coupling between the impurity and the bath. In general, $[H_I, H_{IB}] \neq 0$. Several fundamental quantum mechanical models are based on this apparently simple construction, the most celebrated being the Anderson impurity model [42, 43], the Kondo model [44, 45] and the spin-boson model [46], whose impact and ramifications range from condensed matter physics to quantum information physics, the physics of open quantum systems, and even down to the very foundations of quantum mechanics. In the context of quantum technology, quantum dots are a prominent example of quantum impurity systems [47, 48], while cold atoms have been instrumental in implementing quantum simulators for quantum impurity models and their extensions [49–55].

In quantum information science, significant efforts are taken to shield a quantum system, for example a qubit, from the environment. This helps to reduce unwanted effects such as decoherence and dephasing. If properly controlled and tamed, however, the interaction of a quantum system with the environment, as embodied by H_{IB}, can be a powerful resource. For example, controlling the interaction of qubits with the environment could lead to the realization of environmental dark states [56, 57] and environmental resilient quantum information protocols [58–60]. The control of the interaction between a quantum system and a bath is a central ingredient in quantum thermodynamics [61] and for the realization of quantum engines, like those mentioned above.

Cold atom technology provides us with a large set of tools to engineer and control the three terms in Equation 1.1. In particular, optical tweezers and optical lattices allow us to confine the motion of ultracold atoms to a few degrees of freedom [24, 62–64], mesoscopic traps can be used to control the density and temperature of the atoms in an ultracold bath, and Feshbach resonances enable the control of the interactions [65, 66]. Here, I combine all these elements and realize a cold atom quantum impurity architecture by trapping a single K atom in an optical tweezer, and immersing it in a bath of Rb atoms at ultracold temperatures. To obtain the selective trapping of the K atom, I utilise a species-selective tweezer (SST), whose wavelength is tuned at the so-called tune-out wavelength for Rb, so that it is almost transparent for this atomic species [67, 68].

1.1 Thesis Outline

At the beginning of my studies, I became fully responsible for the experimental setup seen in [69]. I initially worked with the previous researchers as a summer student to collect data and publish the work seen in [70]. I learned the basics of the experiment and how to operate it over several months. At the time of my joining, the experiment was capable of producing

an all-optical Bose-Einstein Condensate (BEC) of ^{87}Rb, alongside a Magneto-Optical Trap (MOT) for ^{39}K and ^{41}K. In the first few months of my work I overhauled the laser system for Rb and K, replacing old optical equipment and lasers, which greatly increased the stability of the system.

Moving on from this, I implemented and characterised an optical tweezer, capable of trapping K atoms. A great deal of work was required to align it with the rest of the system, refine its properties, such as its waist, in order for it to trap only a single ^{41}K atom, and also build the setup necessary to image it.

In collaboration with the University of Exeter, we developed an adaptive Bayesian strategy [71] in order to obtain faster and more reliable temperature estimates of the single atom. We initially found in the current system that release-recapture thermometry took a great deal of time. This made thermalisation measurements, which require many temperature measurements, an even larger time sink. This research went a long way to help with that.

The next area I wished to explore were the interactions between an ultracold bath of ^{87}Rb and a single atom of ^{41}K. In order to do this, I would first need to polarise both atoms into the $|F = 1, m_F = 1\rangle$ substate. So a setup was built to pump the K atoms into this state using the D_1 line. Alongside this, I installed a nanopositioner to the optical tweezer setup. For the rest of my studies, I explored the interactions detailed later in the thesis, discovering that the system was more complex than I first thought [41]. Meaning the goal of creating a single atom quantum heat engine, was further away, yet not completely out of reach.

All of these subjects are discussed in further details throughout this thesis. With the structure of the chapters as follows:

- **Chapter 2 - Background Theory:** In this chapter, I explain the theory required to understand the novel aspects of my work. I first describe the theory regarding the interactions in a system consisting of two different atomic species at different temper-

atures. I then move onto Feshbach resonances, one of the key areas of exploration for this study, and how confinement induced resonances arise when the dimensionality of the system changes. I then discuss the theory surrounding the realisation of a single atom quantum heat engine, which includes the comparison between classical and quantum thermodynamics, and how I can construct the quantum thermodynamic transformations within the experiment. I finally lay out the theory required to understand our specific Bayesian thermometry, which is used to estimate the temperature of a single atom trapped within an optical tweezer.

- **Chapter 3 - Experimental Setup:** In this chapter, I display my experimental setup which I adapted from a pre-existing system, and almost completely overhauled in the process. I describe the myriad of improvements made to the system, which helped facilitate my experiment. This includes parameters and schematics of the vacuum system, the laser system designed to cool and trap the atoms, and the imaging techniques used to observe the atoms.

- **Chapter 4 - The Building Blocks for a K-Rb Mixture:** In this chapter, I lay out the base atomic elements used within the experiment. I expand upon the previous work carried out on how to cool and characterise the two key atomic species. The first of which is an all optical BEC of Rubidium atoms, starting from room temperature down to the ultracold regime. The other is a dark MOT of Potassium atoms, which relies on similar principles to Rb.

- **Chapter 5 - Single Atom in a Tweezer:** This chapter goes into detail about what is required to create a single atom quantum heat engine, comparing them to their classical analogues. It then describes how the optical tweezer was implemented, alongside its properties, which include the ideal wavelength and the heating rates for each species. I then explain how I achieve the trapping of a single K atom, utilising the collisional blockade mechanism. I then discuss how the single atom is imaged, and

how I characterise it.

- **Chapter 6 - Single Atom Thermometry:** This chapter explains how we developed an adaptive Bayesian thermometry enhancing a release recapture method to help measure the temperature of the single atom trapped in an optical tweezer. I show how the performance of the adaptive method compares to other less involved methods using both simulated and real data taken with my experimental system.

- **Chapter 7 - Controlling the Interactions in a Cold Atom Quantum Impurity System:** This chapter details my exploration of the interactions between a single K atom and an ultracold cloud of Rb atoms. It details how the dimensionality of the system, external magnetic field and wavelength of the optical tweezer can all be used to control the interactions.

Chapter 2

Background Theory

In this chapter, I will describe the theory required to understand the rest of this thesis. As I inherited the experiment from the previous researchers, and have continued to reach for similar goals, the following theoretical ideas contain a similar structure and some overlap of the work seen in [69]. This chapter contains the following sections:

- **Section 2.1** introduces the theory regarding the single atom quantum heat engine. It first describes the key components of a single atom quantum heat engine, and compares them to the classical analogues. It then compares how the quantum case relates to the classical one in terms of the exchange of heat and work. These combine to explain the four key quantum thermodynamic transformations.

- **Section 2.2** describes Feshbach resonances, the tunable interactions I use to transform how the quantum mixture interacts. It also describes how a change in dimensionality of the system can give rise to confinement induced resonances.

- **Section 2.3** contains the theory regarding collisions between a single ^{41}K atom and an ultracold bath of ^{87}Rb atoms. It details the different loss mechanisms and how the single atom will thermalise when in contact with the bath.

- **Section 2.4** introduces the Bayesian-global paradigm used to improve the temperature estimates in a release-recapture thermometry experiment.

2.1 Single Atom Quantum Heat Engine

2.1.1 Components of a Single-Atom Quantum Heat Engine

For us to be able to understand the basics of a quantum heat engine, it is important to introduce the analogues between a classical and quantum engine. These are:

- **Working fluid** - several different thermodynamic transformations are performed on the working fluid. For our experiment, it is the single ^{41}K atom trapped in the optical tweezer.
- **Thermal bath** - this has to be large compared to the working fluid, so heat transfer between the two doesn't affect its temperature. This is an ultracold cloud of ^{87}Rb, which is cooled down to the quantum level using evaporative cooling. See Section 4.1 for further information.
- **Piston** - this drives some of the thermodynamic transformations of the working fluid. In our system the piston is the optical tweezer which is ideally species selective to only affect the working fluid and not the bath.
- **Tunable interactions** - we want to tune the interactions between the bath and the working fluid, which allows us to implement more thermodynamic transformations. For this, we use hetero-nuclear Feshbach resonances, see Section 2.2.

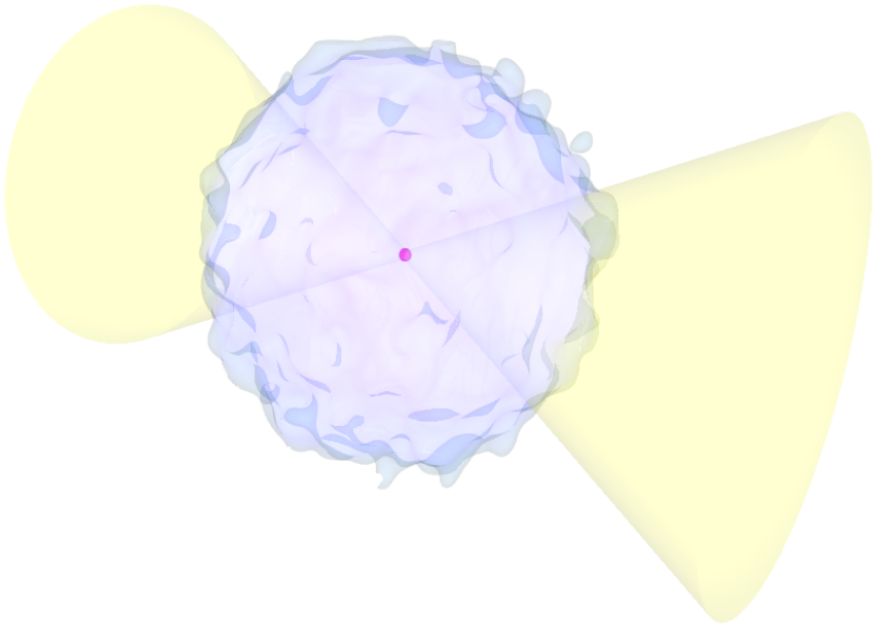

Figure 2.1: A pictorial representation of the proposed single atom heat engine system. The single atom (red sphere) is trapped within an optical tweezer (yellow beam) and is immersed in a bath of atoms of another species (blue cloud) [72].

2.1.2 From Classical to Quantum Thermodynamics

The single atom quantum heat engine consists of three basic elements, a single particle which is trapped in a harmonic oscillator, with frequency ω, immersed within a thermal bath [6]. Due to the trap being created by an optical tweezer, we can engineer the trap so that the transverse (radial) trapping frequencies set an energy scale which is much higher than the thermal one corresponding to the operating temperature, while the axial frequency energy scale is comparable to the thermal one. This allows us to operate in the quantum regime where the thermal energy is of the order of the energy corresponding to the harmonic oscillator $k_B T \simeq \hbar\omega$. This setup allows only the lower axial energy levels and the transverse ground state level to be occupied, leading to a one dimensional multi-level system on the axial degrees of freedom, with the transverse degrees of freedom considered frozen. This

means we can write the Hamiltonian for the system as, $H = \sum_n E_n|n\rangle\langle n|$ where $E_n < E_{n+1}$ and $|n\rangle$ are the eigenvalues and eigenvectors of the one-dimensional harmonic oscillator. For our quantum system, the quantised nth energy level E_n has an associated occupation probability P_n, this leads to the total energy of the system

$$U = \sum_n P_n E_n, \tag{2.1}$$

if we differentiate this, we obtain:

$$dU = \sum_n E_n dP_n + \sum_n P_n dE_n. \tag{2.2}$$

Equation 2.2 is a formulation of the first law of thermodynamics at the single atom level. We can display analogies to the classical formulation of heat and work, identifying the heat exchange $dQ = \sum_n E_n dP_n$ and the work exchange $dW = \sum_n P_n dE_n$. From these definitions, we can take the von Neumann entropy and reduce it to the thermal Shannon entropy:

$$S = -k_B \sum_n P_n \log P_n \tag{2.3}$$

Since we're using a single particle, we can reduce Bose and Fermi statistics to a Boltzmann probability distribution. As the single atom thermalises with the bath, the probability P_n, that the nth level is occupied follows $P_n = 1/Z\ e^{-E_n/k_B T}$, with Z being the partition function.

2.1.3 Thermodynamic Transformations at the Quantum Level

In order to achieve a quantum heat engine, the variables that define our system, P_n and E_n, need to be used to explain the various quantum thermodynamic transformations. The following descriptions address the different thermodynamic transformations.

The quantum adiabatic transformation requires the single atom and the bath to be

decoupled, which means that the magnetic field is tuned to use the zero crossing of the interspecies scattering length, the process can be seen in Section 2.2 below. The trapping potential is then varied, by changing the tweezer power, while satisfying $dP_n = 0$. This implies that there is no heat transfer, $dQ = 0$, between the bath and the single atom.

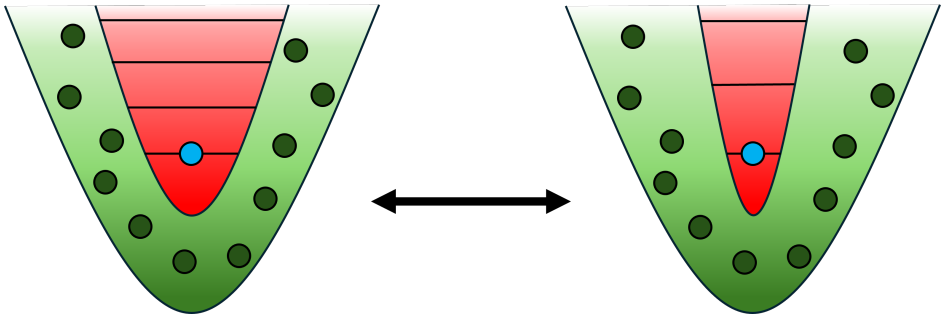

Figure 2.2: Depiction of the quantum adiabatic transformation. The blue particle represents a single K atom trapped in the tweezer, which is represented by the red area, with the horizontal lines representing the energy levels of the harmonic trap. The dark green particles represent the Rb atoms trapped within the optical dipole trap, which is represented by the light green background.

The quantum isothermal transformation needs both species to interact by turning on the interactions between the single atom and the bath. The tweezer trapping potential is varied, while the bath potential remains the same, leading to a constant temperature. This results in heat exchange between the single atom and the bath, at a constant temperature, while the spacing between the energy levels changes.

The quantum isochoric transformation preserves the volume of the system, meaning no work is done on the system, $dE_n = 0$. The single atom interacts with the bath while the bath temperature varies with time by adjusting its trapping potential, while the tweezer potential is kept constant. This results in a change in the occupation probability distributions $dP_n \neq 0$ and therefore $dS \neq 0$.

The quantum isobaric transformation keeps the pressure on the single atom constant. The single atom is in contact with the bath, and the temperature of the bath is changed

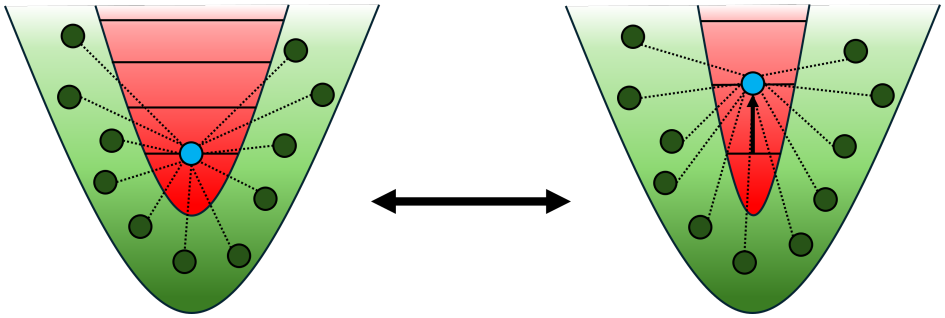

Figure 2.3: Depiction of the quantum isothermal transformation. The dashed lines represent the interaction between the Rb atoms and the single K atom.

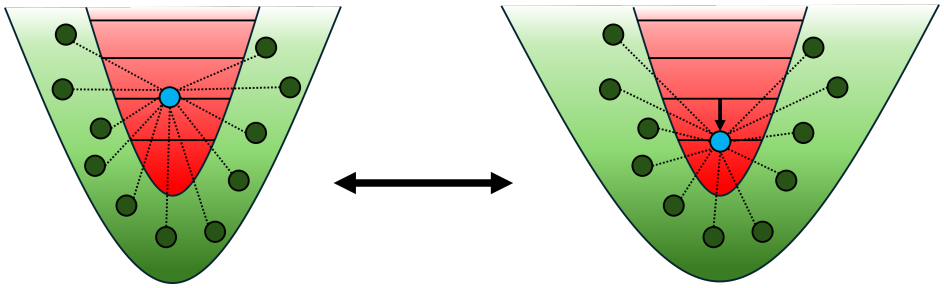

Figure 2.4: Depiction of the quantum isochoric transformation.

in combination with the trapping potential of the single atom. To explain this, we need to define the pressure equivalent in this system. In classical thermodynamics, the relation between the internal energy, U, and the pressure, P, is

$$P = -\left(\frac{\partial U}{\partial V}\right)_S . \tag{2.4}$$

Now replacing U, with the definition in Equation 2.2, we receive the quantum pressure

$$\Pi = -\sum_n P_n \left(\frac{dE_n}{da_{ho}}\right), \tag{2.5}$$

where a_{ho} is the harmonic oscillator length $a_{ho} = \sqrt{\hbar/m\omega}$. This treats the single atom trapped in the tweezer as a quantum harmonic oscillator with frequency ω and mass m.

Using

$$U = \sum_n P_n E_n = \sum \exp\left(-\frac{\beta}{\hbar\omega} E_n\right) E_n, \tag{2.6}$$

with $\beta = \hbar\omega/(k_B T)$, this yields

$$\Pi = \frac{\sqrt{\xi}\sinh\beta}{\cosh\beta - 1}, \tag{2.7}$$

with $\xi = hm\omega^3$. From Equation 2.7 it follows that, during an isobaric transformation, the temperature must be changed according to

$$\frac{\hbar\omega}{k_B T} = \ln\left(\frac{\Pi + \xi^{1/2}}{\Pi - \xi^{1/2}}\right). \tag{2.8}$$

This shows how it's possible to vary ξ and T to keep Π constant. T is changed arbitrarily, as the temperature of the bath can be varied by adjusting the trapping potential. We can change ξ by altering the trapping potential acting upon the single atom.

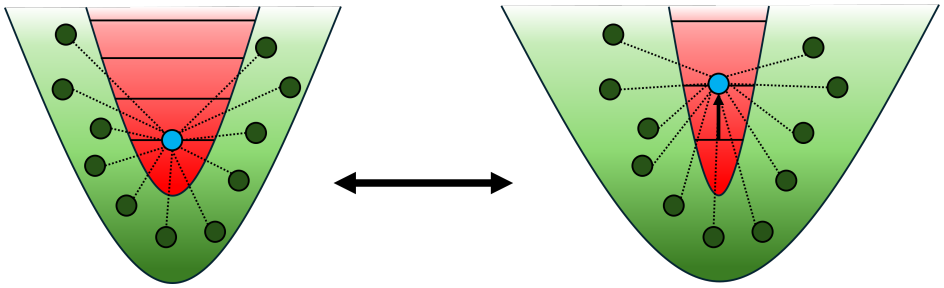

Figure 2.5: Depiction of the quantum isobaric transformation.

2.1.4 Quantum Engine Cycles

The quantum thermodynamic transformations described above can be implemented experimentally to create a quantum heat engine [6]. In the case of my experiment, ultracold ^{87}Rb takes the role of the thermal bath, while ^{41}K acts as the working fluid, with the interactions being controlled using Feshbach resonances. The most simplistic to implement experimentally is the Quantum Carnot Engine (QCE) seen in Figure 2.6, which consists of four main transformations:

- (1) A hot quantum isothermal expansion at a temperature, T_1, where the working fluid receives heat from the thermal bath
- (2) A quantum adiabatic compression where work is extracted from the working fluid
- (3) A cold quantum isothermal compression at a temperature, $T_2 < T_1$, where the working fluid transfers heat to the thermal bath
- (4) A quantum adiabatic expansion where work is done on the working fluid.

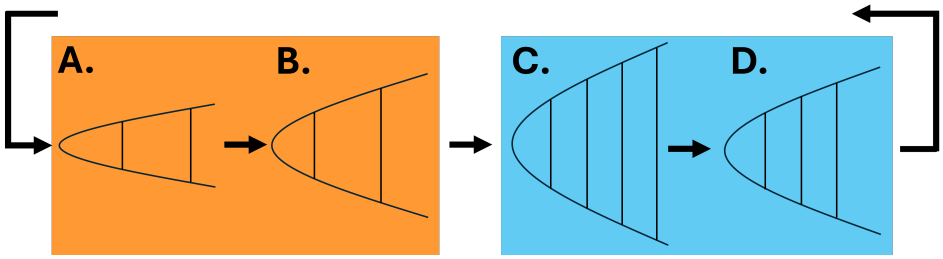

Figure 2.6: Depiction of the quantum Carnot engine taken from [6]. A→B and C→D represent the quantum isothermal transformations with a hot (orange) and cold (blue) bath, respectively. B→C and D→A represent the adiabatic transformations.

2.2 Feshbach Resonances and Tunable Interactions

In order to realise the quantum thermodynamic transformations set out in Section 2.1.3, we need to be able to model and control the short range interaction between a pair of atoms. In order to do this, Feshbach resonances can be used, with many of the key ideas explained in [65]. For this, we can use a molecular potential that depends on the internal states of the atoms.

The atoms used within this experiment have spin structure, and the two atoms can be labelled $i = 1$ or $i = 2$. The electronic orbital angular momentum L_i is coupled to the total electronic spin angular momentum S_i, giving J_i which is coupled to the nuclear spin I_i, to

give the total angular momentum F_i. Each of the eigenstates are given a label q_i, which at zero magnetic field are represented by $F_i m_i$. Both of the atomic species used in this experiment have $^2S_{1/2}$ ground states as they are alkali-metal atoms, with quantum numbers $L_i = 0$ and $S_i = 1/2$. Both isotopes also share the same value of $I_i = 3/2$, which leads to two values of the total angular momentum, $F_i = 1$ and $F_i = 2$. Applying a magnetic field across the atoms will split these levels into Zeeman sublevels. Figure 2.7a and Figure 2.7b display the energy levels for ^{87}Rb and ^{41}K respectively according to the Breit-Rabi formula [73]. Both atomic species are bosons.

A collision event is proposed with atoms prepared in states q_1 and q_2, which are initially separated by a large distance R. They then interact and separate into the individual atoms with states q_1' and q_2'. With the scattering channels being defined by the internal states of the two atoms and the partial wave, $|\alpha\rangle = |q_1 q_2\rangle\,|\ell m_\ell\rangle$, where $\left\langle \hat{R}\middle|\ell m_\ell\right\rangle = Y_{\ell m_\ell}(\hat{\mathbf{R}})$. For an s-wave collision occurring in a magnetic field, we can label the channel using only the quantum numbers $\{q_1 q_2\}$. The channel energy is defined as $E_\alpha = E(q_1) + E(q_2)$, which is the internal energy of the atoms. We can prepare the atoms in channel α with a kinetic energy E, which leads to a total energy $E_{tot} = E_\alpha + E$. We now introduce a second channel β with energy E_β. If $E_\beta \leq E_{tot}$ it represents an open channel, and if $E_\beta > E_{tot}$ it represents a closed channel.

The two channel model is visualised within Figure 2.8 displaying the two molecular potential curves. These are $V_{bg}(R)$ and $V_c(R)$ where R is the atomic separation. At large values of R the background potential, $V_{bg}(R)$ asymptotically connects to two free atoms in the ultracold gas. If we have a collision process with a very small E, then $V_{bg}(R)$ represents the energetically open channel, with $V_{bg}(R \to \infty) < E$, and $V_c(R)$ is the closed channel with $V_c(R \to \infty) > E$.

Resonant features arise when the potential energy of the bound molecular state of the closed channel nears that of the energetically open channel, exhibiting a change in collisional

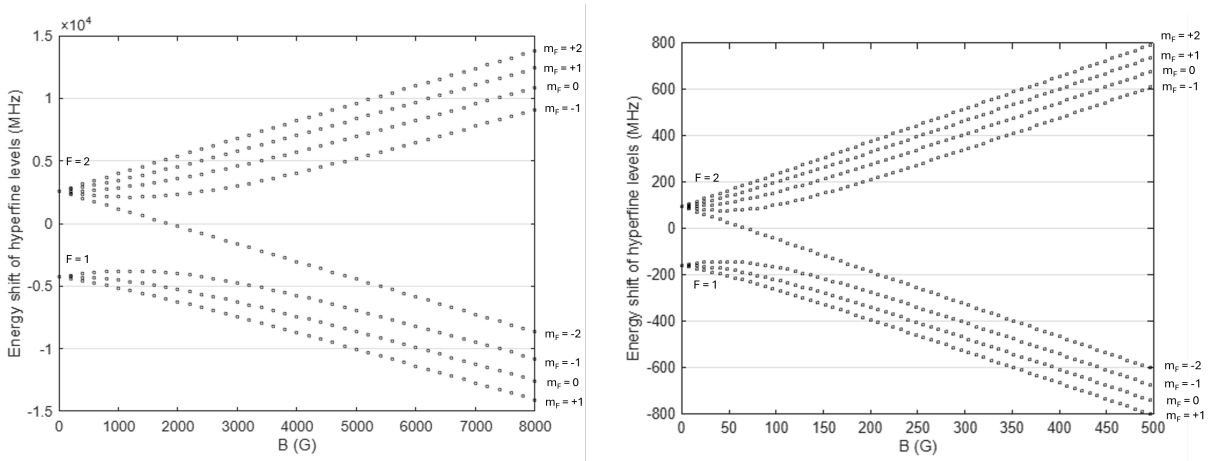

(a) Atomic energy levels for ^{87}Rb which has $S = 1/2$, $I = 3/2$ and $F = 1$ and 2. The two F levels are split at $B = 0$ by a hyperfine energy 6.834 GHz

(b) Atomic energy levels for ^{41}K which has $S = 1/2$, $I = 3/2$ and $F = 1$ and 2. The two F levels are split at $B = 0$ by a hyperfine energy 254.0 MHz

Figure 2.7: Atomic energy levels for ^{87}Rb and ^{41}K atoms, when an external magnetic field is applied [74].

properties. In this study, the energy difference between the states will be tuned using an external magnetic field, when the corresponding magnetic moments are different. This shifts the potential energy of the closed channel and its magnetic sublevels. The expression below describes a magnetically tuned Feshbach resonance, displaying the behaviour of the scattering length a_{sc},

$$a_{sc}(B) = a_{bg}\left(1 - \frac{\Delta_{sc}}{B - B_0}\right), \tag{2.9}$$

where B is the applied magnetic field, a_{bg} is the scattering length associated with the open channel, B_0 denotes the resonance position where the scattering length diverges, and Δ_{sc} is the resonance width.

In order to control the interactions between the two atomic species selected, we take advantage of the low field heteronuclear Feshbach resonances between ^{87}Rb $|F = 1, m_F = 1\rangle$ and ^{41}K $|F = 1, m_F = 1\rangle$. Even though both species have a ground state where $F = 1$,

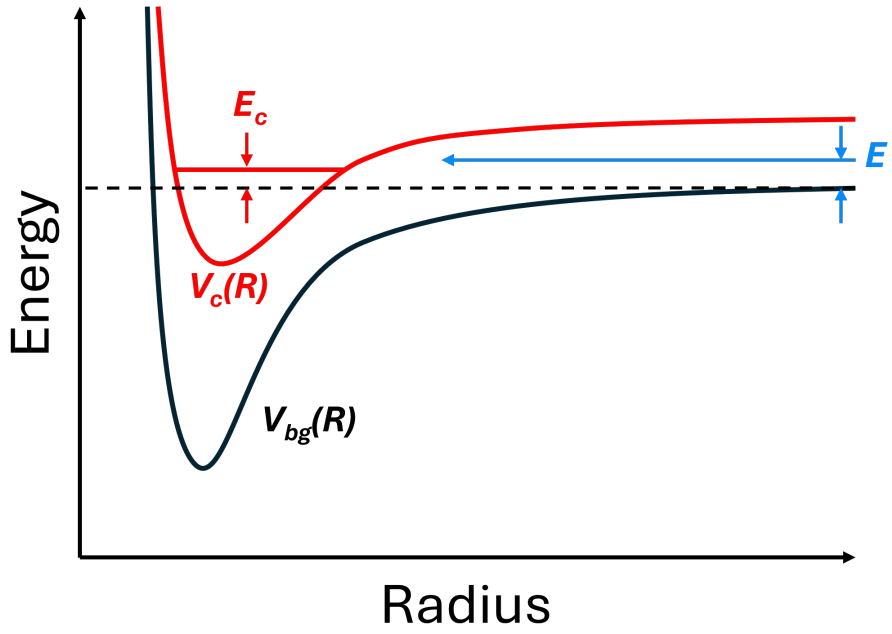

Figure 2.8: The basic two-channel model for a Feshbach resonance. Two atoms collide with energy E in the open channel and couple to a molecular bound state with energy E_c supported by the closed channel.

different methods for each species must be used in order to obtain the atoms in the magnetic sublevel, $m_F = 1$. For Rb, this involves distilling the sublevels by using a magnetic field pulse that polarises the atom into the required sublevel as it becomes favoured. While for K, we optically pump the atom, which uses specifically tuned light to transfer the atomic population into the desired sublevel. The scattering length, a_{sc}, between the two atomic species versus the applied magnetic field can be seen in Figure 2.9. The calculated scattering lengths originate from the collection of work seen in [75–78] with theoretical models developed from experimental Feshbach Spectroscopy. It can be seen that in the range of $\sim$ 50 G - 70 G, that the interaction very quickly goes from attractive, to a zero crossing, to repulsive between the two species. At the zero crossing, the interactions are essentially switched off.

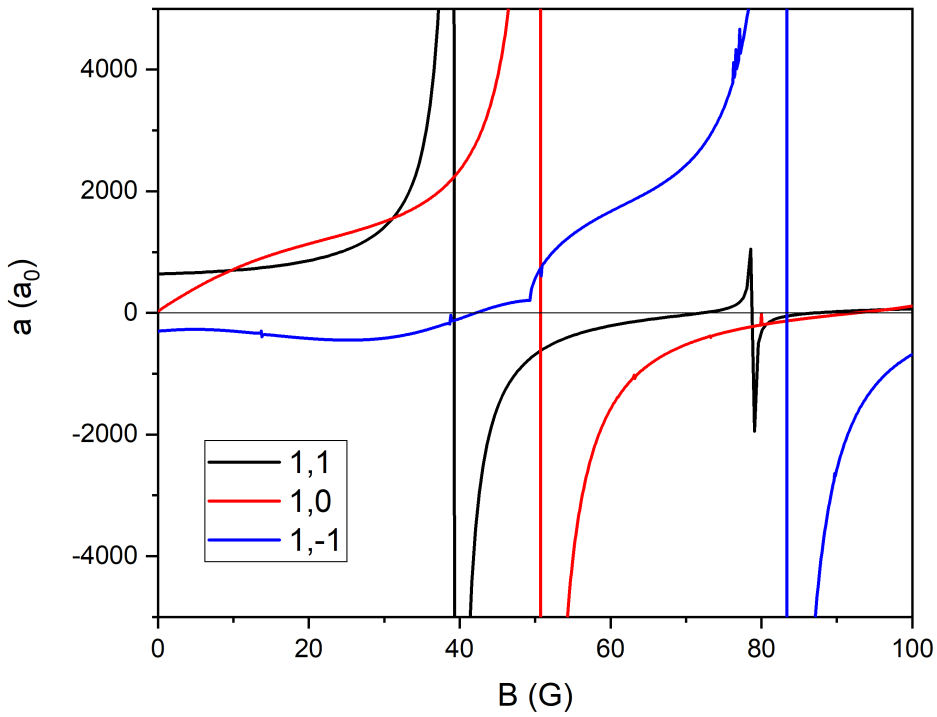

Figure 2.9: Scattering lengths for the interaction between ^{87}Rb and ^{41}K as a function of the applied magnetic field for different K states. We are concerned with the $^{87}\text{Rb}|1,1\rangle$ and $^{41}\text{K}|1,1\rangle$ interaction, which is represented by the black line. Here we can observe two Feshbach resonances. The zero-crossing of the scattering length occurs at $B = 71.34$ G.

2.2.1 Confinement Induced Resonances

The following theoretical work was first laid out in my publication [41]. A main focus of this work is the control of the coupling term H_{IB} from Equation 1.1. This coupling arises from the ultracold collisions between the impurity and the bath. As seen in Section 2.2, the ^{41}K-^{87}Rb mixture is quite appealing due to the ease of controlling the interactions. This is because of the two fairly broad s-wave Feshbach resonances and zero crossings that exist below 100 G [79]. This can be considered as being in the 3D-3D regime. But, as our K atoms are tightly trapped in an optical tweezer, the situation changes.

When $k_B T \leq \hbar\omega_i^{(K)}$, with $i = x, y, z$, the motion of the K atom is frozen in the i direction(s), which confines the motion of the atom to the remaining dimension(s). Due

to the properties of an optical tweezer, the transverse trapping frequencies are identical, $\omega_y^{(K)} = \omega_z^{(K)} =: \omega_{yz}^{(K)}$. Then, by lowering the temperature, it is possible to slowly reduce the dimensionality of the K atom motion from 3D to 1D and even further to 0D. On the other hand, the motion of the Rb atoms in the bath can be described by the thermal motion of particles in a 3D harmonic potential with frequencies $\omega^{(Rb)} \ll \omega^{(K)}$. This leads to an interaction between the K atom and Rb bath that is effectively in mixed dimensions, meaning we no longer expect the same behaviour of the interspecies scattering length seen in the 3D-3D regime [80] [81] [82]. It is expected that a single s-wave Feshbach resonance will generate a series of Feshbach resonances in s- and higher partial waves. This is because a tight trapping of the K atoms leads to a tight confinement of the resulting KRb Feshbach molecule, as it also experiences the potential.

We now look at the 1D-3D regime, neglecting $\omega_x^{(K)}$ and $\omega_x^{(Rb)}$. If the KRb molecule has a binding energy, $|E_b| \gg \hbar\omega$ we expect new resonances to appear approximately when the energy of the confined KRb molecule coincides with the scattering threshold at

$$(1 + |m| + 2n)\sqrt{\frac{m_K}{m_K + m_{Rb}}}\hbar\omega_{yz}^{(K)} - |E_b| = \hbar\omega_{yz}^{(K)}, \tag{2.10}$$

where $m = 0, \pm1, \pm2, ...$ is a magnetic quantum number, $n \geq 0$ is an integer, $m_{K(Rb)}$ is the K (Rb) mass, and $|E_b|$ is the binding energy of the KRb molecule in free space [83]. The 3D-3D resonance is expected to disappear. This means for each n, we expect a series of resonances in higher partial waves, labelled with m. We choose to ignore the higher order resonances, d-wave ($m = 2$) and f-wave ($m = 3$), as they're expected to overlap with and be weaker than the s-wave ($m = 0$) and p-wave ($m = 1$) resonances, by looking at Equation 2.10.

2.3 Single Atom Collisions

My system consists of a single ^{41}K atom trapped in an optical tweezer with temperatures in the range of tens of μK, immersed within an ultracold bath of ^{87}Rb atoms with temperature on the order of 1 μK. In order to use these components to realise the quantum thermodynamic transformations, we must first understand how the single atom will interact with the bath of atoms through thermalisation and losses.

2.3.1 One-Body Interactions

We first consider the losses due to collisions between the single K atom and the background gas, which can be caused by thermal K or Rb atoms. The scattering rate, γ_{bg}, due to the collisions between background atoms and K atoms is given by:

$$\gamma_{bg} = n_{bg}\sigma v_{bg}, \tag{2.11}$$

where n_{bg} is the atomic density of the background atoms, and v_{bg} is the average velocity of the atoms [84, 85]. v_{bg} is calculated as the average thermal velocity, so $v_{bg} = \sqrt{2k_bT_{bg}}$, with T_{bg} being the temperature of the background atoms. In this case, we can consider that the K atom will be ejected from the trap after a single collision with a background atom, this is because the collision energy far surpasses the trap depth by a few orders of magnitude. This collision process can be modelled as one body losses. If N is the number of K atoms, then the result is:

$$\dot{N}_K = \frac{dN_K}{dt} = -\gamma_{bg}N_K. \tag{2.12}$$

2.3.2 Two-Body Interactions

For a single atom in an optical tweezer, when the trap depth is far greater than the temperature of the atom, we can approximate the tweezer as a three-dimensional harmonic trap [72]. For an optical tweezer, the axial confinement is far weaker than the radial confinement due to the anisotropy of the beam. After a collision with a bath atom, the single atom can change vibrational levels. We expect the change in temperature of the single atom to go as

$$\frac{dT_K}{dt} = -(T_K - T_{Rb})\Gamma, \tag{2.13}$$

with $\Gamma = \Gamma_{KRb}/\xi$ the thermalisation rate, where

$$\Gamma_{KRb} = \sigma_{KRb} \underbrace{\sqrt{\frac{8k_B}{\pi}\left(\frac{T_K}{m_K} + \frac{T_{Rb}}{m_{Rb}}\right)}}_{\bar{v}_{KRb}} \int n_K n_{Rb} d^3x \tag{2.14}$$

is the elastic scattering rate [86], $\sigma_{KRb} = 4\pi a_{eff}^{(0)2}$ the scattering cross-section, and ξ the number of collisions needed to thermalise, which is a function of the initial T_K and the bath temperature T_{Rb} [72, 87, 88].

2.3.3 Three-Body Interactions

On top of this, we also want to characterise the losses of K atoms as they interact with the Rb bath. In our system, three-body losses could occur through two channels, namely KKRb and KRbRb. For the K density, three-body losses can therefore be described by the following rate equation:

$$\frac{dn_K}{dt} = -2\alpha_{KKRb} n_K^2 \tilde{n}_{Rb} - \alpha_{KRbRb} n_K \tilde{n}_{Rb}^2, \tag{2.15}$$

where α_j is the collision rate per unit of volume in the j channel, that in general has a power law dependence on the scattering length, and $\tilde{n}_{Rb}$ is the local density of Rb in the tweezer volume. Since in our system we expect to only have $\simeq 1$ K atom, we expect the first term in Equation 2.15 to be negligible.

2.4 Bayesian Data Analysis and Global Thermometry

The Bayesian-global paradigm was first introduced in [40, 89]. Although the focus of the study in Chapter 6 (adapted from [71]) concerned the specific release-recapture method for my experiment, this method can be applied to any thermometry experiment in which the temperature behaves as a scale parameter [90]. The following theoretical work has been adapted from our work in [71].

The goal here is to estimate a temperature T from a set of measurement outcomes $\mathbf{n} = (n_1, ..., n_\mu)$ which are recorded in μ runs of an experiment. We also consider a controllable parameter t that we set to $\mathbf{t} = (t_1, ..., t_\mu)$ in each subsequent run. We want to extract the maximum information possible from these data, which requires a likelihood function [33, 34]. Assuming each experimental run is independent, a probability $p(n_i|T, t_i)$ needs to be found, which is the probability for obtaining the outcome n_i given T and t_i. The true temperature is unknown, so we work with a hypothesis $\theta \in [\theta_{min}, \theta_{max}]$ about its value. A weight can then be assigned to the different θ depending on the measurement record ($\mathbf{n}$, $\mathbf{t}$), by constructing the probability $p(\theta|\mathbf{n}, \mathbf{t})$. By using Bayes theorem, this distribution can be written as

$$p(\theta|\mathbf{n}, \mathbf{t}) \propto p(\theta) \prod_{i=1}^{\mu} p(n_i|\theta, t_i), \tag{2.16}$$

where $p(n_i|\theta, t_i)$ is our likelihood model evaluated at θ, and $p(\theta)$ is the probability representing information about T prior to collecting the data. As we don't tend to have any prior knowledge about T, we choose the distribution $p(\theta)$ that corresponds to maximum igno-

rance within $[\theta_{min}, \theta_{max}]$ [91]. The energy scale in which the model $p(n_i|T, t_i)$ is applicable for release-recapture thermometry is determined by the unknown temperature itself. We can then say that temperature is a scale parameter [40, 89, 90, 92], and adopt Jeffreys prior

$$p(\theta) = \left[\theta \log\left(\frac{\theta_{max}}{\theta_{min}}\right)\right]^{-1}, \tag{2.17}$$

to represent the maximum ignorance about it [33, 34, 93]. As $p(\theta)$ and $p(n_i, t_i|\theta)$ are now fixed, we can use Equation 2.16 as follows. We take our initial measurement (n_1, t_1), then the likelihood $p(n_1|\theta, t_1)$ is calculated as a function of θ. The functions $p(\theta)$ and $p(n_1|\theta, t_1)$ are multiplied and the result is normalised. We see this as updating the initial information with the first set of measured data. We proceed to record (n_2, t_2) and repeat the process using $p(n_2|\theta, t_2)$. This continues for μ iterations, where we arrive at $p(\theta|\mathbf{n}, \mathbf{t})$ which encodes all of the available temperature information. This is why it is known as the posterior probability.

From this, we can extract an estimate and its associated error. As shown in [89], whenever T behaves as a scale parameter, the optimal estimator is given by

$$\tilde{\vartheta}(\mathbf{n}, \mathbf{t}) = \theta_u \exp\left[\int d\theta\ p(\theta|\mathbf{n}, \mathbf{t}) \log\left(\frac{\theta}{\theta_u}\right)\right], \tag{2.18}$$

where θ_u neutralises the units within the logarithm [94] without affecting the value of $\tilde{\vartheta}(\mathbf{n}, \mathbf{t})$. For this study, we set $\theta_u = 1\ \mu$K. We also have the error for the estimator in Equation 2.18 as

$$\Delta\tilde{\vartheta}(\mathbf{n}, \mathbf{t}) = \tilde{\vartheta}(\mathbf{n}, \mathbf{t})\sqrt{\bar{\epsilon}_{\mathrm{MLE}}(\mathbf{n}, \mathbf{t})}, \tag{2.19}$$

where

$$\bar{\epsilon}_{\mathrm{MLE}}(\mathbf{n}, \mathbf{t}) = \int d\theta\ p(\theta|\mathbf{n}, \mathbf{t}) \log^2\left[\frac{\tilde{\vartheta}(\mathbf{n}, \mathbf{t})}{\theta}\right], \tag{2.20}$$

is the mean logarithmic error, a relative error, evaluated for the current dataset. The Bayesian temperatures can therefore be written as $\tilde{\vartheta}(\mathbf{n}, \mathbf{t}) \pm \Delta\tilde{\vartheta}(\mathbf{n}, \mathbf{t})$. We also look into

the idea of mean information gain for a single shot. This can be quantified as

$$\mathcal{K}(t) = \sum_n p(n|t)\ \log^2\left[\frac{\tilde{\vartheta}(n,t)}{\tilde{\vartheta}_p}\right], \tag{2.21}$$

where

$$\tilde{\vartheta}_p = \theta_u\ \exp\left[\int d\theta\ p(\theta)\ \log\left(\frac{\theta}{\theta_u}\right)\right], \tag{2.22}$$

and

$$p(n|t) = \int d\theta\ p(\theta) p(n|\theta, t). \tag{2.23}$$

From this, we can adaptively adjust the control parameter t to maximise $\mathcal{K}(t)$ at every iteration. This makes each measurement maximally informative.

Chapter 3

Experimental Setup

In this chapter, I discuss the key parts of the experimental setup which allows for the cooling of two different atomic species down to the ultracold regime, alongside the ability to manipulate them. This is a continuation of the efforts of the previous set of PhD students, while introducing some important new additions that were put in place by myself. Some of which were major refinements of the system, others were completely new optical paths. As such, the structure of this chapter follows that of the work in [69], with some overlap of content.

- **Section 3.1** describes the vacuum system, which is where the atoms are cooled and trapped. Without it, the ultracold samples would interact with the much hotter background atoms and heat up.
- **Section 3.2** describes the laser system, which is used for the cooling and trapping of the atoms, from room temperature to the ultracold regime. The schematics of the physical system are also displayed
- **Section 3.3** describes the optical tweezer setup used to trap a single K atom.

- **Section 3.4** explains the optical pumping setup, which is required to pump the atomic species into the correct state for the particular Feshbach resonance I wish to explore.
- **Section 3.5** displays the imaging system and the various techniques used in order to quantify the atoms and their characteristics.

3.1 Vacuum System

In experiments such as this one, an ultra-high vacuum (UHV) is required otherwise the cold atom samples will be heated due to collisions with background atoms, also limiting the lifetime of the atoms in the trap. The potential sources of these background atoms are either from the atomic sources or the air that's trapped within the system, both of which have much higher temperatures than the cold atoms. In order to reach the cold regime, the required pressure is 10^{-7} mbar. Further to this, in order to reach the ultra cold regime, the required pressure is 10^{-10} mbar.

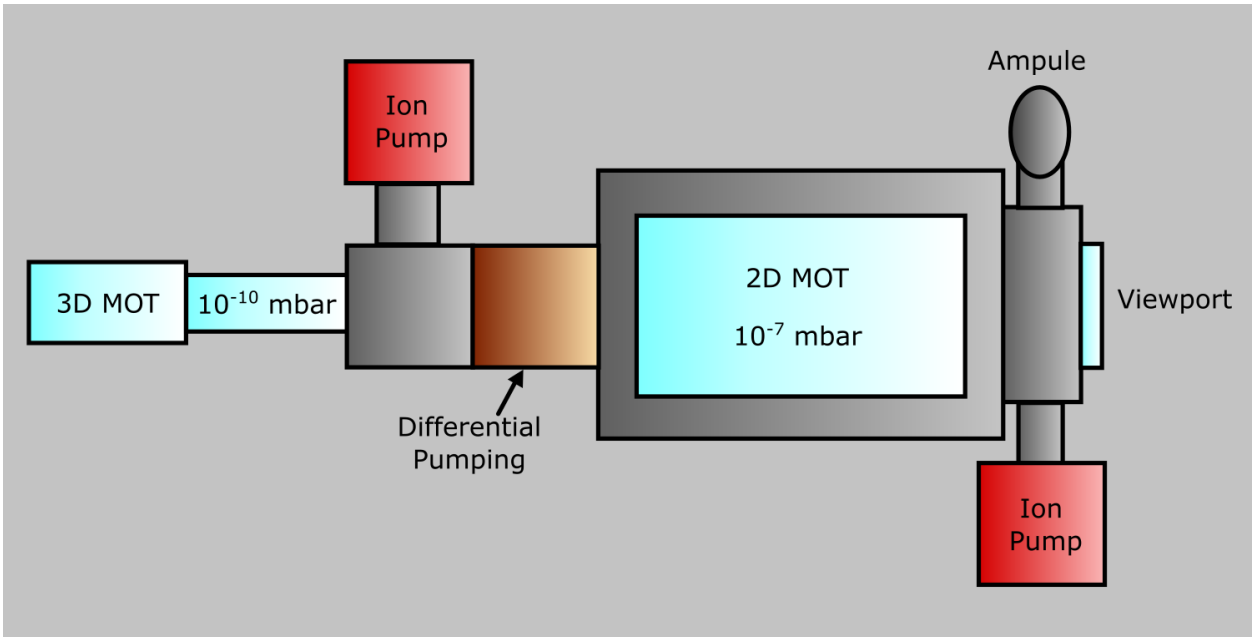

Figure 3.1: Diagram of the vacuum system used in the experiment.

The vacuum system is separated into two chambers, which can be seen in Figure 3.1. The

first of which is the 2D MOT chamber, here the atoms are pre-cooled using a MOT. This traps and cools the atoms in two dimensions, starting from a room temperature vapour, down to a flux of cold atoms. The 2D MOT chamber is made out of a single block of titanium, with four windows of size 4×10 cm. The pressure within is 10^{-7} mbar.

On one end of the chamber there is an ion pump to maintain the vacuum as well as two metallic bellows that contain the ampoules that release both the Rb and K samples. There is also a valve to connect a turbo molecular pump, which can be used in the initial pumping stages. Still on the same side, there is a viewport to allow a push beam to pass through the 2D MOT to the 3D MOT. The atoms are then moved to and captured within a 3D MOT, also named the science chamber. Here, the atoms are laser cooled and trapped across three spatial directions at a pressure of 10^{-10} mbar. The 3D MOT chamber is a rectangular glass cell, which allows for a huge amount of optical access.

The two chambers are connected by a hole with a diameter of 1 mm and a length of 1 cm. This creates a differential pumping system, which allows us to maintain the pressure in the two chambers, and the three orders of magnitude pressure difference between them. The higher pressure in the 2D MOT allows for a higher density-flux of atoms, which will then be transported to the 3D MOT. Once the atoms are in the 3D MOT, the atomic species can then be prepared in the required states, depending on the experimental requirements. This setup consisting of two separate chambers enables efficient cooling and trapping of the two atomic species, starting from atoms at room temperature, cooling all the way down to the ultracold regime.

On the outside of the 2D MOT chamber, there are a set of coils in the anti-Helmholtz configuration for both the horizontal and vertical directions, which are required to trap the atoms. The 3D MOT only has two coils, but using a four way relay, it's possible to switch between Helmholtz and anti-Helmholtz configuration. The coils are used to make the 3D MOT, and can tune the scattering length of the atomic sample with Feshbach resonances

(see Section 7.1). There are also a set of vertical compensation coils, in anti-Helmholtz configuration, to control the position of the atomic species slightly.

3.2 Laser System

The main laser system used to cool and trap atoms can be separated into two distinct parts. The first of which is the laser cooling system, used to cool the atomic species from room temperature down to a few tens of μK. The other key piece is the dipole trapping system, and as the name suggests, it traps the previously cooled atoms. From there, evaporative cooling can be performed on the atomic sample to reduce the temperature further, all the way down to the ultracold regime. Applications of this system can be seen in Chapter 6 and Chapter 7.

3.2.1 Laser Cooling System

The laser cooling for the MOTs of both of the atomic species is performed by using the transitions in their respective D_2 lines. To perform laser cooling, a closed atomic transition is required, which is defined as a transition from a stable ground state to an excited state, which can then only decay back to the same ground state. Although, for the atomic species used in this experiment, there is no perfect closed transition. There is a non-zero probability that a nearby open transition is excited, which can optically pump the atoms into a dark state. Because of this, repumping lasers are required in order to remove the atoms from the dark states, reintroducing them into the states used for laser cooling.

Figures 3.2 and 3.3 show the structure of the atomic levels for the D_2 lines of ^{87}Rb and $^{39-41}$K respectively. Within the diagrams, ω_{cool} and ω_{rep} correspond to the laser frequencies of the cooling and repumping transitions, while Δ_{cool} and Δ_{rep} are the accompanying laser detunings. The cooling laser addresses the $|F = 2\rangle \rightarrow |F' = 3\rangle$, but there is also a non-

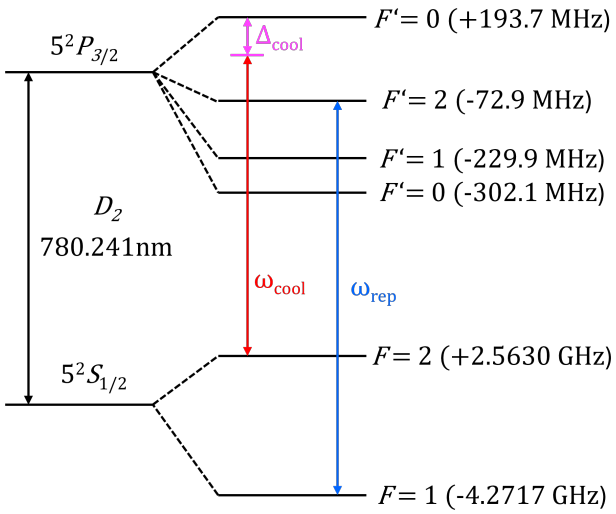

Figure 3.2: The structure of the atomic levels of the ^{87}Rb D_2 line [95]. The frequency difference between each hyperfine level and their fine level are noted within the brackets. ω_{cool} and ω_{rep} are the frequencies used for the cooling and repumper lasers, respectively. Δ_{cool} is the detuning of the cooling laser with respect to the cooling transition.

zero probability that it excites the $|F = 2\rangle \rightarrow |F' = 2\rangle$ transition, which may then decay to $|F' = 1\rangle$. This is no longer in the cooling cycle and is inaccessible by the cooling laser. Because of this, a repumping laser is needed which excites the transition $|F = 1\rangle \rightarrow |F' = 2\rangle$, which repopulates the cooling cycle. However, the excited levels for the K atoms are very close, separated by only a few MHz. This is within the order of the natural linewidth of the D_2, Γ_K. This leads to some overlap in the functions of the cooling and repump lasers, meaning that the repump laser is able to exert force on the atoms. This is not the case for the Rb samples. The atomic transitions for each of the atomic species are as follows: for Rb, the cooling transition is $|5s^2S_{1/2}, F = 2\rangle \rightarrow |5p^2P_{3/2}, F = 3\rangle$, and the repump transition is $|5s^2S_{1/2}, F = 1\rangle \rightarrow |5p^2P_{3/2}, F = 2\rangle$. Whereas the K cooling transition is $|4s^2S_{1/2}, F = 2\rangle \rightarrow |4p^2P_{3/2}, F = 3\rangle$, with the repump transition being $|4s^2S_{1/2}, F = 1\rangle \rightarrow |4p^2P_{3/2}, F = 2\rangle$.

For successful laser cooling, three features are required. First, the correct frequencies for the desired transitions, which must not deviate for long periods of time, and also be tunable.

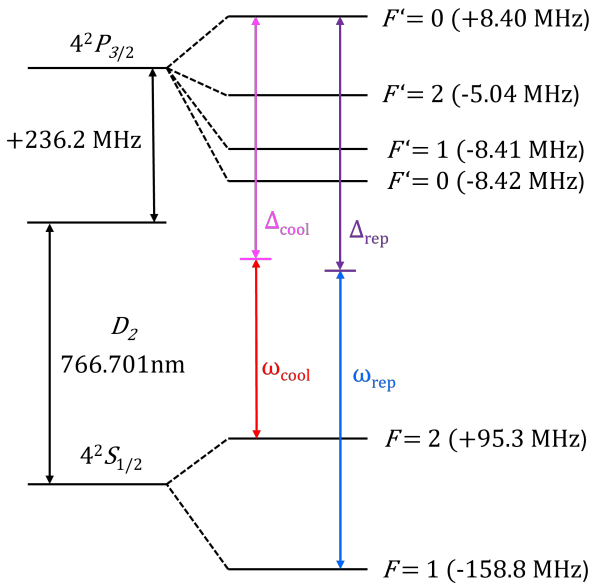

Figure 3.3: The D_2 line for ^{41}K [96]. The cooling and repumper laser frequencies are represented by ω_{cool} and ω_{rep}, respectively. Δ_{cool} and Δ_{rep} are the detunings between their respective laser frequency and the frequency of the transitions.

In order to stabilise the frequencies, I employ two techniques. The first of which is Doppler free saturated absorption spectroscopy [97]. To begin, the laser frequency is swept thought the atomic sample. This produces an atomic transition reference signal, which contains peaks. In order to lock to this signal to the correct point, it needs to have a zero crossing, so a proportional-integral-differential circuit (PID) can be used. To reach this signal, fast modulation is used on top of the scanning signal to obtain the derivative of the signal by phase modulation. The PID circuit is built into both of the laser controllers (TOPTICA DLC Pro). The second method is sideband offset locking [98]. This method generates a beat signal between the repumper and cooling lasers. The repumper laser is used as a reference to lock the cooling laser. Like saturated absorption spectroscopy, this also uses a PID circuit to lock the laser frequency.

3.2.1.1 Laser Cooling Layout

The main laser cooling system used in this experiment can be separated into four distinct parts, which are described below:

- For the **Rb Laser Sources** (Figure 3.5a), the seed laser sources for both the repumper and the cooling light are both TOPTICA DL PRO lasers. The repumper light passes through a Rb cell to perform saturated absorption spectroscopy to lock the laser. The repumper light is then combined with the cooler light, which is then incident on a photodiode (PD). This generates the beat signal that is required to lock the cooling laser to the repump laser by sideband offset locking. There are a total of three tapered amplifiers (TAs), model EYP-TPA-0780, which amplify the power of the input laser to the power required for laser cooling. The repumper light passes through one, and is fibre coupled to the Rb distribution. The cooling seed also passes through a TA, where it then splits. One arm is denoted as 2D cooling and is coupled to a fibre leading to the Rb distribution, the other arm as 3D cooling. This light first passes through another TA before being fibre coupled to the Rb distribution.

- The **Rb Laser Distribution** (Figure 3.5b) consists of three acousto-optical modulators (AOMs) used to control the intensity and the frequency of the repumper and cooling light. A further fourth AOM is used to set the beam to the correct frequency for the pushing and imaging beams. The light for the 3D MOT is a combination of the cooling and repumper beams, separated over three outputs, which are then sent to three sets of opposing outputs to create the six beam 3D MOT. A small fraction of this light is directed towards a fibre for the tweezer guide beam, only used for the initial alignment of the optical tweezer.

- For the **K Laser Sources** (Figure 3.6a), there is a single seed laser, which is a TOPTICA DL PRO. Similar to the Rb distribution, the light passes through a K cell for

saturated absorption spectroscopy to lock the laser. Two TAs are used, model EYP-TPA-0765, to amplify the light to the necessary power for laser cooling. There are two AOMs used to shift the frequency of the light, and because the required frequencies for K cooling and repumping are so similar, it's satisfactory to use a single laser together with a combination of AOMs. The light then reaches the rest of the K setup via free space.

- The **K Laser Distribution** (Figure 3.6b) consists of three AOMs used to control the frequency and intensity of the specific beams required for the laser cooling. This consists of an imaging and pushing arm, and a combination of repumper and cooling light used across the 2D MOT, 3D MOT and the side beam used to excite a single K atom in fluorescence imaging. See Section 5.2.1.

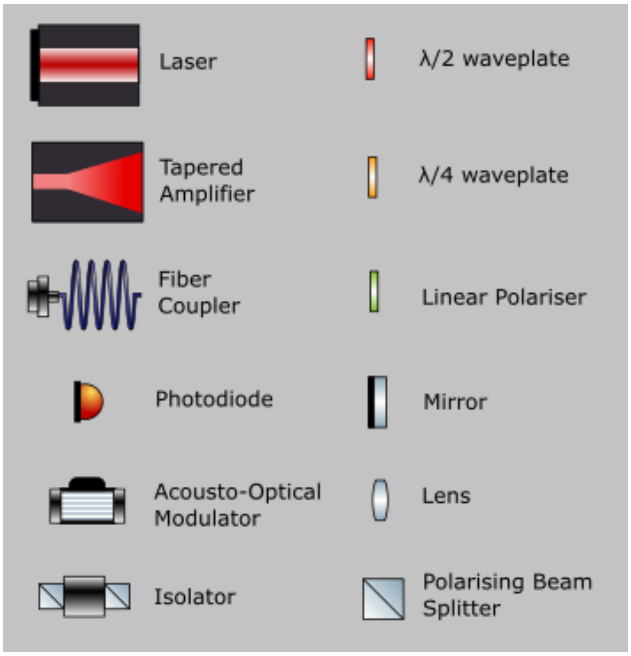

Figure 3.4: Key for the optical schematics.

The next point of concern is how I deliver the prepared light to the atoms. The light is coupled into 2:2 fibre splitters, meaning they have two inputs and two outputs. The Rb light is coupled into one of these inputs, with the K light being coupled into the other. The light

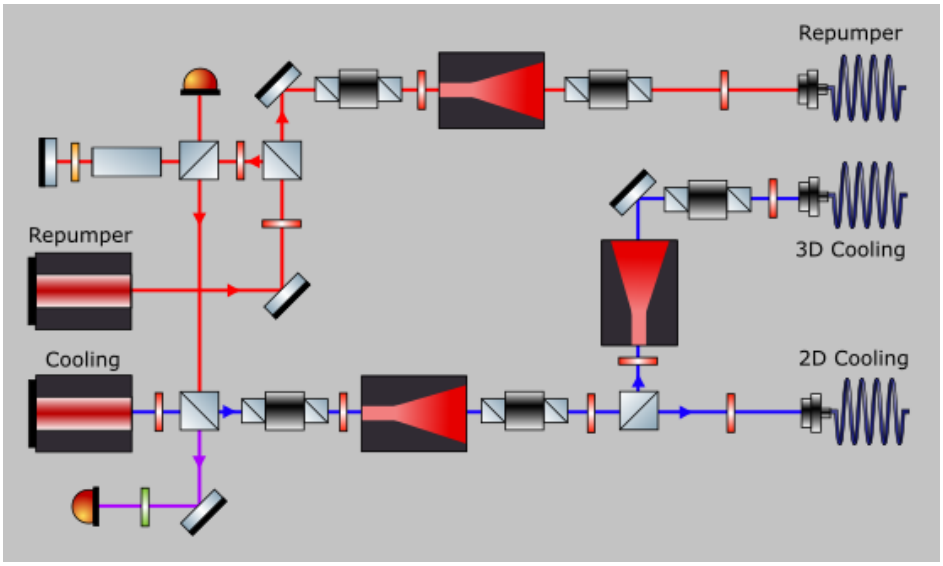

(a) Rb laser sources.

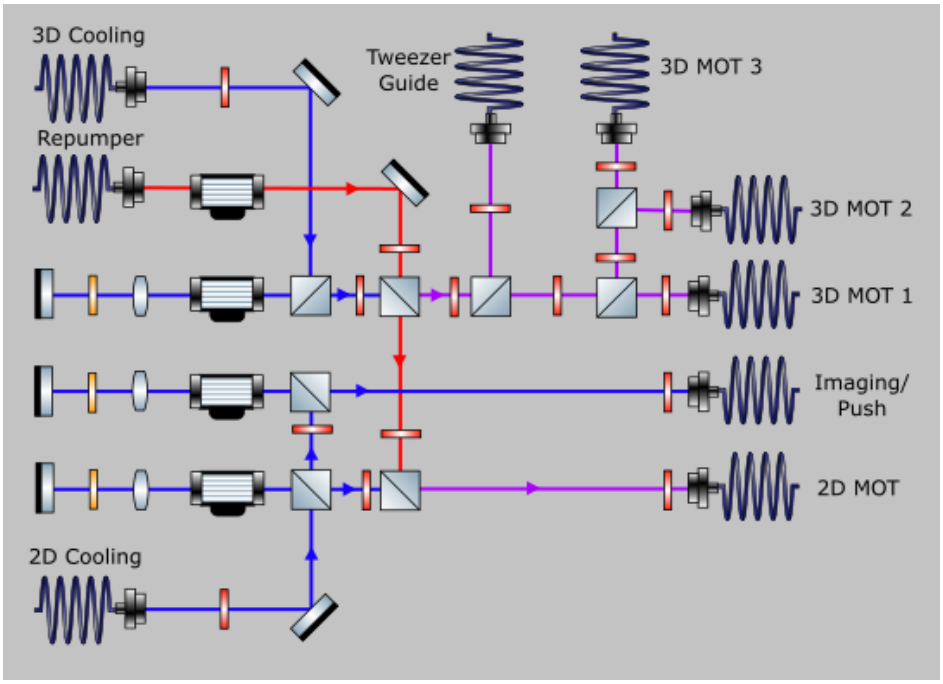

(b) Rb laser distribution.

Figure 3.5: Schematic for the laser layout used for Rb cooling. The red beams represent the repumper light, the blue beams represent the cooling light, and the purple beams are a mixture of the two.

is split and output evenly for each of the key optical stages. The first part is the 2D MOT, which consists of two beams of light. Each of the beams is collimated by two cylindrical

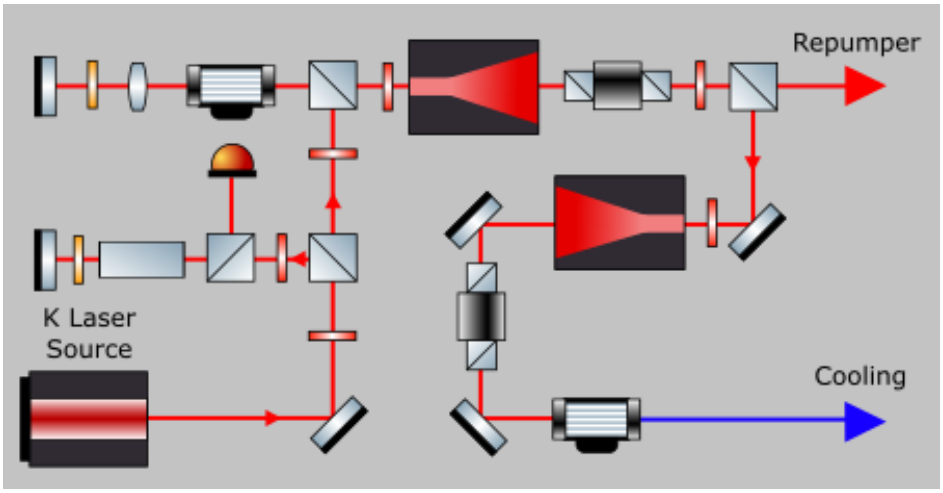

(a) K laser sources.

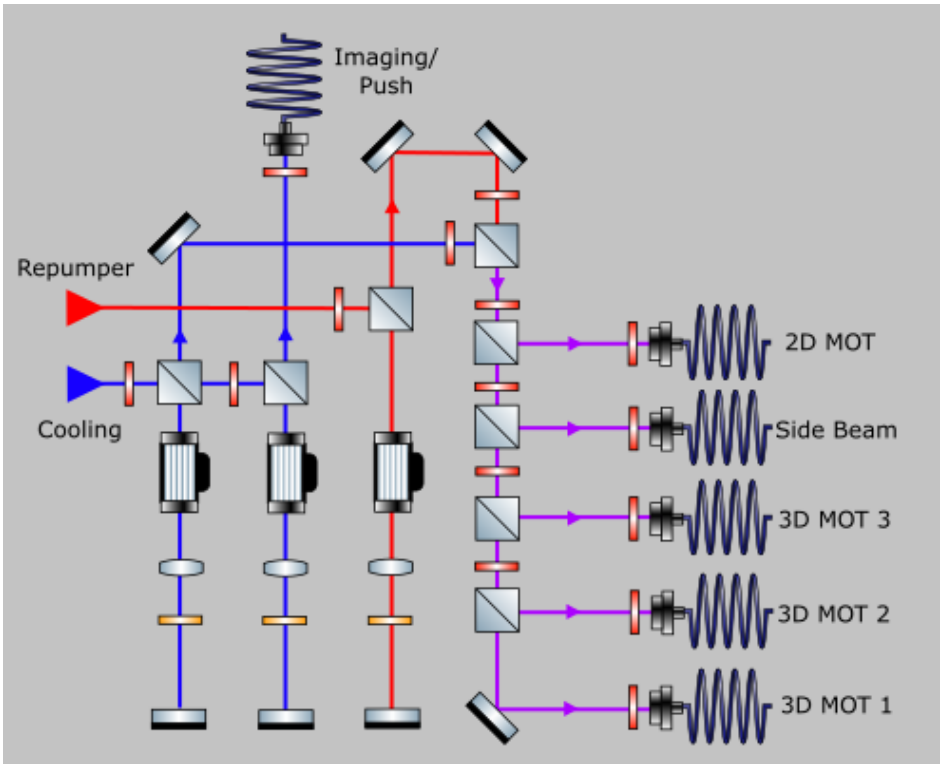

(b) K laser distribution.

Figure 3.6: Schematic for the laser layout used for K cooling. The red beams represent the repumper light, the blue beams represent the cooling light, and the purple beams are a mixture of the two.

lenses of focal length 6 cm and 20 cm, which are placed perpendicular to each other. This creates an elliptical beam of size 4×9 cm. $\lambda/4$ waveplates are used to produce the required

beam polarisation. Finally, the beams are retro-reflected using triangular prisms, this also makes sure that the beam polarisation is correct on the way back.

For the 3D MOT, three 2:2 fibre splitters are used for the six beams. The light comes out of the fibre into six lens tubes that have $\lambda/4$ waveplates and lenses with 10 cm focal length attached to the end. This creates a 25.4 mm beam size. There is also a 1:2 fibre splitter used for the push and imaging beams. For effective cooling of the atoms, the power of all six of the cooling beams must be balanced. In addition, for K, the repumper beams must also be balanced, due to the fact that the cooling and repumper beams overlap in function. To balance the force from the lasers, these powers must also be balanced. The values of the powers and detunings that I use for each species to load them into the MOT can be seen in Table 3.1.

Table 3.1: Values for each of the important parameters of the lasers for the loading of the MOT. These values are identical to the ones used in [69].

Laser	P_{cool} (mW)	Δ_{cool}	P_{rep} (mW)	Δ_{rep}
Rb 2D MOT	80	-1.5 Γ_{Rb}	30	0
Rb 3D MOT	80	-2.5 Γ_{Rb}	8	0
Rb Push Beam	1	0	0	0
K 2D MOT	100	-3 Γ_{K}	60	-2.5 Γ_{K}
K 3D MOT	80	-3 Γ_{K}	40	-2.5 Γ_{K}
K Push Beam	1.2	-1.5 Γ_{K}	0	0

3.2.2 Dipole Trap System

Once the atoms have been cooled to an appropriate temperature, they need to be trapped. This is performed with a dipole trap system. This allows for the manipulation of the trapped atoms alongside the evaporative cooling technique, which is used to cool the atoms to the ultracold regime. The setup can be seen in Figure 3.7, and consists of two high intensity beams crossed at their respective waists, this describes a crossed dipole trap. The main advantage this has over a single beam is that it has a better aspect ratio of trapping frequen-

cies, for a single beam the imbalance is very large with the axial trapping frequency being 10× smaller than the radial direction. To avoid unwanted interference effects, a bichromatic setup is used. The first laser is a 1070 nm Ytterbium fibre laser (model YLR-20-AC), which has a maximum output power of 20 W. After all the optical elements, it has a maximum power of 11 W and a waist of 36 ± 1 μm. The other laser is a 1550 nm Erbium fibre laser (model ELR-20-AC), with a maximum output power of 20 W. The maximum power used on the atoms is 3.5 W with a waist of 39 ± 1 μm. These waists were found using the knife-edge method. A knife blade is attached to a translation stage and is swept across the beam, the power of the resulting beam is measured. A plot of laser power with respect to the position of the knife edge is plotted, and an error function is fitted to it to find the waist. The setup of the crossed dipole trap seen in Figure 3.7 consists of the following:

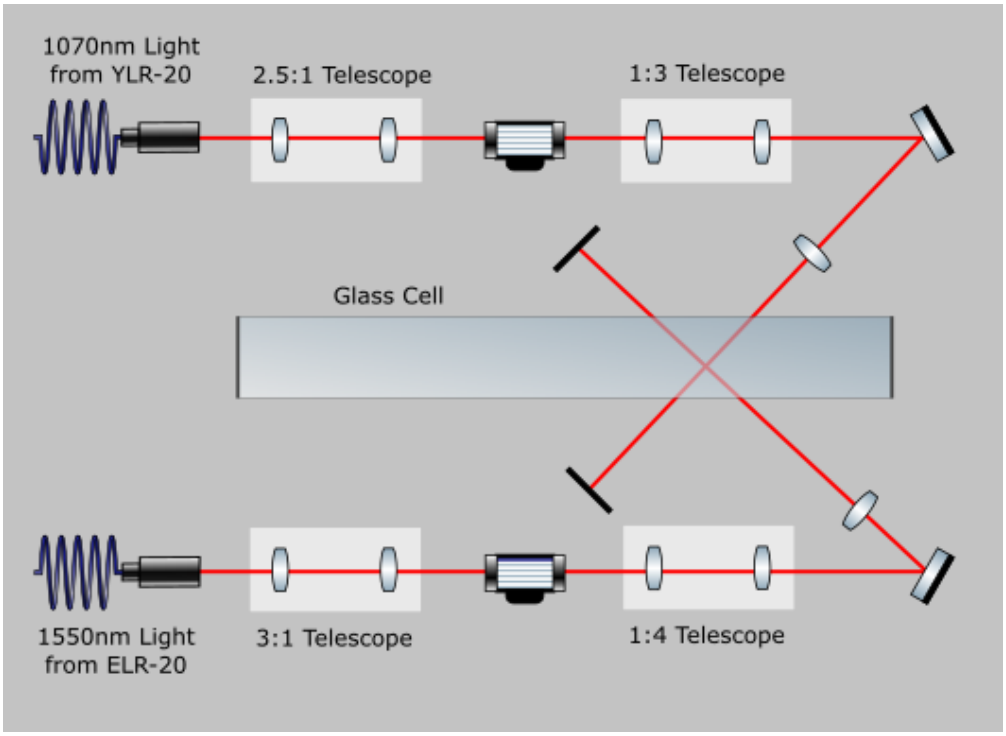

Figure 3.7: The optical path for the high-powered lasers used to create a dipole trap. The lasers have wavelengths of 1070 nm and 1550 nm.

1070 nm - The laser produces a continuous beam of light which is unpolarised. It has an integrated fibre collimator that emits a beam of size 5 mm. The light first passes through

a 2.5:1 telescope to reduce the beam size in order for it to pass through an AOM, which controls the beams power. The zeroth order from the AOM is blocked by a beam dump. The first order of the AOM then passes through a 1:3 telescope, which magnifies the beam before it's focused within the glass cell by a lens with a 10 cm focal length to produce the desired waist.

1550 nm - The setup is almost identical to that of the 1070 nm one. Like before, the laser produces a continuous beam of unpolarised light, which is emitted by an integrated fibre collimator with size 5 mm. A 3:1 telescope is used to focus the beam through an AOM, where the first order is then magnified by a 1:4 telescope. Finally, the light is focused to its desired waist by a 30 cm focal length lens.

3.3 Optical Tweezer

In order to realise the ideas set out above experimentally, I required an optical tweezer to trap and manipulate single atoms. An optical tweezer is a highly focused beam of light with a very narrow waist (<2 μm), which is very similar to the dipole traps explained earlier. A regime in which it's only possible to trap a single atom can be reached using the collisional blockade (see Section 5.1.2). In order to produce the beam waist required, I use a long working distance microscope objective, more specifically, the 20x Mitutoyo Plan Apochromatic NIR B Infinity Corrected Objective. This objective has a working distance of 25.5 mm and produces a waist below 2 μm. Due to the long working distance, the objective can be placed outside the glass cell without blocking the optical access of any other beams. The objective is attached to a nanopositioner, which allows us to move the beam vertically by up to 100 μm.

The optical tweezer setup can be seen in Figure 3.8. The light source is a Ti:Sa (Titanium Sapphire) laser (model M-Squared SolsTis), with a tunable wavelength between 600 nm and

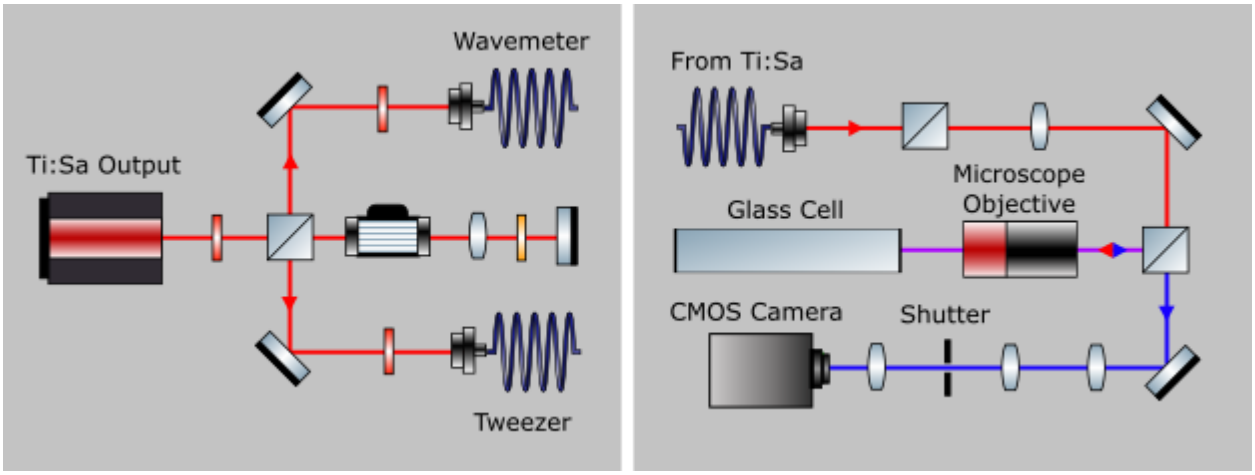

Figure 3.8: The optical layout for the optical tweezer setup. The red light is the tweezer light, which is incident on the atoms. The blue light is the fluorescence from the K atoms. The purple beam represents the overlap of these two wavelengths.

900 nm. It is pumped by a 532 nm laser (model Coherent Verdi), which outputs up to 12 W of power. At a pumping of 12 W, the Ti:Sa outputs 4 W at a wavelength 789.82 nm (50 mW maximum incident on the atoms), which is the tune-out wavelength for Rb. At the tune-out wavelength, no Rb atoms should be trapped in the tweezer (yet some Rb is still found to be trapped, see Section 5.1). This wavelength of light is able to trap K atoms without issue.

A small part of the light is coupled to a wavemeter, where it's possible to view the wavelength of the beam to pm precision. The rest of the light passes through a double pass AOM, which is used solely for intensity control. After being coupled through a fibre, there is a PBS which is used to clean the polarisation of the light, as fluctuations in the polarisation can affect the trapping potential of the tweezer. After this, there is a 20 cm focal length doublet lens which is used to acquire the correct beam size before the microscope objective. There is then a 70:30 (transmission:reflection) beam splitter, which is used to separate the tweezer light from the fluorescence signal of the K atoms. The tweezer light is then focused by the microscope objective to the desired waist within the glass cell.

The K atoms trapped within the tweezer will fluoresce, emitting light at a wavelength

of 767 nm, which is collected and collimated by the microscope objective. The light is transmitted through the 70:30 beam splitter, and the beam is enlarged by a telescope. I then focus the fluorescent light onto a single pixel of a CMOS camera (model Hamamatsu ORCA C-14440). To prevent ambient noise and noise from the tweezer light, a 767 nm bandpass filter is used in combination with a mechanical shutter.

3.4 Optical Pumping Setup

In order to explore the Feshbach resonances between ^{87}Rb and ^{41}K I require both species to be in the $|F = 1, m_f = 1\rangle$ state. To do this, the K atoms are optically pumped using the optical transitions of the D_1 line, which can be seen in Figure 3.9. The D_1 line has a wavelength of 770.108 nm. To pump exclusively into the $|F = 1, m_f = 1\rangle$ state, two frequencies of light are needed. The D_1 setup can be seen in Figure 3.10. Firstly, there needs to be a beam to excite the $|F = 1\rangle \rightarrow |F' = 1\rangle$ transition with σ^+ polarisation, then a beam to excite the $|F = 2\rangle \rightarrow |F' = 2\rangle$ transition with π polarisation.

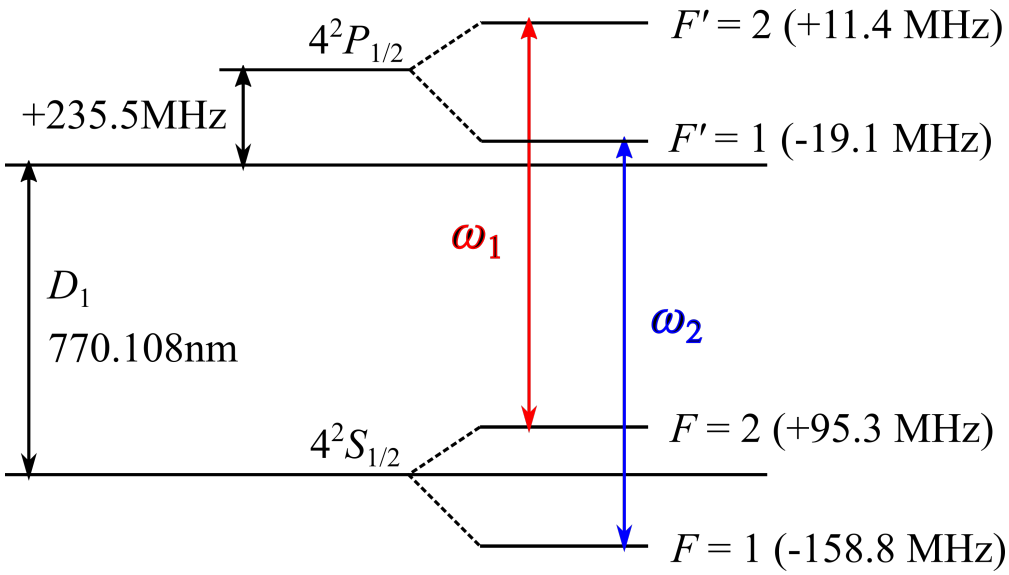

Figure 3.9: D_1 line for ^{41}K. The $|F = 2\rangle \rightarrow |F' = 2\rangle$ transition is excited with the frequency ω_1 and the $|F = 1\rangle \rightarrow |F' = 1\rangle$ transition is excited with the frequency ω_2.

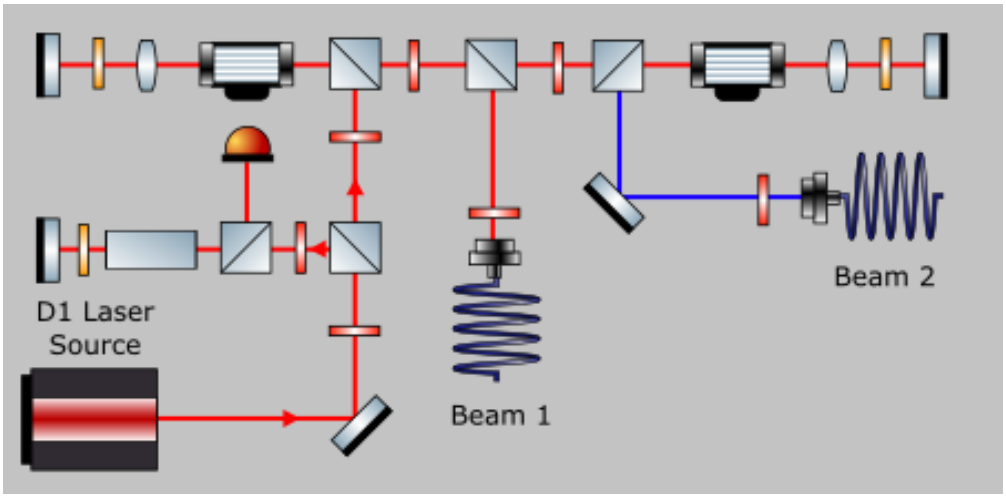

Figure 3.10: The schematic for the ^{41}K D_1 setup. The red beam passes through an AOM, so its frequency excites the $|F = 2\rangle \rightarrow |F' = 2\rangle$ transition. The blue beam excites the $|F = 1\rangle \rightarrow |F' = 1\rangle$ transition.

The laser source for the D_1 setup is a TOPTICA DL PRO laser. The light first passes through a K cell to perform saturated absorption spectroscopy to lock the laser. The laser is locked to the $|4s^2S_{1/2}, F = 1, 2\rangle \rightarrow |4p^2P_{1/2}, F' = 1, 2\rangle$ crossover of ^{39}K [99] [100]. The light then passes through a double pass AOM, where the frequency is shifted to the one required for the $|F = 2\rangle \rightarrow |F' = 2\rangle$ transition. This is coupled to a fibre, and is then incident on the K atoms in the glass cell in the horizontal direction. The light passes through a second double pass AOM to shift the frequency to that which is required for the $|F = 1\rangle \rightarrow |F' = 1\rangle$ transition. This is also fibre coupled, passing through a $\lambda/4$ waveplate to create the correct σ^+ polarisation. This beam is incident on the atoms in the vertical direction. The orientations of the beams are chosen due to the magnetic field defining the quantisation axis, which when in Helmholtz configuration is aligned vertically. The beam intensity is set to double that of the ^{41}K D_1 saturation intensity, which is 17.28 W/cm^2.

3.5 Imaging System

In order to examine the cold atom samples, they need to be imaged. For this I have two main cameras. The first camera (model Allied Vision Guppy PRO F-031) captures images in the horizontal direction, with the second camera (model Allied Vision Mako G-040) capturing images in the vertical direction. The cameras have a pixel size of 5.6 μm and 6.9 μm respectively. The images are then fed to a computer to be processed and analysed.

The optical layout for the imaging system can be seen in Figure 3.11. There is a removable mirror which allows us to switch easily between the horizontal and vertical imaging depending on what is required. The horizontal imaging setup has a telescope which demagnifies the image by 3x, which leads to a large field of view. This enables us to observe all of the atoms trapped within the MOT, which is very useful for initial alignment and other diagnostic purposes. The BEC is only a few pixels though, so switching to the vertical imaging alleviates this problem, as it has a telescope which magnifies the image 2.6x. With this larger magnification the BEC can be seen more easily, and due to the vertical orientation it's better for time of flight (TOF) measurements.

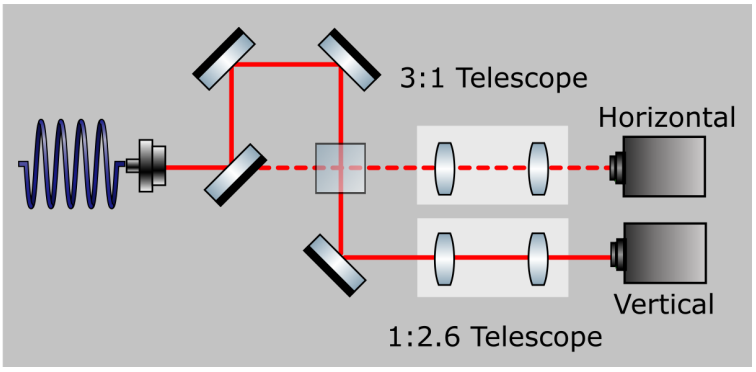

Figure 3.11: Optical schematic for the imaging system.

3.5.1 Imaging Techniques

To image the atoms, I use two main imaging techniques, absorption imaging and fluorescence imaging.

Absorption Imaging - In absorption imaging, a beam with a frequency close to that of the atomic transition frequency is incident on the sample, which leads to the atoms absorbing the light. This leaves a shadow of the beam intensity distribution, which is imaged by a CCD camera. In order to gain useful information from this, three intensity profiles are measured. First, the intensity profile of the laser travelling through the chamber with atoms, I_f, then the same but without atoms, I_0. The background light, I_b, is also measured, which is an image with no atoms and no laser light. Using these intensity profiles, the optical density, OD, can be calculated

$$OD = -\log\left(\frac{I_f - I_b}{I_0 - I_b}\right). \tag{3.1}$$

To transform this into a number of atoms, Beer's Law is used. With every pixel having an effective area, A, the total number of atoms, N, is given by:

$$N = \frac{A}{\sigma_{abs}} \sum_{i}^{\text{pixels}} OD_i. \tag{3.2}$$

Here, σ_{abs} is the absorption cross-section which is given by [101]:

$$\sigma_{abs} = \frac{6\pi c^2}{\omega_0^2 \alpha} \frac{1}{1 + 4\Delta^2/\Gamma^2 + I/I_s}, \tag{3.3}$$

where ω_0 is the atomic transition frequency, and α is the absorption coefficient. Combining the two expressions above leads to the total number of atoms:

$$N = \frac{A\omega_0^2 \alpha}{6\pi c^2} \left(1 + 4\frac{\Delta^2}{\Gamma^2} + \frac{I}{I_s}\right) \sum_{i}^{\text{pixels}} OD_i. \tag{3.4}$$

The absorption imaging technique is destructive, so a balance must be made between the imaging power and the measurable optical density of the sample. Using the vertical imaging setup, I can image BEC samples of $OD \approx 2.5$ with $\sim 10^5$ atoms.

Temperature Determination - For a thermal atomic sample, the size of the cloud depends on the temperature of the atoms and the expansion time. The following expression describes the expansion,

$$\sigma_{TOF}^2 = \sigma_0^2 + \frac{k_b T}{m} t^2. \tag{3.5}$$

σ_{TOF} is the standard deviation of the cloud density profile after a designated time of flight, t, while σ_0 is the standard deviation of the cloud density profile at $t = 0$. A Gaussian profile can then be fitted to the absorption images and their density profiles, leading to different values of σ_{TOF}, which are used to determine the temperature of the cloud [102].

Fluorescence Imaging - This technique relies upon stimulating and capturing the fluorescence of the atomic sample. To make the atoms fluoresce, they are illuminated for a short period of time by both the repumper and cooling lights. This brings the atoms into the cooling cycle, where they absorb photons from the laser to enter the excited state, then spontaneously emit a photon when they decay to the ground state. A camera then collects the emitted photons. The atom number, N, is related to the number of emitted photons, N_{ph}, by the scattering ratio, R_{sc}, which is given by

$$R_{sc} = \frac{N_{ph}}{N} = \frac{\Gamma}{2} \frac{I/I_s}{1 + \frac{I}{I_s} + 4\frac{\Delta^2}{\Gamma^2}}. \tag{3.6}$$

Here, Γ is the natural linewidth of the transition, I is the intensity, I_s is the saturation intensity, and Δ is the detuning of the laser frequency with respect to the transition frequency. N_{ph} is measured experimentally. The horizontal imaging system is the preferable orientation for fluorescence imaging, and with it, I am able to image an atomic cloud with as few as $\sim 10^6$ atoms within a volume of ~ 1 cm^3.

Chapter 4

The Building Blocks for a K-Rb Mixture

Within this chapter, I lay out the initial components that I used to explore the interactions between ^{87}Rb and ^{41}K atoms, following from the work seen in [69] and [70]. I describe how the experimental system can cool a sample of Rb atoms down to the BEC regime, alongside cooling K atoms to the sub-Doppler limit.

- **Section 4.1** goes into detail about how it is possible to create an all-optical BEC of ^{87}Rb atoms within the experimental setup. This begins by using laser cooling methods, starting from room temperature down to the Doppler limit, and then all the way to the BEC regime using evaporative cooling. I also briefly describe the BEC characterisation.
- **Section 4.2** explains the techniques that were used to cool ^{41}K from room temperature down to the Doppler limit using a MOT and compressed dark MOT.

4.1 An All Optical ^{87}Rb BEC

The initial step in creating the desired system was to create an all optical BEC of ^{87}Rb. The atoms are first cooled down from room temperature to a few tens of μK using laser cooling. The setup for this is shown in Section 3.2. The atoms are then transferred into a cross dipole trap, where they are cooled further using evaporative cooling. There are a couple of advantages that using an all-optical BEC has compared to other methods, such as magnetic RF evaporation. In RF evaporation coils carrying high current are required to perform the evaporation, these tend to be large and usually need to be constantly cooled. All-optical evaporation is comparatively simpler. The other advantage is that due to a lack of magnetic field in evaporative cooling, the magnetic sublevels m_F are degenerate, so atoms in any of the magnetic sublevels can be cooled to the BEC regime.

4.1.1 Experimental Sequence

To begin with, a cold atom flux is created within a 2D MOT, which is then transported to the 3D MOT in the main science chamber using a push beam. The 3D MOT is loaded for 5 s where the atom number saturates. The push beam and 2D MOT lights are then switched off. At this point, there are about 10^9 atoms at $\sim$ 300 μK within the 3D MOT. The first dipole trapping beam, which has a wavelength of 1070 nm, is then switched on to full power to ready it for later stages.

The atoms then need to be cooled below the Doppler limit, this is done using a temporal dark MOT where the atoms reach $\sim$ 50 μK. Section 4.1.3 explains this step in more detail. Once this stage is complete, the atoms are loaded into the dipole trap. At the same time, all of the MOT cooling lights and the magnetic quadrupole field are turned off. Once the atoms are in the dipole trap, the evaporative cooling begins by slowly reducing the power of the 1070 nm dipole trap beam, while also introducing the crossed 1550 nm beam which also

has its own power reduced with time. The values of the beam powers for each evaporation stage can be seen in Table 4.1.

Table 4.1: The power of the dipole trap beams at the beginning of each stage of the evaporative cooling.

Stage	1070 nm Power (W)	1550 nm Power (W)	Time (ms)
Ramp 1	11.5	0	80
Ramp 2	5.18	0	70
Ramp 3	4.88	0	700
Ramp 4	2.55	3.68	800
Ramp 5	1.5	3.63	600
Ramp 6	0.24	3.53	900
Ramp 7	0.073	1.89	1250
Ramp 8	0.022	1.27	N/A

The Rb atoms are then held in the trap at their final power values for 20 ms to allow for a final rethermalisation before they are released for TOF imaging. Within the next few parts, I will talk in more detail about the individual stages of the cooling process.

4.1.2 Loading Rb atoms in 3D MOT

The atoms begin their journey in the 2D MOT, where they are confined in two dimensions and cooled using Doppler cooling. This creates a cold and dense flux of atoms at a rate of $\sim 10^9$ atoms/s with a speed of $\sim$ 10 m/s. The atoms are then moved to the main science chamber by a push beam where they are loaded into the 3D MOT, which cools and confines the atoms in three dimensions. After $\sim$ 5 s of loading into the 3D MOT, I typically have $\sim 5\times10^9$ atoms at $\sim$ 300 μK. This dual MOT system allows for efficient loading of atoms into 3D MOT [103].

For both of the MOTs Doppler cooling is performed, utilising the D_2 line transitions of Rb as shown in Section 3.2.1. The process requires both a cooling and repumper laser to keep an efficient cooling cycle. The light also needs to be correctly circularly polarised in

order to excite the correct m_f sublevels due to the quadrupole magnetic field making them energetically different due to Zeeman splitting.

The beams are red-detuned from resonance, with the 3D cooling having Δ_{cool} = -2.5Γ and the value for the 2D cooling being -1.5Γ. Γ is natural linewidth of the Rb D_2 line [95]. On the other hand, the repumper beam is set on resonance with repumper transition, while the push beam is set on resonance with the cooling transition. Both MOTs have a magnetic field gradient of 10 G/cm.

4.1.3 Rb Dark MOT

Once the atoms are trapped within the 3D MOT, they need to be cooled further in order to successfully trap them in the dipole trap. This is done using the well known technique of a temporal dark MOT [104] [105]. To begin with the repumper power is reduced, meaning the atoms fall out of the cooling cycle into the $|F = 1\rangle$ dark state. Within this dark state the atom has reduced accessibility from the cooling light, which leads to a reduction in rescattered radiation and excited state collisions. The dark MOT stage leads to an increase in phase space density and a further decrease in temperature. The atoms are also contained within a smaller volume within the magnetic field minimum, which can enhance other cooling processes like gradient polarisation cooling.

Experimentally, the repumper power is reduced from $\sim$ 5 mW to $\sim$ 10 μW in 50 ms. The cooling light is then detuned from Δ_{cool} = -2.5Γ to Δ_{cool} = -10Γ in 150 ms. The detuning of the cooling light is changed to interact with the hotter atoms, as they have a higher velocity, meaning a larger Doppler shift which requires a larger red detuning. During this stage the temperature reduces down from 300 μK to 50 μK, which is below the Doppler limit of 146 μK.

4.1.4 Evaporative Cooling

In order to reach the BEC regime I use an all-optical evaporative cooling stage. The atoms from the dark MOT are loaded and trapped within a crossed dipole trap. The setup for this can be seen in Section 3.2.2. For an alkali atom using linear or unpolarised light, the dipole trapping potential, U_d is given by [106]

$$U_d(\mathbf{r}) = \frac{\pi c^2 \Gamma}{2} \left(\frac{2}{\omega_2^3 \Delta_{2,F}} + \frac{1}{\omega_1^3 \Delta_{1,F}} \right) I(\mathbf{r}), \tag{4.1}$$

where ω is the laser frequency, and $\Delta_{1,F}$ and $\Delta_{2,F}$ are the laser detunings with respect to the D_1 and D_2 lines.

The dipole lasers, wavelengths 1070 nm and 1550 nm, are both red detuned with respect to both spectral lines, thus, the minimum of the potential is located at the maximum intensity of the beams. They are Gaussian beams, so atoms are trapped at the beam focus where intensity is maximum. Once the atoms are trapped in the potential, evaporative cooling is performed. To do this, the power of the dipole trap lasers is reduced, removing the hottest atoms as the trap depth decreases. This process must be done slowly enough for the atoms in the trap to have time to rethermalise through elastic collisions.

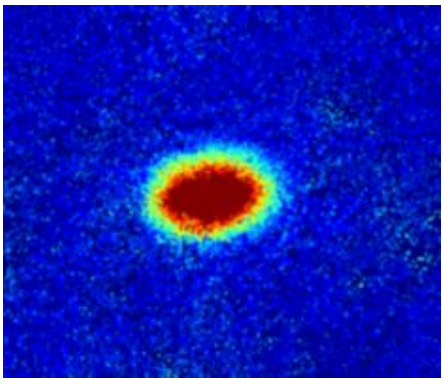

Figure 4.1: An absorption image of a BEC of 56 x 10^3 ^{87}Rb atoms after 20 ms time of flight.

4.1.5 BEC Characterisation

In order to characterise the BEC, the critical temperature, T_c must be determined, this is a function of the trapping frequencies, ω_1, ω_2 and ω_3. T_c can be determined experimentally, starting from its definition in a system with N particles

$$T_c = \frac{\hbar\bar{\omega}N^{1/3}}{[\zeta(3)]^{1/3}k_B} \approx 0.94\frac{\hbar\bar{\omega}}{k_B}N^{1/3}, \tag{4.2}$$

with $\bar{\omega} = (\omega_1\omega_2\omega_3)^{1/3}$ being the geometric average of the trapping frequencies, and ζ the Riemann zeta function. The next step is to substitute Equation 4.2 into the condensed fraction

$$F = \frac{N_0}{N} = 1 - \tau^3, \tag{4.3}$$

Where N_0 is the number of particles in the ground state, and $\tau = T/T_c$, which leads to

$$N_0 = \max\left[N - \left(\frac{k_BT}{0.94\hbar\bar{\omega}}\right)^{1/3}, 0\right]. \tag{4.4}$$

The relation between a trapping frequency and the trapping potential is then considered [106]

$$\omega_i = \sqrt{\frac{2\hat{U}}{mw_i^2}}, \tag{4.5}$$

where $\hat{U}$ is the first order term of the Taylor expansion of the trapping potential in the direction of the trapping frequency, m is the atom mass and w_i is the beam waist. As the temperature of the atoms is dependent on the trap depth, $\hat{U}$ is proportional to the temperature. It is then possible to write $\bar{\omega} = \beta T^{1/2}$, with β being a constant. So Equation 4.4 can be written as:

$$N_0 = \max\left[N - \left(\frac{k_BT}{0.94\hbar\beta T^{1/2}}\right)^3, 0\right] = \max[N - \alpha T^{3/2}, 0], \tag{4.6}$$

where $\alpha = [k_B/(0.94\hbar\beta)]^3$. Experimental data can be fit to Equation 4.6 to find T_c, where the condensed fraction, $N_0 > 0$. This requires the values of the trapping frequencies to be found.

The trapping frequencies can be measured using parametric heating. I first apply a sinusoidal modulation to the dipole traps power with a certain frequency, ω_m, for a short period of time after the evaporation stages. When the frequency of the modulation is twice the fundamental frequency of the trap, $\omega_m \approx 2\omega_i$, the modulation introduces energy into the system, which heats it, leading to a loss of atoms from the trap. I then inspected the resonant like behaviour to acquire the three trapping frequencies, which for full evaporation leads to $\omega_i = (60.2 \pm 0.4, 91 \pm 1, 128 \pm 2)$ Hz.

From these trapping frequencies, the critical temperature, $T_c \approx 350$ nK for the BEC. This can also be visualised from when the optical density profile of the atomic sample changes from a thermal distribution to a bimodal one. The bimodal distribution is the combination of a Thomas-Fermi distribution that describes the BEC and the Gaussian that describes the thermal component.

4.2 K Cooling and Trapping

The main purpose of my study was to trap a single ^{41}K atom and immerse it in a bath of ultracold ^{87}Rb atoms, which could eventually realise a single atom quantum heat engine. With the ultracold Rb accounted for, as I can go as far as the BEC regime, the next step was to figure out how to trap a single atom using an optical tweezer. In order for this to happen, I first needed to cool down the ^{41}K atoms to an appropriate temperature.

4.2.1 K MOT and DMOT

Like ^{87}Rb, I used a MOT and other laser cooling techniques to reduce the temperature of the K atoms. As before, Doppler cooling is performed using the D_2 line to create a closed cooling cycle, while the same hyperfine transitions as Rb are used for the purposes of cooling and repumping. The beam powers for the MOT stage can be seen in Table 3.1, with the time being 0.5 s, which is shortened to 200 ms when attempting to capture a single atom. For K atoms, the repumper light needs to be detuned, as there is overlap in the function of the cooling and repumper light due to the small excited state hyperfine separation, explained in Section 3.2.1. The detunings are set to $\Delta_{\text{cool, K}}$ = -2.5Γ_K and $\Delta_{\text{rep, K}}$ = -1.3Γ_K for the cooling and repumper beams respectively, where Γ_K is the natural linewidth of the D_2 line of K [96]. As the repumper is not on resonance due to being red detuned it exerts a viscous force on the atoms, meaning the six MOT beams must have their power balanced.

Due to the difficulties mentioned above, the Doppler cooling of ^{41}K is not that effective. This results in a MOT that has a temperature of $\sim$ 1 mK. To cool the atoms further, I implemented a compressed dark MOT stage [107]. To begin with, the power of K cooling and repumper are decreased. The repumper is then red-detuned very slightly by $\sim$ 1 MHz, while the cooling detuning is shifted to $\Delta_{\text{cool, K}}$ = -Γ_K. The magnetic field strength is also increased from 10 G/cm to 20 G/cm. This results in a cooler sample, which surpasses the Doppler limit T_D^K = 125 μK, as well as a more dense cloud of atoms, which leads to an increase in the single atom loading rate of the optical tweezer.

Chapter 5

Single Atom in a Tweezer - Towards a Single Atom Quantum Heat Engine

Within this chapter, I lay out the design formulated to realise a single atom quantum heat engine, and how I eventually trapped a single atom of ^{41}K.

- **Section 5.1** shows the development of a species-selective optical tweezer in my experiment. This includes the calculation of the trapping potentials and heating rate for both Rb and K atoms in the tweezer. It then moves onto how only a single atom is loaded into the trap, taking advantage of the collisional blockade mechanism.
- **Section 5.2** details how I use fluorescence imaging to examine the single atom. This section also details how the fluorescence images are converted into usable data, using the photon counts in each pixel to estimate the number of atoms captured during each experimental run. This can produce information about the tweezer characteristics, including the trapping frequency.

5.1 Developing a Species Selective Optical Tweezer

In order for the optical tweezer to be species selective, the wavelength must be chosen so that it only creates a potential for one of the species. Using again the expression

$$U_d(\mathbf{r}) = \frac{\pi c^2 \Gamma}{2} \left(\frac{2}{\omega_2^3 \Delta_{2,F}} + \frac{1}{\omega_1^3 \Delta_{1,F}} \right) I(\mathbf{r}), \tag{5.1}$$

the dipole potential can be calculated as a function of the wavelength. This has been plotted in Figure 5.1 for both Rb (red) and K (blue), alongside the atomic polarizabilities for both species in Figure 5.2. The tune-out wavelength can be seen marked by a dashed line on the plot, which is a wavelength where the dipole potential for Rb is zero, while still acting upon the K atoms. For a tweezer with wavelength of 789.820 nm, power of 25 mW and a waist $w = 2$ μm, the calculated trapping frequencies are $(f_x, f_y, f_z) = (15.7, 153, 153)$ kHz, where the x direction is the axial direction of the tweezer.

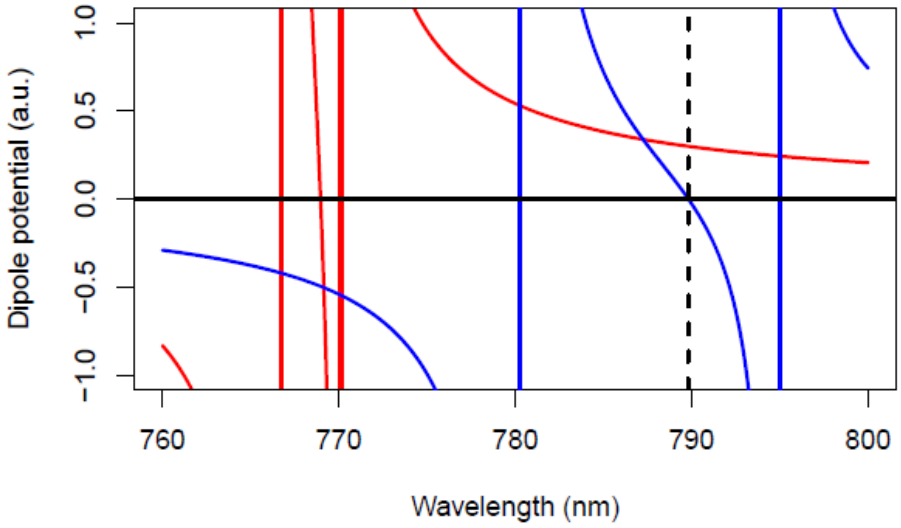

Figure 5.1: Dipole potential for Rb (blue) and K (red) as a function of the laser wavelength. The tune-out wavelength for Rb is represented by the vertical dashed line (789.820 nm).

For this specific system, the 'tune-out wavelength' doesn't exhibit zero potential for the Rb atoms. It can be seen from [62], when there are atoms in a very tightly confined trap

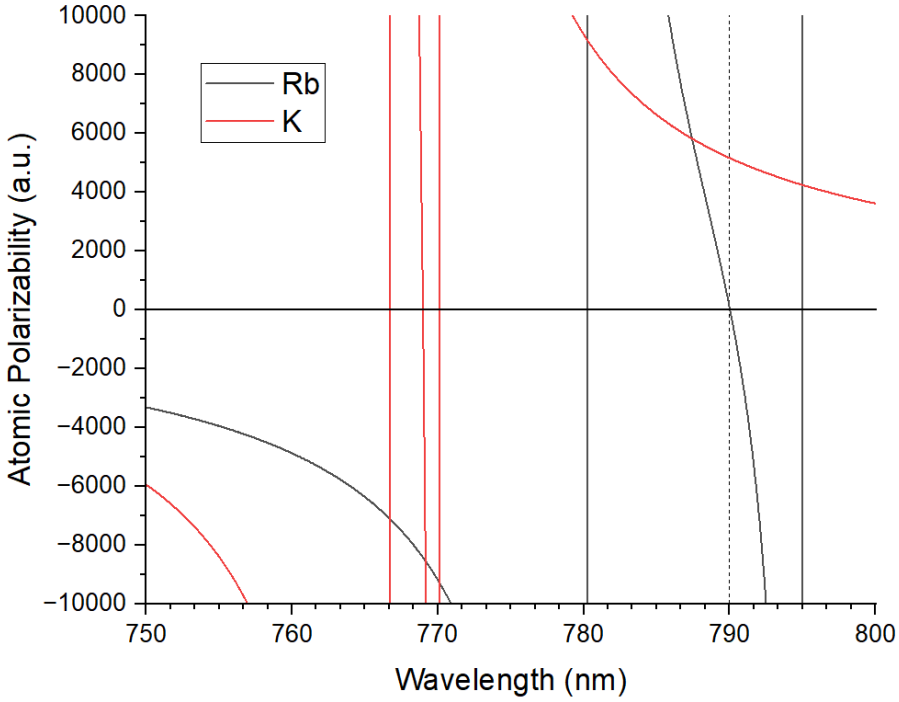

Figure 5.2: Atomic polarizability for Rb and K as a function of the laser wavelength. The tune-out wavelength for Rb is represented by the vertical dashed line (789.820 nm).

with a beam waist $w \sim \lambda$, polarisation effects which are associated with the breakdown of the paraxial approximation can strongly impede coherent manipulation and cooling. Such tightly focused beams have longitudinal polarisation components, which, even if the input field is linearly polarised, result in a spatially varying elliptical polarisation. This affects the trapping potentials and impairs cooling. Described using ray optics as in [62], the light enters the microscope objective with transverse linear polarisation, as parallel rays. When refracted by the objective, the polarisation of these rays must also deflect to remain transverse to the ray [108]. Then, in the diffraction limited volume around the focus, all the rays interfere, creating a field which is elliptically polarised. This creates a small light shift and alters the trapping potential on the atoms near the focus. Solutions to this issue are explored in Section 7.1.

5.1.1 Heating Rate

Another aspect that needs to be calculated is the heating rate of the atoms due to the dipole trap. Even if the trapping potential for Rb is zero, there will still be some heating effects. Using an equation from [106] the heating rate, $\dot{T}$, can be calculated. For a harmonic dipole trap, this is

$$\dot{T} = \frac{2}{3} T_{\mathrm{rec}} \bar{\Gamma}_{\mathrm{sc}}, \tag{5.2}$$

where T_{rec} is the recoil temperature of the atom and $\bar{\Gamma}_{\mathrm{sc}}$ is the mean photon scattering rate, which is estimated as the photon scattering rate at the centre of the trap. The photon scattering is at a maximum at the centre of the trap, yielding an upper limit to the heating rate.

$$\Gamma_{sc} = \frac{\pi c^2 \Gamma^2}{2} \left(\frac{2}{\omega_2^3 \Delta_{2,F}^2} + \frac{1}{\omega_1^3 \Delta_{1,F}^2} \right) I(\mathbf{r}_0). \tag{5.3}$$

For my specific tweezer parameters, this leads to heating rates of 132 μK/s and 664 μK/s for the K and Rb atoms, respectively. The temperatures I wish to reach for both species are of the order of 1 μK, with the interaction timescale on the order of 10 ms. Using this, the atoms will be heated by $\sim$ 1 μK during this time. To prevent any unnecessary heating of the Rb atoms a nanopositioner is used. This loads the K atoms in the tweezer 40 μm away from the ultracold Rb atoms during the experiments in which they interact. This will be explained in more detail in Chapter 7.

5.1.2 Collisional Blockade

Optical tweezers are very narrow waisted dipole traps, and in the case of this experiment it will only trap a single atom. In order to load only a single atom, I take advantage of the mechanism known as the collisional blockade. Over many loading events, this leads to an average loading of 0.5 atoms in the tweezer, which can also be described as the loading

of exactly one atom. The description of this regime uses the model set out in [109]. The number of atoms in the trap is described as

$$\frac{dN}{dt} = R - \gamma N - \frac{\beta}{V} N(N-1), \tag{5.4}$$

where R is the loading rate, $-\gamma N$ describes the one-body decay (due to collisions with fast atoms from the background gas), and $-\beta/V N(N-1)$ describes the two-body decay (due to a variety of inelastic collision mechanisms), where β is independent of the volume, V. The volume is approximated as [110]

$$V = \pi w_0^2 z_R \ln \frac{1}{1-\eta} \sqrt{\frac{\eta}{1-\eta}}, \tag{5.5}$$

w_0 is the tweezer waist, z_R is the Rayleigh length and $\eta = k_B T/|U_0|$, where U_0 is the potential depth. The volume depends on the waist, leading to different loading regimes of the trap. Other techniques, such as light induced collisions due to blue detuned light, can be used to assist the collisional blockade process [111]. Due to the waist of my tweezer being larger than desired, this may have helped with tweezer loading.

5.1.3 Tweezer Loading

For the most efficient tweezer loading, the atomic sample needs to be cold and dense. The following is the base sequence I use to cool and then trap ^{41}K atoms in the optical tweezer. Throughout the different experiments, this sequence was slightly modified depending on the needs.

To begin with, the MOT is loaded with ^{41}K atoms for 30 ms. This is followed by a dark MOT stage for 20 ms, which is the same as the one seen in Section 4.2. The dark MOT cools the atoms from ~ 1 mK reached in the K MOT down to the Doppler limit, 125 μK. The dark MOT is then compressed by increasing the magnetic field gradient from 10 G/cm to 20 G/cm,

increasing the atomic density. During the compressed dark MOT stage, the tweezer light is switched on, and is overlapped with compressed MOT for 20 ms. The atoms are now loaded into the tweezer. Depending on the sequence, the tweezer light is then ramped down, the initial and final intensity values are dependent on the goals of the particular experiment, and are explored further in Section 6.2 for single atom thermometry and Section 7.1 for the single atom as an impurity. As the tweezer waist ~ 2 μm (see Section 5.2.2), a majority of the K atoms within the MOT will not be trapped. So there is a wait time of 95 ms after the K MOT lights are shut off, so the atoms that are in the K MOT that weren't captured will escape.

5.2 Examining the Single Atom

5.2.1 Fluorescence Imaging

In order to examine the single atom, I use fluorescence imaging. The techniques used here were inspired by the works seen in [112] and [113]. When using fluorescence imaging for the MOT, the cooling and repumper lights need to be tuned to resonance in order to maximise the scattering of light by the atoms. This will heat up the atoms, leading to losses from the trap. This is not ideal when trying to image very few atoms or even a single atom. Instead, the imaging light needs to be red-detuned, which helps keep the temperature low and reduces the losses. This increases the time in which the atoms can be imaged, with most of my experiments using an exposure time of 50 ms.

The light used to induce the fluorescence comes from the two opposing vertical beams at a reduced intensity compared to the MOT values. Alongside this are two side beams of waist ~ 1 mm and power ~ 50 μW, which are retro-reflected and correctly circularly polarised. These act the same as the horizontal MOT beams would, except with a far smaller intensity

to reduce scattering. They were aligned by overlapping them with the K DMOT, so they can excite the atoms in the tweezer.

Scattered photons from the atoms in the tweezer are collected by a microscope objective, which is the same one that focuses the tweezer light. The collected light is then focused onto a single pixel of a CMOS camera (model Hamamatsu ORCA Flash 4.0 V2). The fluorescence signal was optimised by changing the detunings of the cooling and repumper lights during imaging. The optimal detunings were found to be $\Delta_{\text{cool, K}} = -0.66\Gamma_K$ and $\Delta_{\text{rep, K}} = -0.75\Gamma_K$ for the cooling and repumper beams, respectively. When optimising these parameters, the tweezer light is not ramped down, therefore there are a greater number of atoms remaining in the trap, between 5 and 8. Section 5.2.3 goes into detail about how to identify the number of atoms trapped in the tweezer, by inspecting photon counts.

An unfortunate side effect of the tweezer light is that it induces light shifts of the hyperfine energy levels. These light shifts strongly impact the fluorescence imaging due to the small frequency difference between the hyperfine energy levels in the excited state manifold of ^{41}K. This results in detrimental effects, such as fluctuating dipole force heating [114], inhomogeneous detunings and impaired laser cooling due to the breakdown of hyperfine coupling [115], which is needed to perform the fluorescence imaging of the single atom. The light shifts can even be large enough to cause difficulties loading K atoms from the dark MOT. To solve this, I utilise a solution developed in [116], which involves chopping the fluorescence and tweezer lights. Both lights are switched on and off alternatively, so that when one is on, the other is off. To avoid parametric heating, the chopping frequency has to be much greater than the tweezer trapping frequency, which is on the order of tens of kHz. It must also be approximately less than $\Gamma/2\pi$, where Γ is the natural linewidth of K, to allow the atom enough time to decay to the ground state before the light is switched back on. I set the chopping frequency at 1.08 MHz, which was found to be optimal for the setup. As the frequency is so high, this can be considered an adiabatic process, which leads to the effective

trap depth being half of the original one. To resolve this, the power of the tweezer beam is increased. Another note is that even though the MOT and tweezer power oscillations should theoretically be in anti-phase, it was found that the optimal phase between the signals was 290 degrees. This is possibly due to some electronic delay, as well as the time the atoms spend in the excited state.

5.2.2 Tweezer Characteristics

Once the sequence is set up, there needs to be a way to gain information from the fluorescence images. An example of such an image can be seen in Figure 5.2.1. The number of photon counts incident on each pixel of the CMOS camera is received by a computer. It is then possible to select a region of interest to sum the photon counts in a particular area, enabling the characterisation of the atoms.

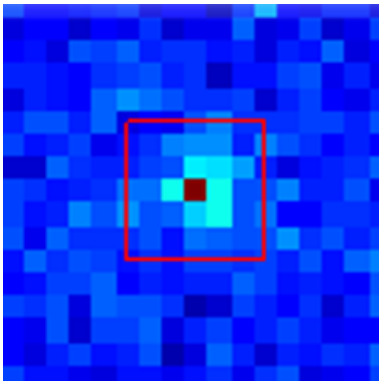

Figure 5.3: A fluorescence image of the K atoms trapped in the optical tweezer. The red square represents the region of interest.

Using the parametric heating method seen in 4.1.5, the radial and axial trapping frequencies of the optical tweezer can be identified. For my impurity experiments seen in Chapter 7 the power of the tweezer incident on the atoms is set to 0.7 mW. The results of this can be seen in Figure 5.4a (axial) and Figure 5.4b (radial). These yield a result of $\omega^{(K)} = 2\pi \times (1.4, 22, 22)$ kHz. The two radial frequencies are identical due to the geometry

of the tweezer. This yields a waist of 2.1 μm, a tweezer intensity of 10.11 kW/cm^2, and a trap depth of 0.12 mK. I also initially trap the atoms at 7.5 mW before ramping down to 0.7 mW, which from calculations find the trapping frequencies $\omega^{(K)} = 2\pi \times (4.6, 77, 77)$ kHz, and a trap depth of 1.28 mK.

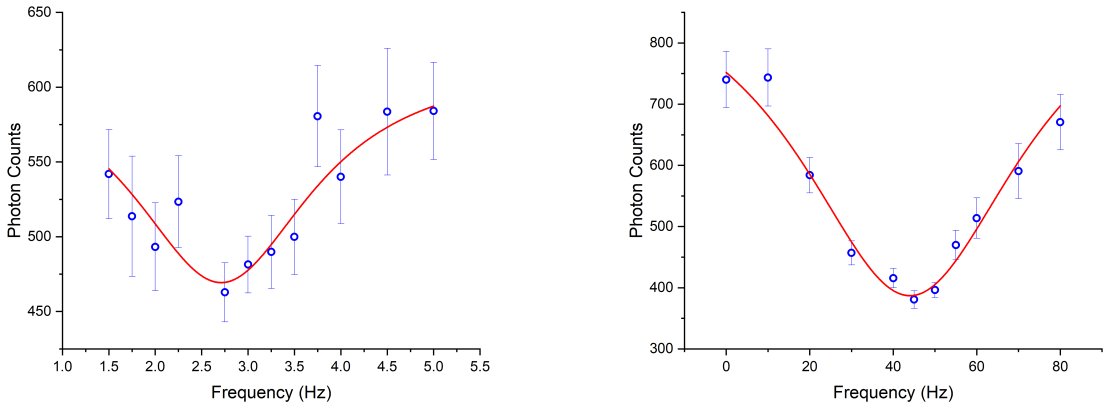

(a) Identifying the axial frequency of the optical tweezer.

(b) Identifying the radial frequency of the optical tweezer.

Figure 5.4: Photon counts versus the optical tweezer modulation frequency.

5.2.3 Mapping Photon Counts into Atom Numbers

The next step is to identify the number of atoms trapped in the tweezer. An appropriate region of interest is first selected, and the photon counts within that region are summed and plotted in a histogram. After many experimental runs, a histogram is produced, an example of which can be seen in Figure 5.5. It can be described as a calibration histogram, where the photon counts produce a multimodal distribution, with each peak being associated with a different number of atoms in the trap. Here two peaks can be seen which correspond to the background (zero atoms) and a single atom. To confirm the first peak is the background, a histogram is taken using a sequence where K atoms are not loaded into the tweezer, due to no MOT loading, which leaves only the first peak. The calibration histogram is taken before

each set of measurements and periodically repeated to confirm experimental stability.

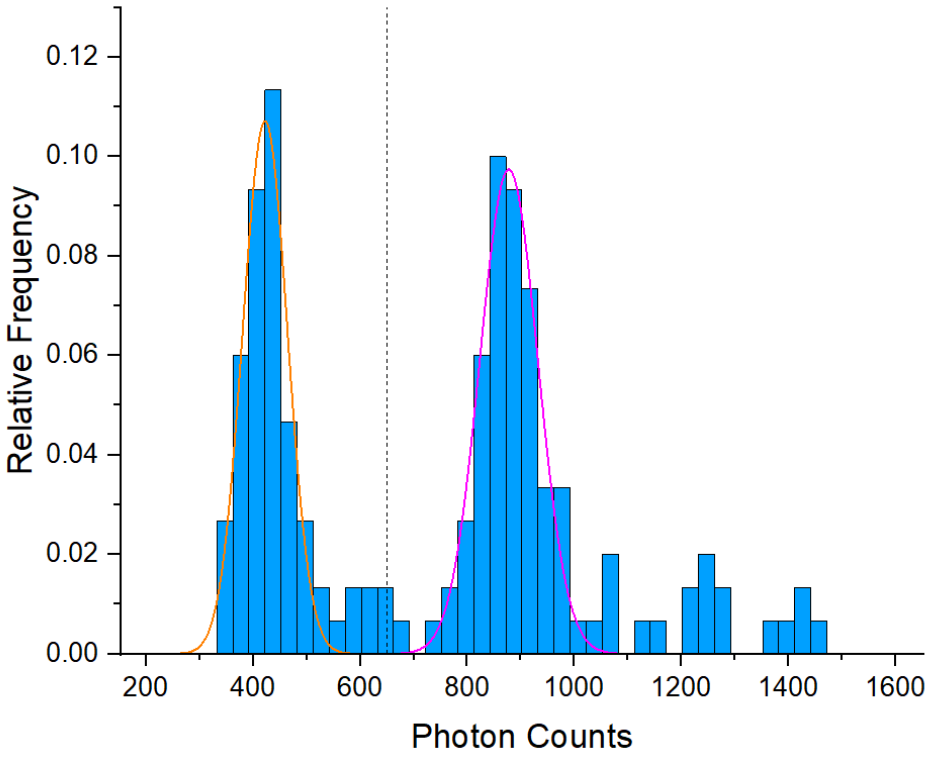

Figure 5.5: A histogram of the collected photon counts from the optical tweezer. A multimodal Gaussian fit is applied to identify the peaks corresponding to different atom numbers. The zero atom peak is centred at 422.1 ± 9.4 with width 83.7 ± 18.8, while the one atom peak is centred at 877.5 ± 11.4 with width 108.6 ± 22.8.

Once the histogram has been taken, a multimodal Gaussian fit is applied to the data. This gives the position m of the background (zero atom) peak, and the spacing Δ between the peaks. I found Δ to be constant in data sets with more than two peaks. From this information, the conversion from photon counts to atom number can be written as

$$n_i = \text{round}\left(\frac{n_{p,i} - m}{\Delta}\right), \tag{5.6}$$

where n_i and $n_{p,i}$ are the number of atoms and photon counts respectively for a given experimental shot i. The resulting value is mapped to an integer value of the atom number

for the nearest peak. For the example in Figure 5.5, $m = 477$ and $\Delta = 564$.

In order to distinguish the number of atoms trapped within the optical tweezer it's possible to define a photon count threshold. To find the optimal threshold, the imaging fidelity needs to be found, laid out within [117] and also used within [118]. If the photon count is above this threshold, then an atom is present in the trap. Some caveats to this are that very few photons may be collected even though an atom is in the trap, leading to a false negative. As the exposure time is 50 ms, it is also possible that the atom may be lost throughout the imaging, leading to the counts seen between the two peaks in Figure 5.5. The imaging fidelity is found by calculating the overlap between the two Gaussians for the zero and single atom cases. Maximising the fidelity leads to the correct value for the detection threshold.

Chapter 6

Single Atom Thermometry

This chapter is a reformatted, slightly adapted copy of our paper seen in [71]. It lays out the work done on single atom thermometry in collaboration with a team at the University of Exeter. It displays the advantages of combining my experiments capabilities with their theoretical work.

- **Section 6.1** introduces our Bayesian method. I also describe a simple analytical model for the recapture probability. Three different thermometric protocols are then set out, and their performance is compared. These protocols are the base Bayesian processing of data captured at unoptimised times, followed by the repeated measurements at an *a priori* optimal time, and a fully adaptive method.

- **Section 6.2** contains details on the experimental setup, and how the real data are taken and processed.

- **Section 6.3** ranks the different thermometric protocols in terms of estimate variability and asymptotic convergence speed. It also shows how information maximisation reduces the required number of measurements for estimated to converge to a target precision

- **Section 6.4** displays our conclusions.

By exploiting the Bayesian methods in [40], an adaptive strategy was developed to optimally assess the temperature of single or few atom systems. Given a set of measurement outcomes, and a model for the experiment, we can find the estimate that minimises, on average, a suitably defined error. Most importantly, the shot to shot information gain can be computed, which would allow us to adjust and update the experiment in real time, so that we receive the maximum information for each measurement.

Within this chapter, the benefits of this new adaptive Bayesian framework will be shown when applied to my experiment. In this case, it will be the optimisation of a release-recapture thermometry experiment using a few ^{41}K atoms tightly confined within an optical tweezer at a temperature regime of a few μK. We are exploring Bayesian thermometry, as precise thermometry in this type of system is extremely expensive when it comes to the number of repetitions required to measure a single temperature. As explained before, a method such as time of flight imaging cannot be used due to the low optical density of the atoms within the tweezer. Looking to other methods such as Raman sideband spectroscopy, the atoms in question are too hot for this method to operate. This leaves us with the release-recapture method, which has two main drawbacks which our optimisations look to overcome. The first being the large number of experimental repetitions, the second is that it tends to be less accurate than other methods. The control parameter for this optimisation is the light-off time of free expansion of the atoms.

6.1 Adaptive Bayesian Thermometry

For this section, I refer to the Bayesian data analysis and global thermometry set out in Section 2.4.

6.1.1 Release Recapture Method

A release-recapture thermometry experiment begins with a trap which confines an ultracold gas at a temperature T. The trap is then switched off momentarily for a time t, leading to the atoms expanding ballistically. After the trap is reactivated, fluorescence imaging is used to measure the number of recaptured atoms n. To acquire the temperature, we must fit the measurement outcomes at different times to a model $f(T,t)$, which represents the fraction of recaptured atoms [28].

The simplest case is when only a single atom is loaded into a trap. In this case, the probabilities for recapturing or losing the atom after time t_i are

$$p(n_i = 1|T, t_i) = f(T, t_i), \tag{6.1a}$$

$$p(n_i = 0|T, t_i) = 1 - f(T, t_i), \tag{6.1b}$$

this gives us the required likelihood model. We now need to calculate the recaptured fraction $f(T,t)$. The trapping potential is created by focusing a beam down to a narrow waist, which produces tight confinement in the radial directions (transverse x-y plane). This potential is described by

$$U(r) = -U_0 \exp\left(-\frac{2r^2}{w_0^2}\right), \tag{6.2}$$

where U_0 is the trap depth, as in Equation 5.1, w_0 is the beam waist, and $r^2 = x^2 + y^2$. In the low temperature regime, at low T, where $U_0 \gg k_b T$, Equation 6.2 leads to [119]

$$f(T,t) = \frac{1}{g(\eta)} g\left[\frac{\eta W(\tilde{t}^2)}{\tilde{t}^2}\right], \tag{6.3}$$

where $g(s) = 1 - e^{-s}$, $\eta = U_0/(k_B T)$, $\tilde{t}^2 = 4U_0 t^2/(m w_0^2)$, m is the mass of the atom, and $W(\cdot)$ is the Lambert function, defined implicitly as $W(s)e^{W(s)} := s$.

In order to estimate T in practice, we choose a range of release times $\{t_1, ..., t_\nu\}$ in order

to monitor the decay of $f(T,t)$. At each time t_i, α_i independent photon count measurements are taken, to infer the number of recaptured atoms $\{n_{ij}\}_{j=1}^{\alpha_i}$. Once all the measurements have been taken, we get the average $\bar{n}_i$ for every t_i. These are then fitted to $\lambda f(T,t)$ using the least squares method. Here, the release time t acts as an independent variable, while T and λ are fitting parameters.

There are two main issues here. In order to assume that the empirical average $\bar{n}_i$ is close enough to its real value, we require a very large number of repetitions α_i. [120, 121]. The second issue regards the fact we discard most of the information to use the average $\{\bar{n}_i\}$ even though we have the entire measurement record $\{n_{ij}\}$. These problems lead to potentially unreliable results and a loss of precision. These are solved when using the Bayesian estimation framework of global thermometry.

6.1.2 Adaptive Maximisation of the Information Gain

During this part, I will discuss how the Bayesian methods can be used to process the data from conventional release-recapture experiments. Then, moving onto how Bayesian data analysis can improve how the measurements are taken and processed. First, seeing how the validity of Equation 6.3 relies on the fact that we remain in the low temperature regime where $U_0 \gg k_b T$, this means that the unknown T sets the energy scale in which this model is applicable. Thus, we have a scale-estimation problem, where Equations 2.17-2.21 are applicable. We also need to start with a choice for our temperature range $[\theta_{min}, \theta_{max}]$. For the lower bound, we choose 5% of the trap depth, as the atoms are not expected to reach this temperature, even during the final stages of cooling. Then for the upper bound, we choose the temperature where Equation 6.3 starts to break down.

6.1.2.1 Unoptimised Bayesian Protocol

We begin by considering a basic release-recapture experiment, as described in Section 6.1.1. For this case, the vector $\mathbf{t}$ of release times is

$$\mathbf{t} = (\underbrace{t_1, ..., t_1}_{\alpha_1 \text{ times}}, ..., \underbrace{t_\nu, ..., t_\nu}_{\alpha_\nu \text{ times}}). \tag{6.4}$$

The values of t_i can be chosen in order to see all the important features of the decay of the survival probability in Equation 6.1. After receiving the measurement record ($\mathbf{n}$,$\mathbf{t}$) it can then be processed, which results in better estimates than the least-squares fit, as we're making use of all the available data. Before this study, the data taken by the experiment were processed using the least-squares fit.

The issue here is not all the expansion times t_i provide the same amount of information. For example, when the temperature is low, and you inspect the low release times, the change in survival can be too small to identify. As the atoms are cold, they're unlikely to move far over these times. Instead, we want to look at longer release times. For large T, it's the opposite. The atoms are hot, and can be lost from the trap quickly, meaning the best information is at low release times. If we were to continue to take our data in this manner, by evenly sampling each time interval, we would end up with a great number of uninformative data points. As data is collected, we feed it to the temperature information to update it. As this happens, we should ideally focus our efforts on taking data at the times t_i which yield the most information. This will speed up the convergence of the temperature estimate, and reduce the spread of estimates from a small sample size.

6.1.2.2 *a priori* Optimisation of the Expansion Time

Even without any measured data, and starting from a maximum ignorance of T, we still start with some amount of information, the trap parameters. In this case, those of the optical tweezer. We can then use this information to determine an optimal expansion time t_s for the first measurement run. This is done by searching for a time when $\mathcal{K}(t)$ in Equation 2.21 is maximised, which is even possible before any measurements are taken. In the simplest case, we would take t_s, and perform every single measurement using this release time, as in

$$\mathbf{t} = (\underbrace{t_s, ..., t_s}_{\mu \text{ times}}). \tag{6.5}$$

Knowing that the most uninformed shot is the first one, if we keep its uncertainty low, we increase the speed of the convergence of our estimate to the true temperature as we update our information [122–124].

6.1.2.3 Adaptive Optimisation of the Expansion Time

Instead of using the single release time t_s generated in the *a priori* method, we can update this optimal time after each run of the experiment. This maximises the information content of the posterior probability adaptively. The steps are

1. given the prior $p(\theta)$ and the likelihood $p(n|\theta, t)$ for the first shot, maximise $\mathcal{K}(t)$ over t to find $t_1 = t_s$ as in the *a priori* method;

2. perform a measurement at the optimal time $t_1 = t_s$ to record n_1;

3. normalise $p(\theta)p(n_1|\theta, t_1)$ using it as the new prior for the next run; reapply step 1 and 2 to find t_2 and n_2;

4. repeat μ times. The data can then be processed with Equations 2.18 and 2.19.

6.1.3 Performance Comparison on Single Atom Simulations

We next performed some preliminary tests to compare the different Bayesian methods described above alongside the nonlinear least squares fitting method. We simulated a trap loaded with exactly one atom, with a trap depth of $U_0/k_B = 29$ μK and a beam waist of $w_0 = 1.971$ μm. The temperature is set to $T = 40$ μK for these simulations. These parameters are the same as the ones in the physical experiment.

An analytical method is used, as described in [28], also described above. This yields the number of recaptured K atoms after a recaptured time t. First, the atoms in the trap are assumed to be at $x = y = 0$ at $t = 0$. They are then released, with velocities drawn from a Maxwell-Boltzmann distribution, where they expand radially from the centre. The potential energy at the new position is compared to the kinetic energy of the atom at time t. Atoms are considered 'lost' if their kinetic energy is greater than the potential energy. From this, a maximum initial velocity for any recaptured atoms can be deduced. The Maxwell-Boltzmann distribution is then integrated up until this maximum velocity, which leads to the recaptured fraction N/N_0, where N_0 is the number of atoms initially trapped within the tweezer. Two assumptions are made, the first is that the method doesn't account for gravity, which in reality may not be negligible. Then, due to the very elongated trap, the trapping in the z-direction is assumed to be negligible. It is possible to also use a classical Monte-Carlo method as seen in [125], which takes gravity into account. In this method, the atoms are modelled as non-interacting point masses which experience both gravitational and dipole trap forces.

For the nonlinear and unoptimised Bayesian methods we choose the release times to be (5, 10, 20, 30, 50, 70, 100) μs, and at each of these times 30 data points are generated. The *a priori* optimised and fully adaptive Bayesian strategies are applied to simulated data with a total of 210 entries, which is the equivalent total of the other two methods. The

three Bayesian methods use Jeffreys prior seen in Equation 2.17, with the range between $\theta_{min} = 14.5$ μK and $\theta_{max} = 125$ μK. For these particular parameters, the *a priori* optimal expansion time is calculated to be $t_s = 14$ μs.

The variability on the temperature estimate for each method can be seen in Figure 6.1. It can be seen that the *a priori* and adaptively optimised methods result in estimates which are far more accurate than those without optimised release times. Alongside this, parts (a) to (c) show the convergence to the true temperature with respect to the number of data points, showing that the time optimised methods also converge quicker, requiring less data.

6.2 Experimental Realisation

6.2.1 The Experimental Setup

The Bayesian framework can now be applied to my experimental data. The key parts of the experiment are explained in Sections 4.2 and 5.1.3 regarding the K dark MOT and tweezer loading respectively. As a quick reminder, ^{41}K atoms are loaded into the optical tweezer from a dark MOT. The number loaded can be controlled by the amount of atoms loaded in the initial MOT stage. The atom number can be determined by using Equation 5.6. The tweezer beam has a wavelength of 790 nm and is focused down to a waist of ≈ 1.9 μm. The resulting elongated tweezer trap has a radial-to-axial dimension ratio of $1 : 249$. The setup can be well described by Equation 6.3.

As the temperature of the few-atom system is determined by the trap depth of the optical tweezer, I can perform a pseudo evaporative cooling stage to further reduce the temperature. Due to collisions between individual K atoms being negligible, this is not evaporative cooling in the traditional sense, as there is a lack of thermalising collisions. Firstly, as the trap depth is being lowered, the hottest of the atoms are removed from the trap. Secondly, as

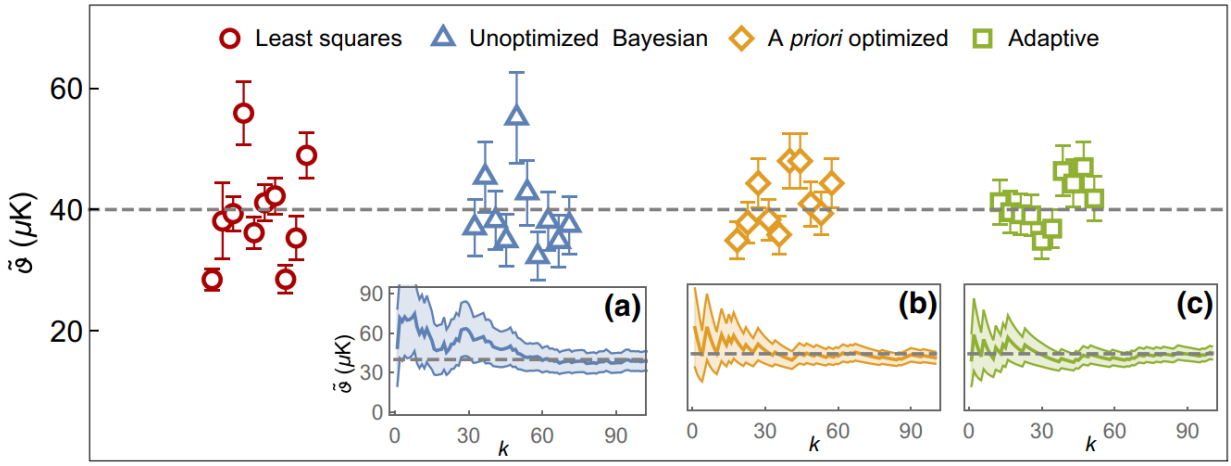

Figure 6.1: Reliability of estimation strategies for a trap loaded with a single atom. Temperature estimates and their error bars, obtained from processing simulated release-recapture measurements on a single ^{41}K atom with different protocols (see Section 6.1.3 for details). The results obtained from ten different realisations are shown. The underlying true temperature is set to 40 μK (dashed grey line). First, a record with 30 measurements at seven unoptimised expansion times is fitted to the recapture probability, as discussed in Section 6.1.1 (red circles), as well as processed with our Bayesian-global technique (blue triangles). The time-optimised methods are also applied to the same overall number of data points (i.e., 210), respectively simulated at the optimal *a priori* recapture time t_s (orange diamonds) and at adaptively chosen variable optimal times (green squares). Optimisation of the recapture times noticeably reduces the variability of the estimates. Note that there is no abscissa axis in the main plot; the estimates have been squeezed together to help visualise their variability. Insets (a)–(c) show the typical convergence of global estimates with the number of measurements k. As shown, time-optimised methods typically require much less data to converge, when compared with their unoptimised counterparts. Also, the final error bars are smaller in (b) and (c).

the potential energy is being adiabatically lowered, the total energy is reduced. This could be considered closer to a distillation technique.

6.2.2 Multi Atom Model

Even though it's possible to control the number of atoms within the tweezer, the assumption that only a single atom be loaded every experimental run is ambitious in some cases. To account for more atoms, we can modify the measurement model $p(n_i|T, t_i)$ from Equation 6.1. We can assume the atoms are distinguishable, with negligible interactions between them. Following this, the probability for recapturing n_i atoms during the ith run, given that the trap is initially loaded with N_0 atoms, can be written as

$$p(n_i|N_0, T, t_i) = B[n_i|N_0, f(T, t_i)], \tag{6.6}$$

where $B(n_i|N_0, q)$ is the binomial distribution

$$B(n_i|N_0, q) = \binom{N_0}{n_i} q^{n_i}(1-q)^{N_0-n_i}, \tag{6.7}$$

with success probability $q = f(T, t_i)$, as defined in Equation 6.3. Here N_0 is known as a nuisance parameter and thus needs to be marginalised over. In order to do this, we begin with the fact that the probability of starting with N_0 atoms can be described by a Poisson distribution [126, 127]

$$P(N_0|\lambda) = \frac{\lambda^{N_0}}{N_0!} e^{-\lambda}, \tag{6.8}$$

where λ is the mean initial atom number. We can find this value experimentally by taking a large set of calibration points at zero release time. In this case

$$p(n_i|T, t_i) = \sum_{N_0=0}^{\infty} P(N_0|\lambda) B[n_i|N_0, f(T, t_i)] = P[n_i|\lambda f(T, t_i)]. \tag{6.9}$$

The model for the multi-atom scenario is thus a Poisson distribution with a mean of $\lambda f(T, t_i)$. Using this, we can now apply the Bayesian methods from Section 6.1.2 to our experimental data.

6.3 Results and Discussion

6.3.1 Processing Real Data at Unoptimised Release Times

I will first look into the analysis of our experimental data at unoptimised release times, where we apply least squares fitting and the unoptimised Bayesian technique to the data. In this case, the data is from two sets of measurements on the ^{41}K atoms, one in a shallow trap, the other in a deep trap. The depths of which are $U_0/k_B = 110$ μK and 290 μK respectively. For the shallow potential, we took 50 measurements on the number of recaptured atoms at each of the expansion times $\mathbf{t}_a = (5,\ 10,\ 15,\ 20,\ 30,\ 40,\ 50)$ μs, with an additional 100 calibration measurements with zero release time. For the deep potential we took 30 measurements at each of the expansion times $\mathbf{t}_a = (5,\ 10,\ 20,\ 30,\ 50,\ 70,\ 100)$ μs, with an additional 60 calibration measurements with zero release time.

We now process the data using the nonlinear fit to the mean number of recaptured atoms, including the $t = 0$ times with the rest of the data. We receive temperature estimates of 15.8 $\pm$ 32 μK and 57 $\pm$ 11 μK for the shallow and deep trapping configurations, respectively. The fits can be seen as the solid red lines in Figure 6.2.

The unoptimised Bayesian methods that were developed are then applied to the exact same data. Using the zero release time calibration measurements, we find the mean atom numbers to be $\lambda = 1.88$ and $\lambda = 1.65$ for the shallow and the deep traps, respectively. Using the reasoning in Section 6.1.2, the support of our prior $p(\theta)$ is set to $5.5 \leq \theta \leq 30$ μK for the shallow trap and $14.5 \leq \theta \leq 125$ μK for the deep trap. The Bayesian estimates come out to be 15 $\pm$ 17 μK and 45 $\pm$ 7 μK, these are represented by the dashed blue lines in Figure 6.2.

At first glance, the estimates from both of the methods seem similar. But we can see that the temperature estimate using the Bayesian method for the deep trap falls below the error bars of the least squares method. One could expect some discrepancy due to the smaller

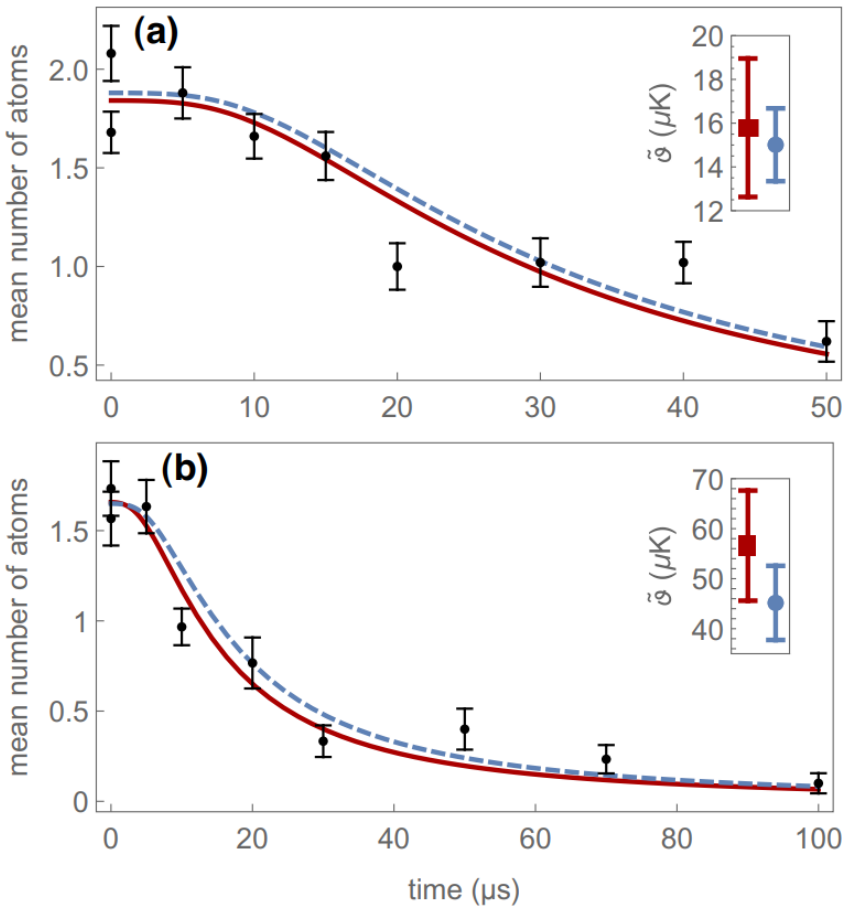

Figure 6.2: Temperature estimation from measurements at unoptimised recapture times. Empirical mean and standard error of the number of recaptured ^{41}K atoms (black dots) at each free expansion time in the two experiments described in Section 6.3.1 for a (a) shallow and (b) deep trapping potential. The solid red curves are two-parameter nonlinear fits to $\lambda f(T,t)$ in λ and T, where $f(T,t)$ is the survival probability from Equation 6.3. These yield (a) $T_a = 15.8 \pm 32$ μK and $\lambda_a = 1.84 \pm 11$ and (b) $T_b = 57 \pm 11$ μK and $\lambda_b = 1.66 \pm 9$. In turn, the Bayesian strategy (cf. Section 6.1.2.1) applied to the full measurement record gives (a) $T'_a = 15.0 \pm 17$ μK and (b) $T'_b = 45 \pm 7$ μK. The insets show the estimates. The dashed blue curves correspond to $\lambda f(t,T)$ evaluated at temperatures T'_a and T'_b, with initial average atom numbers $\lambda'_a = 1.88$ and $\lambda'_b = 1.65$, as calculated from the calibration measurements.

number of measurements performed in the deep trap experiment, but this is exactly what using the Bayesian techniques aims to solve.

6.3.2 Finding the Most Reliable Strategy

We see from the above analysis that both the nonlinear and Bayesian strategies yield different temperature estimates using the same data set. The next step is to establish which of the methods is more dependable and should be trusted. To figure this out, multiple runs of the deep trap experiment were simulated, setting the temperature to 40 μK. The key details can be seen in Figure 6.3.

We first examine the nonlinear and unoptimised Bayesian methods. In Figure 6.3 (b), the red circles and blue triangles represent ten simulated deep-trap experiments using these methods, respectively. Each point consists of 30 data points simulated at the seven release times in $\mathbf{t}_b$, with an additional 60 calibration measurements at $t = 0$, as before. It can be seen that the variability of the estimates is high, although the Bayesian estimates have a lower spread with more consistent error bars.

In order to quantify the variability, we can use the empirical error Var $\tilde{\vartheta}/\langle\tilde{\vartheta}\rangle^2$ of a set of estimates, where

$$\text{Var } \tilde{\vartheta} = \langle\tilde{\vartheta}^2\rangle - \langle\tilde{\vartheta}\rangle^2, \tag{6.10a}$$

$$\langle\tilde{\vartheta}\rangle = \frac{1}{N}\sum_{i}^{N}\tilde{\vartheta}_i. \tag{6.10b}$$

For these parameters over 100 simulated runs, the variability of the conventional least squares method was evaluated as 0.064. The unoptimised Bayesian method was evaluated as 0.057, which is slightly more reliable.

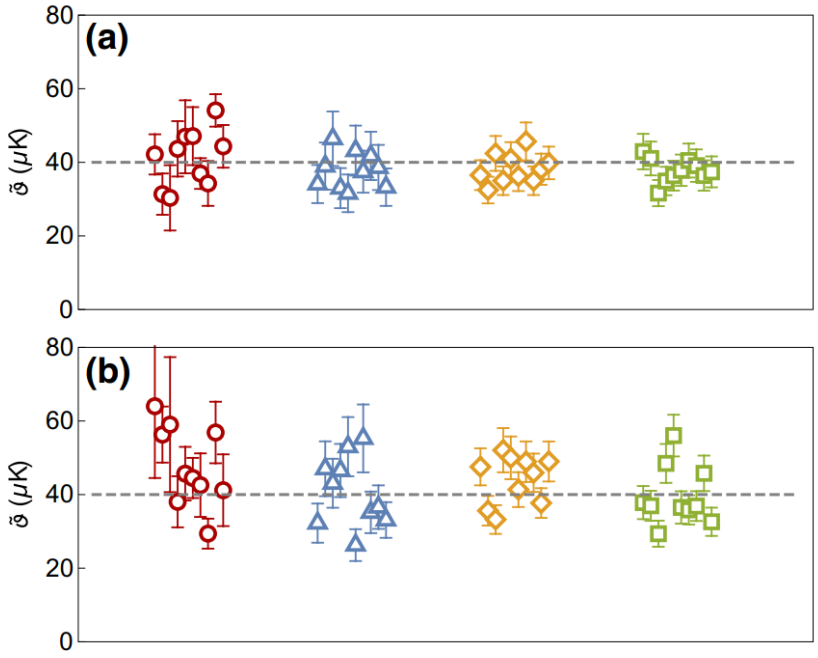

Figure 6.3: Estimate variability of different strategies. Temperature estimates drawn from simulated release-recapture measurements on ^{41}K. The parameters for the simulations are those of the deep-trap experiment from Section 6.3.1 and Figure 6.2 (b), and the true temperature is set to 40 μK (dashed gray). In (a), the mean number of atoms loaded into the trap is assumed to be known, and equal to $\lambda = 1.65$. In each case, ten independent runs of the experiment are simulated, consisting of 30 measurements generated at each of the seven unoptimised recapture times $\mathbf{t}_b$. The estimates are calculated via the conventional least-squares method (red circles) and the Bayesian approach (blue triangles). Since λ is known, the least-squares method becomes a one parameter fit. Orange diamonds and green squares correspond to estimates drawn from the *a priori* optimised and fully adaptive protocols, respectively. These also run on datasets of 210 measurements. The *a priori* optimal recapture time here is $t_s = 22$ μs. In (b) λ is not known (its true value continues to be $\lambda = 1.65$). A calibration set of 60 measurements at $t = 0$ is thus needed, in addition to the 210 data points. In this case, the least-squares method becomes again a two-parameter fit in T and λ. For all three Bayesian variants, λ is recalculated at every run from a fresh calibration set. Hence, the λ used for estimation differs slightly between independent simulations. The overall variability of the estimates thus increases. This is particularly apparent for both the *a priori* optimised and adaptive protocols, as the optimisations are done with the estimated λ, resulting in slightly off optimal times. Markers in (b) are the same as in (a).

But, we now wish to look at the Bayesian methods where the release times are chosen to maximise information gain. Looking again at Figure 6.3 (b), we move onto the results for the *a priori* optimised and fully adaptive method (represented by the orange diamonds and

green squares, respectively). These use datasets of the same size as the unoptimised methods (i.e. 210 points and 60 calibration measurements). We wish to evaluate the information gain from Equation 2.21, in order to do this we must truncate the Poisson distribution (Equation 6.8) for the number of atoms initially loaded into the trap. Here, we set $N_0 = 7$ as the maximum, since the probability of loading more atoms is negligible for $\lambda = 1.65$, which is the true value of the initial number of atoms in the simulations. The value of λ is assumed to be unknown when processing data, thus needing to be recalculated at every simulated run from the calibration data. In order to account for the finite resolution of the experimental release times, we replace the optimal release times with integer multiples of a minimum resolution of 2 μs.

As expected from Figure 6.1, the fully adaptive method is the most dependable, outperforming the other methods, having a variability of 0.034 for 100 runs. This is a 40% improvement over the unoptimised Bayesian method, and over 50% improvement compared to the conventional least squares method. An interesting note is that the variability of the *a priori* optimised method is comparable to that of the fully adaptive one, yet it is far easier to implement. Even more so when taking experimental data, meaning it should be the default method. This is our first key result.

The fact that the initial average atom number in the tweezer is unknown interferes with the estimate variability. The empirical average of the simulated calibration data differs from run to run, even if we fix λ. In order to single out the temperature-estimation aspect of the calculations, we also run variability checks where we treat λ as a known parameter. It can be seen from Figure 6.3(a), that the overall variability is smaller in this case, but the hierarchy between the methods has not changed.

6.3.3 Assessing Convergence Speed

We have seen so far that using the *a priori* optimal release time obtained from the release-recapture data, then processing this using the global thermometry techniques, yields a clear advantage over the unoptimised methods, at least in terms of reliability. However, we also wish to optimise our experimental resources, such as time. We need to now consider the speed of convergence of the temperature estimate. We want to reduce the amount of data needed in order for the variability to settle into an asymptotic regime, and also find the rate at which the variability is reduced once we reach this limit.

In Figure 6.4 we compare the conventional non-linear-fit method to our *a priori* optimised Bayesian-global protocol in terms of convergence. We use the same parameters as in Section 6.3.1. We compute the estimated variability from Equations 6.10 for 5000 simulated runs of the experiment, and gradually increase the number of measurements per run k. As seen in the figure, as k grows, the variability of both protocols eventually scales as

$$\frac{\text{Var } \tilde{\vartheta}}{\langle \tilde{\vartheta} \rangle^2} \sim \frac{1}{kF}, \tag{6.11}$$

where F is the free parameter. To get a rough idea of the onset of this scaling, we take the logarithm of the calculated variabilities and fit it to $-a \log k - \log F$. We start from the largest k and work backwards, adding points at lower k to the fit. We then search for the number of shots at which the exponent a first deviates from 1 by more than 2.5%. This gives $k_c \simeq 350$ for the conventional method and $k_{ap} \simeq 200$ for our *a priori* optimised protocol. Hence, for $k > k_c$, we can be certain that both protocols have entered the asymptotic regime in k. Comparing the two, we find that the *a priori* optimised method has a 43% variability reduction compared to the conventional method in release-recapture measurements, even in the asymptotic limit. From this, we have shown that our methods are not only more reliable when processing small data sets, but that they also require fewer measurements to achieve

the same precision as the conventional protocol. For our experimental setup, this roughly translates into halving the number of measurements needed to hit any target precision. This is the second key result of this work.

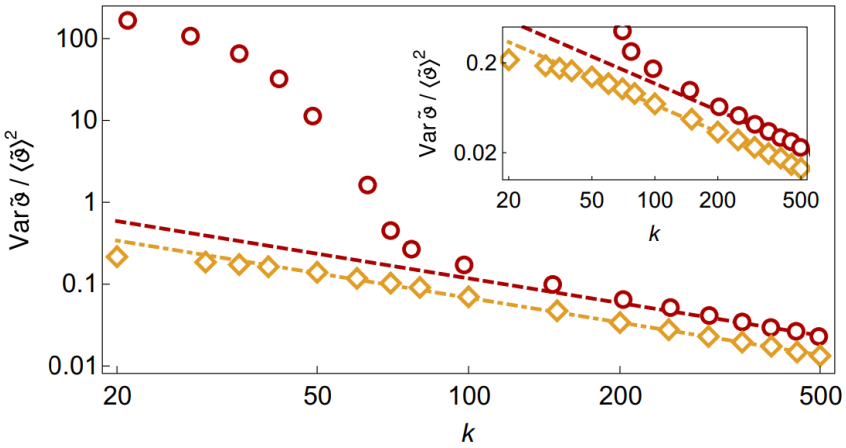

Figure 6.4: Convergence of conventional and *a priori* optimised protocols. Log-log plot of variability versus the number of measurements k, calculated from 5000 simulated runs of the deep-trap experiment from Section 6.3.1. The measurement count k excludes any calibration measurements at $t = 0$. Specifically, $(2/7)$ k calibration outcomes are generated for each run. All other parameters are the same as in Figure 6.3. The conventional non linear-fit release-recapture (red circles) is compared to our *a priori* optimised protocol (orange diamonds). Note the vast superiority of the optimised method for low k, i.e., scarce data. Asymptotically, the variability takes the approximate form $1/(kF)$. This occurs for $k > 350$ for the conventional protocol and $k > 200$ for the optimised one. The dashed and dash-dot lines highlight the asymptotic variability scaling for both methods. The offset between these lines indicates that the asymptotic convergence speed to the true temperature is roughly twice as fast for the *a priori* optimised protocol. The insets enlarge the region in which our Bayesian technique enters the asymptotic regime.

6.3.4 Time Optimisation on an Individual Experiment

We can now explore the scenario where the *a priori* optimised protocol is used in an actual release-recapture experiment (see Figure 6.5). To see what this might look like, we use the data from the shallow trap experiment, which was processed in Figure 6.2(a). As before, we limit the initial number of atoms in the trap to $N_0 = 7$, which gives us an optimal capture time of $t_s = 42$ μs. We then use our Bayesian global technique to process the measurement outcomes at the times closest to t_s. These are the 50 measurements taken at 40 μs. Normally, every single data point would be taken at the exact same optimal time, but due to running out of data points, we had to move onto the next closest time, which was 50 μs, and so on.

The estimate and error bars resulting from the Bayesian record of the first k entries of the reordered record are plotted in orange in Figure 6.5. From this, we observe that more than 100 data points seem to add little to no information about the estimate, these points did not need to be taken. This shows that when we uniformly sample the decay of the survival probability, more than 30% of our experimental resources are wasted. To further emphasise the importance of the time optimisation to the convergence of the estimate, we display a plot (in blue) in which the measurements were processed in reverse, from least to most informative.

From this, we can display three key benefits of optimising the release time to increase information gain. Firstly, it produces more reliable estimates when lacking data. Secondly, it ensures a faster convergence towards the true temperature in the asymptotic limit of many measurements. Finally, it allows us to significantly reduce the number of data points needed for the estimate to converge in a single experimental run.

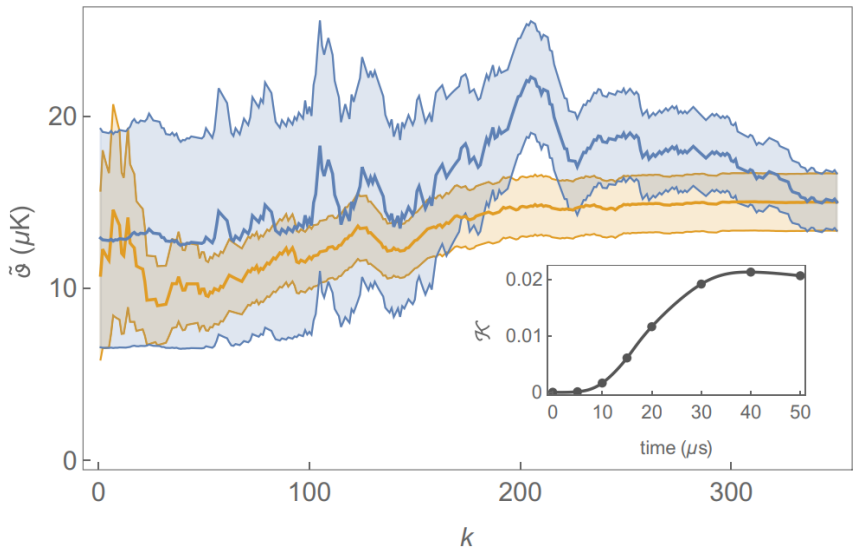

Figure 6.5: Recapture-time optimisation. Estimate and error bar from the first k entries of the measurement record of the shallow trap experiment from Figure 6.2(a), reordered to mimic the *a priori* optimised protocol (orange). The optimal recapture time $t_s = 42$ μs is calculated as per Section 6.1.2.2. The *a priori* information gain $\mathcal{K}$ as a function of the recapture time is shown in the inset for this model (gray dots). The gray line is a mere guide to the eye. The 50 measurements at the closest recorded time (40 μs) are moved to the top of the list. The set of measurements at the second-closest recorded time (50 μs) are picked next, and so forth, until exhausting the 350 available data. The estimate and error bars of that exact same list, but processed in the reverse order, are shown in blue for comparison. As we can see, the orange curve already converges to the final estimate by processing the 200 most informative data. At that point, the estimate is 14.7 ± 1.7 μK. The remaining 150 data carry practically no information, since the estimate drawn from the full measurement record is 15 ± 1.7 μK.

6.3.5 *a priori* Optimised Protocol versus Fully Adaptive Protocol

As seen in Section 6.3.2 the *a priori* optimised and fully adaptive protocols have an almost identical estimate variability. This prompted us to focus more on working with the former,

due to its simplicity. Although, in some situations, it may be worth the extra effort to implement the fully adaptive method for the release time. In order to see this, we go back to the deep-trap configuration in Figure 6.2 (b), to compare the two protocols again. Just like in Section 6.3.2, we simulate ten independent experiments for each method, but in this case, we work with a wider support for our prior, moving it by one order of magnitude down into colder temperatures. Which is to say, $1.45 \leq \theta \leq 125$ μK.

As seen in Figure 6.6, the adaptive protocol exhibits a reduced variability with respect to the *a priori* optimised method. This is due to the fact that the *a priori* optimised time is close to 60 μs, while the true optimal release time stabilises around 20 μs after a few measurements. This quickly renders the *a priori* optimised method inefficient when it comes to information acquisition. The fully adaptive method does not share this issue.

6.4 Conclusions

Within this work, we have demonstrated how temperature methods can be substantially improved in practice by exploiting Bayesian global thermometry techniques. We do so by utilising our flexible experimental setup, taking release-recapture measurements on a few ^{41}K atoms at μK temperatures which are tightly confined in an optical tweezer. The conventional protocol samples the fraction of recaptured atoms evenly across recapture times and fits the data to a model of recapture probability. Instead, what is proposed here is that we choose the release time that maximises the information gain, then processing the measured data with the developed Bayesian techniques.

Using both the experimental data we collected alongside the numerical simulations, we have shown that these new methods have three key advantages. Firstly, the variability of estimates extracted from small data sets is largely reduced when compared to the conventional least squares method, leading to more dependable thermometry. Secondly, finding an opti-

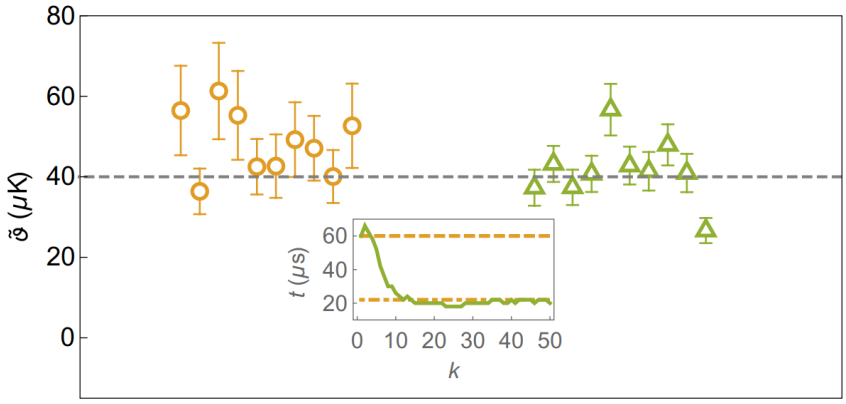

Figure 6.6: *a priori* optimised protocol versus adaptive protocol. Comparison between the *a priori* optimised (orange diamonds) and fully adaptive (green squares) protocols. Ten independent runs of the deep-trap experiment are simulated for each method. All parameters are the same as in Figure 6.10 (b), except for θ_{min}, which is set here to 0.5% of the trap depth U_0/k_B (see Section 6.3.5). The inset shows the optimal expansion time as a function of k for one of the simulated measurement records (solid green). The *a priori* optimal recapture time for this wider hypothesis support is indicated by the orange dashed line. In contrast, the *a priori* optimal time for the narrower support used in the previous figures is the orange dash-dot line. Our observation that the *a priori* optimised method seems to perform as well as the arguably superior fully adaptive scheme is explained by the fact that, for the narrower prior, t_s almost coincides with the true optimum for most of the experiment.

mal time leads to a faster convergence towards the true temperature in the asymptotic limit of many measurements. Finally, the optimisation of the recapture time greatly reduces the number of measurements we need to take for the estimates to stabilise to a final temperature reading. Alternatively, you can view the conventional method as wasting resources by taking and processing numerous uninformative measurements. Time is an expensive resource when it comes to real experiments, especially when many temperature measurements are required.

We also demonstrate that the best results are obtained when using the fully adaptive

protocol, where each release time takes into account all of the previous measurements. Yet, even a simpler protocol, the *a priori* optimal one, can compete with the fully adaptive method. Here you measure repeatedly at a single release time, the one that maximises the information gain in the first measurement. This time follows from the parameters of the experiment and the range of temperatures being probed. Other than an arbitrarily broad temperature range, we assumed no prior knowledge about the temperature.

We have shown how quantum thermometry can deliver practical solutions leading to quantifiable precision enhancements, once the quantum Fisher information-based local paradigm is abandoned in favour of the global framework. While the former has proven useful when studying fundamental precision limits and maximising the responsiveness of temperature sensors, the more general Bayesian framework can, in addition to that, process finite experimental records optimally. Importantly, all of these fundamental principles can be applied to other techniques in different temperature ranges and completely different experiments, leading to an exciting future for quantum thermometry.

Chapter 7

Controlling the Interactions in a Cold Atom Quantum Impurity System

This chapter is a reformatted, slightly adapted copy of my paper seen in [41]. It describes a cold atom quantum impurity system consisting of a single K atom trapped in an optical tweezer, which is immersed in an ultracold bath of Rb atoms. We then explore their interactions by performing Feshbach spectroscopy, also detecting several interdimensional confinement-induced resonances. We also study how these resonances change, as the temperature of the bath and the dimensionality of the system are altered.

- **Section 7.1** describes the base setup for our quantum impurity system, which consists of a single K atom, trapped within an optical tweezer, immersed in an ultracold bath of Rb atoms. I also display the full experimental sequence from the individual atomic species to when they interact.
- **Section 7.2** looks at how an external magnetic field affects the interactions in the system, and how the unique dimensionality of the system affects them. I discuss the appearance of confinement induced resonances in the experimental data and how they

affect the expected Feshbach resonances.

- **Section 7.3** explores how the wavelength of the SST affects the interactions of the system. I discuss the experimental measurements I took, which monitor the thermalisation and lifetime of the impurity for different wavelengths.

- **Section 7.4** displays the conclusions drawn.

7.1 K Quantum Impurity in a Rb Thermal Bath

Our experimental architecture is sketched in Figure 7.1: a single atom of ^{41}K is trapped in a species-selective tweezer (SST) and is immersed in a cloud of ^{87}Rb at ultracold temperatures. The wavelength of the laser that produces the SST is tuned close to the tune-out wavelength for Rb [67, 128], $\lambda_0 \simeq 790$ nm. An external magnetic field is used to control the interspecies interaction strength. This configuration realizes a pristine implementation of a quantum impurity system, because at ultralow temperatures, the motion of the tightly trapped K atom is confined to a few modes of a three-dimensional quantum harmonic oscillator.

Our experimental sequence (seen in Figure 7.2) starts by loading Rb atoms from a dark magneto-optical trap (MOT) into a crossed dipole trap [70]. The atoms are initially pumped in the $|F = 1\rangle$ ground state manifold. We then perform evaporative cooling keeping the magnetic quadrupole field on, so that at the end of the evaporation we obtain a polarized sample in the $|F = 1, m_F = 1\rangle$ state, by treating the ultracold sample similarly to a spin-1 spinor condensate [129–131]. This process is carried out using a Stern Gerlach procedure with a pulse of 10 ms, images of which can be seen in Figure 7.3. This is a magnetic field gradient which increases the trap depth for atoms in the $m_F = +1$ state, lowering the depth for the $m_F = -1$ state. Meaning the two unwanted states are selectively evaporated [132]. Unfortunately, this means about one third of the atoms are lost. A typical evaporation ramp lasts 4.25 s, and we obtain pure Bose-Einstein condensates of 6×10^4 atoms. Unless otherwise

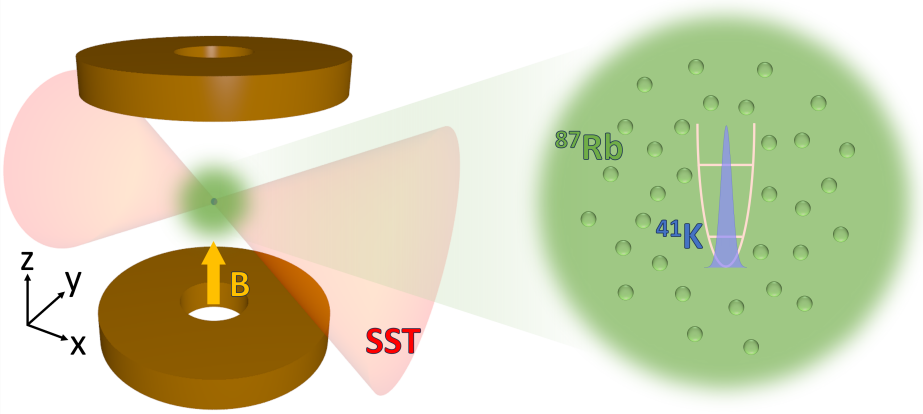

Figure 7.1: Representation of our experimental architecture (not to scale): a single ^{41}K atom is trapped in a species-selective optical tweezer (SST) and immersed in a cloud of ultracold ^{87}Rb atoms trapped in an optical dipole trap (not shown). Because of the tight confinement, in the ultracold regime the motion of the K atom is limited to a few quantized modes. A uniform magnetic field is applied along the vertical axis to control the value of the interspecies scattering length. By adjusting the wavelength of the SST around λ_0, we can make the tweezer attractive, transparent, or repulsive for the Rb atoms, allowing us to locally control the Rb density in the vicinity of the K atom.

stated, for this work, we stop the evaporation after 2.25 s obtaining thermal gases of 10^5 atoms at $\simeq 1$ μK, with trapping frequencies $\omega^{(Rb)} = 2\pi\times$ (85, 255, 265) Hz.

At the end of the ramp, we switch on a K MOT that surrounds the Rb sample for 200 ms. We also switch the SST on at the same time. The latter is realized with an apoplanar microscope objective that produces a beam with $\simeq 2.1$ μm waist at a distance of 25.5 mm. The SST light is linearly polarized along the vertical direction. The SST is initially placed 40 μm above the Rb cloud to avoid losses due to KRb scattering during the loading of the K atoms. The trapping potential has a typical depth of 1.2 mK. After the MOT, we compress the K cloud with a dark MOT, allowing us to load $\simeq 4$ atoms of K in the SST with temperatures of 30 μK. We then switch off the quadrupole field, and we ramp on a uniform magnetic field of 10 G along the vertical direction. Once the field is set, we optically pump the

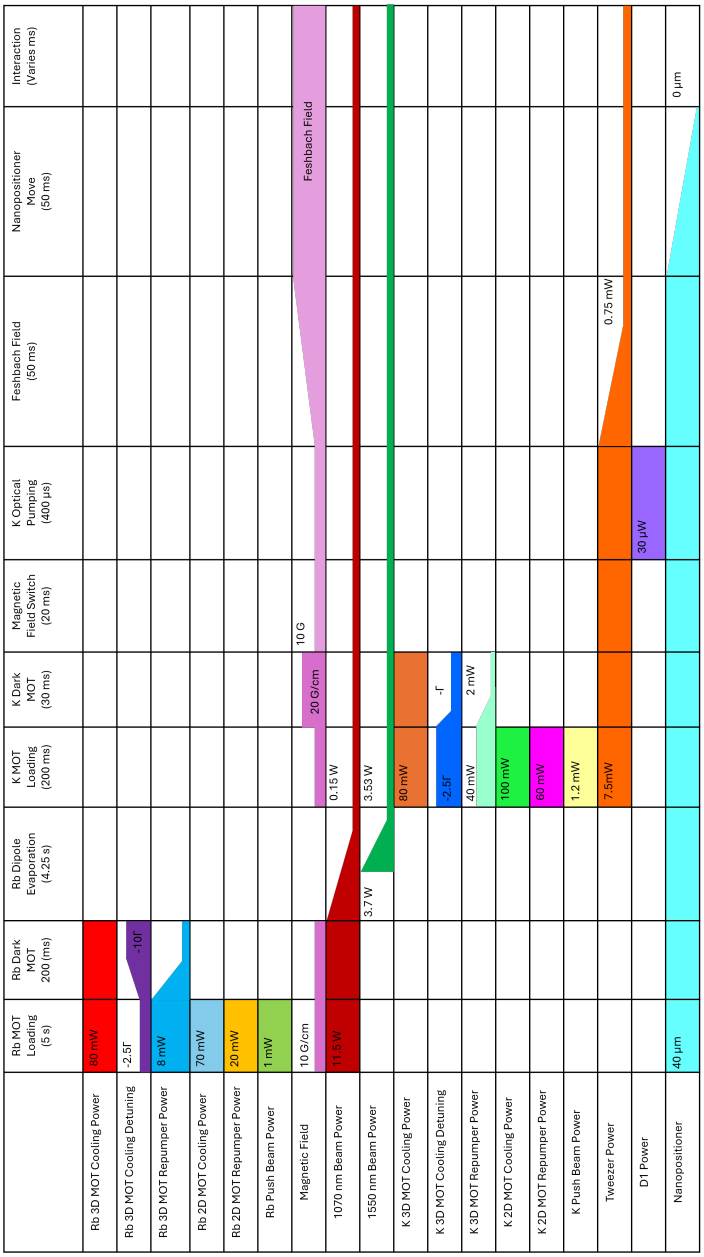

Figure 7.2: Experimental sequence used to interact a single atom of K with an ultracold bath of Rb. I exclude the steps for absorption and fluorescence imaging.

K atoms in the $|F = 1, m_F = 1\rangle$ state with two laser beams tuned on the D1 line. The beams include a π polarized beam resonant with the $|2S_{1/2}, F = 2\rangle \rightarrow |2P_{1/2}, F = 2\rangle$ transition and a σ^+ polarized beam resonant with the $|2S_{1/2}, F = 1\rangle \rightarrow |2P_{1/2}, F = 1\rangle$ transition. After this stage, both species are therefore in the target $|F = 1, m_F = 1\rangle$ ground state. Finally, we ramp the magnetic field to the target value in 50 ms, lowering at the same time the power

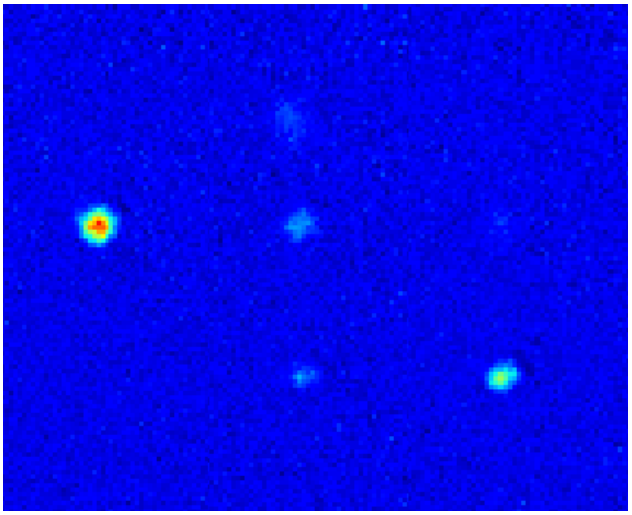

Figure 7.3: The polarisation of the ultracold Rb cloud into the $|F = 1, m_f = 1\rangle$ state. This is a collated absorption image of the three different stages. On the left you have the unpolarised atom cloud, in the centre you have the three different magnetic substates split spatially using a Stern Gerlach field which applies a force on the atoms depending on their substate, on the right we have the correctly polarised sample.

of the SST. This allows us to keep only the coldest atoms in the SST and to reduce the off-resonant light scattering that could cause losses for both species. Typically, we end up with 1.5 atoms of K at $\simeq 20$ μK, with trapping frequencies $\omega^{(K)} = 2\pi \times (1.4, 22, 22)$ kHz.

To immerse the K atoms in the Rb bath, we actuate a mechanical nanpositioner stage that brings the SST to the centre of the Rb cloud in 50 ms. After a variable interaction time, the Rb atoms are released, and we perform time of flight absorption imaging. The K atoms are instead kept in the SST and their number is inferred through fluorescence imaging, typically needing 30 repetitions. As mentioned before, in order to avoid undesired light shifts caused by the SST, we chop the fluorescence and tweezer light at a frequency of 1.02 MHz and a phase shift of 90° [116]. To measure the temperature of the K atoms, we perform release-recapture thermometry using Bayesian estimation, requiring 180 experimental runs [71].

The tune-out wavelength λ_0 for ^{87}Rb is approximately 790 nm [128] in case of linearly

polarized light. In our case, however, the strong focussing of the tweezer beam could in principle generate longitudinal field components at the position where the K atoms are trapped. This would result in a shift of the tune-out wavelength. Therefore, to find where the SST is transparent for the Rb atoms, we measure the survival probability of the K atoms as a function of the SST wavelength. This scan can be seen in Figure 7.4. Indeed, across λ_0 the potential for Rb goes quite steeply from attractive to repulsive, respectively increasing or decreasing the local Rb density. By scanning the SST wavelength, we observe that the survival probability of K atoms at 10 G after 50 ms goes from 0 to 1 in the [790-790.1] nm range. This sets our range of operations, as it allows us to fully open or close the SST volume to the Rb atoms. We will show in Section 7.3 how to use this feature to control the way the quantum impurity interacts with the bath. We calculate that at 0.1 nm detuning from λ_0 the density of Rb in the SST volume is vanishing, therefore we infer that for our system λ_0 is not significantly shifted from the expected value of $\simeq 790$ nm.

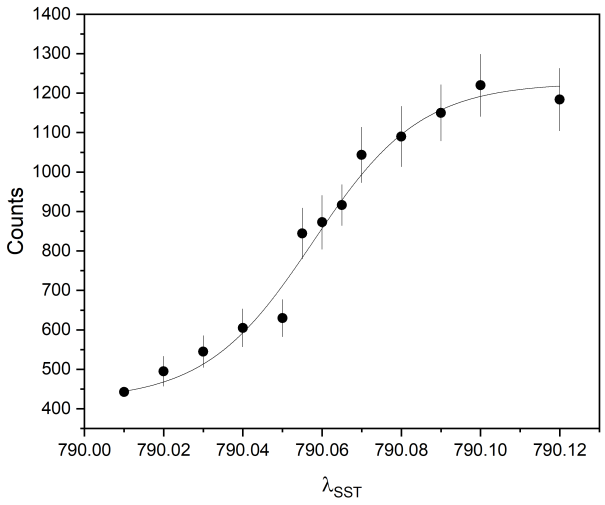

Figure 7.4: Reported are the counts on the CMOS camera imaging the K atoms as a function of λ_{SST}. The error bars are the result of the average over 30 experimental repetitions. The number of counts is proportional to the number of K atoms. Approximately 450 counts correspond to 0 trapped atoms. The line is a sigmoid fit to the data.

7.2 Controlling the interactions with the external magnetic field

We now follow on from, and expand upon, the theory concerning confinement induced resonances set out in Section 2.2.1.

To accurately determine the effective scattering length $a_{eff}^{(m)}$ as a function of the external magnetic field and the resonance positions in our system, we utilise the theory developed in [83] with our experimental parameters. The regularised wave function of two particles at the same position projected to the mth partial wave $\chi_m(\rho)$ obeys the following integral equation derived from the Schrödinger equation:

$$\frac{1}{\tilde{a}(\hat{E}_c)}\chi_m(\rho) = \frac{\rho^m e^{-\rho^2/2l_{yz}^2}}{(2m+1)!\ \pi l_{yz}^2} + \frac{2\pi}{\mu_{KRb}}\int d^2\boldsymbol{\rho}' \mathcal{G}_m(\rho;\rho')\chi_m(\rho'). \tag{7.1}$$

Here $l_{yz} = \sqrt{\hbar/m_K\omega_{yz}^{(K)}}$ is the transverse harmonic oscillator length, $\mu_{KRb} = m_K m_{Rb}/(m_K + m_{Rb})$ is the reduced mass, $\mathcal{G}_m(\rho;\rho')$ is the regular part of the Green's function at zero collision energy [83], and $\tilde{a}(E)^{-1} = a_{3D}^{-1} - \mu_{KRb}\, r_{3D} E/\hbar^2$ is the energy-dependent scattering length [133, 134], with a_{3D} and r_{3D} the scattering length and the effective range in free space, respectively, and $\hat{E}_c$ the collision energy operator provided by

$$\hat{E}_c = \hbar\omega_{yz}^{(K)} - \left[-\frac{\hbar^2\boldsymbol{\nabla}_{\boldsymbol{\rho}}^2}{2(m_K+m_{Rb})} + \frac{m_K}{2}\omega_{yz}^{(K)2}\boldsymbol{\rho}^2\right]. \tag{7.2}$$

Once $\chi_m(\rho)$ is numerically obtained, the effective scattering length defined with the scattering amplitude being $\lim_{k\to 0} f_m(k) \propto -a_{eff}^{(m)}k^{2m}$ follows from

$$a_{eff}^{(m)} = \sqrt{\frac{m_{Rb}}{\mu_{KRb}}}\int d^2\boldsymbol{\rho}'\rho'^m e^{-\rho'^2/2l_{yz}^2}\chi_m(\rho'). \tag{7.3}$$

The resulting $a_{eff}^{(m)}/l_{yz}^{2m+1}$ is shown in Figure 7.7 for $m = 0$ and $m = 1$ by utilising the free-space scattering length as a function of the external magnetic field from [77] and the free-space effective range fixed at 168.37 a_0 from [81]. We note that it is necessary to include the effective range correction for quantitative predictions. Confinement-induced resonances appear when the effective scattering length diverges, whose positions are also indicated by the vertical lines in Figure 7.5 (a).

To detect the interdimensional Feshbach resonances, we look at the survival population of the K atoms as a function of the external magnetic field. As described earlier, we first set the magnetic field to the target value, and we then immerse the K atom in the Rb cloud, keeping the magnetic field constant. After a fixed interaction time, we detect how many K atoms are left. Given that on average we trap $\simeq 1$ atom of K, we expect three-body losses only through the KRbRb channel. This is verified by the exponential decay of N_K as a function of the interaction time (see also in the next section). Our results for a Rb cloud at 1 μK, $\lambda_{SST} = 790.025$ nm, and interaction time 50 ms are shown in Figure 7.5 (a). This set of parameters implies 1D-3D mixed dimensional scattering, since $k_B T/\hbar$ is lower than the radial trapping frequencies but significantly higher than the axial one. Our data show several loss features between 20 and 45 G, as expected in this scattering regime. To quantitatively analyse the data, we perform Gaussian fits of those features whose amplitude is above the experimental error bars, i.e., when the signal-to-noise ratio is above 1, and that are broader than twice our scan resolution, which is 0.25 G (see Figure 7.6). We identify 8 features, whose fitted centres are reported in Figure 7.5 (b) together with the values predicted by the theory, grouped according to the m and n indices. The widths of the resonances obtained with the Gaussian fits are reported as 'error bars'. The spacing of the observed loss features clearly mirrors the one of the theoretical values and, in particular, the presence of two series corresponding to $m = 0$ and $m = 1$ is apparent.

For what concerns the position of the resonances, the agreement between theory and

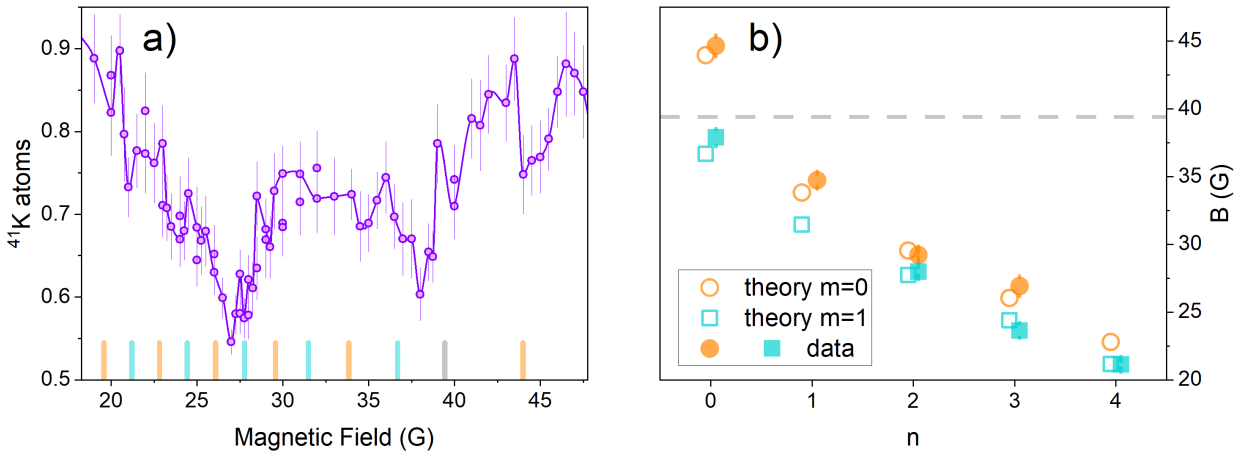

Figure 7.5: a) Feshbach spectroscopy for our quantum impurity system in the 1D-3D regime (1 μK): number of remaining K atoms as a function of the external magnetic field after 50 ms of interaction. For each value of the magnetic field, we average over 30 experimental repetitions. The error bars are the standard deviation of the mean. The solid purple line is a spline curve to guide the eye. The vertical grey line is the position of the free-space resonance according to [77]. The vertical orange (cyan) lines are the positions of the $m = 0$ ($m = 1$) resonances predicted by the theory. b) The open symbols are the values of the magnetic fields for the $m = 0$ (circles) and $m = 1$ (squares) interdimensional Feshbach resonances predicted by the theory, as a function of the order integer n in Equation 2.10. The filled symbols are the magnetic field values of the centres of the loss features in (a) obtained with a Gaussian fit. Data and theory are offset along the horizontal axis to enhance readability. We append the widths of the resonances obtained with the fit as 'error bars'. We assign each experimental resonance to the closest theoretical one. The dashed line is the position of the 3D resonance.

experiment is very good. However, we were not able to detect loss features in correspondence to the $\{m = 1, n = 1\}$ and $\{m = 0, n = 4\}$ resonances. The strength of the resonances, which is responsible for the width and depth of the loss features, is expected to decrease as m and n increase. However, as also reported in other systems [81, 135, 136], our data do not show the expected behaviour. The positions of three-body loss features are affected by

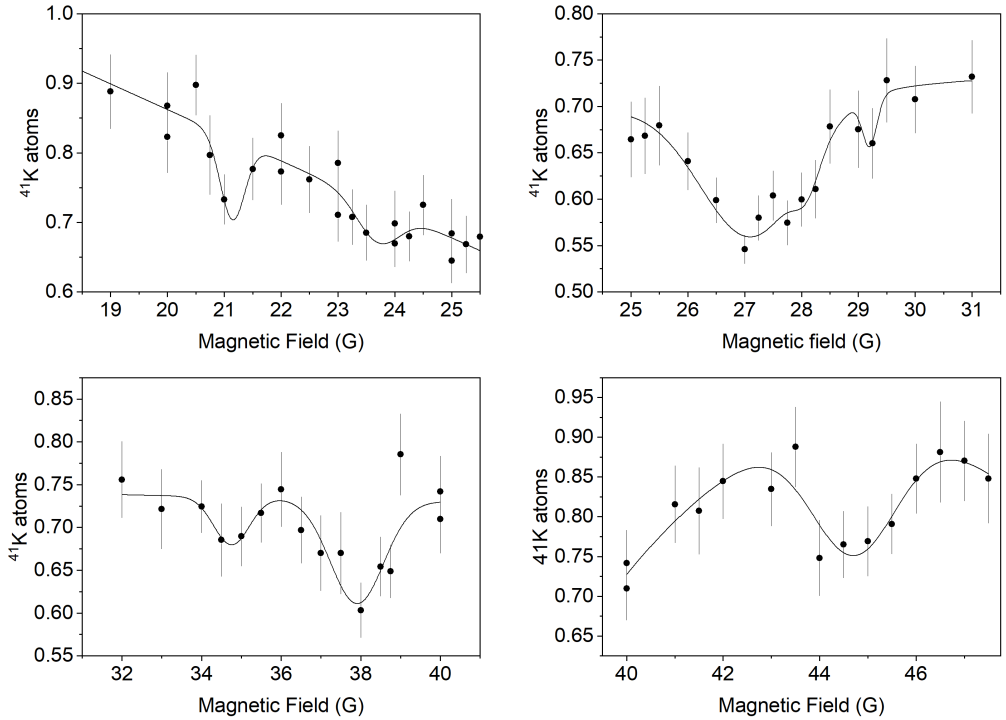

Figure 7.6: The data points are the result of Feshbach spectroscopy in the 1D-3D regime (1 μK). Reported is the number of remaining K atoms as a function of the external magnetic field after 50 ms of interaction. For each value of the magnetic field, we average over 30 experimental repetitions. The error bars are the standard deviation of the mean. The data are the same as in Figure 7.5 (a), broken down in four panels to enhance readability. The lines are fits to the data employing Gaussian functions.

complicated dynamics between atoms and molecules. The centre, width and the shape of the experimental curves can change with temperature, be affected by other close resonances, or by the presence of Efimov resonances. A description of these processes is outside the scope of this work. Another effect that could limit the resolution of our Feshbach spectroscopy is the fact that during the immersion, the K atom experiences a different elastic collision rate for different values of the magnetic field. This implies that the thermalisation time with the bath is not uniform across the magnetic field scan, and in some cases the thermalisation time could even be longer than the lifetime of the K atom. This effect could be mitigated by first immersing the K atom at a value of the magnetic field that enables thermalisation,

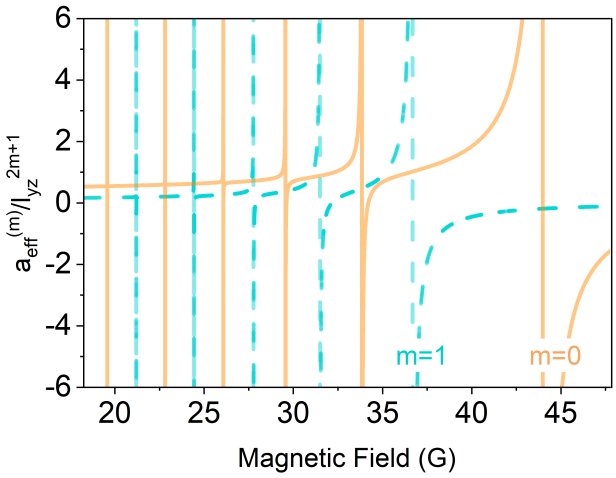

Figure 7.7: Theoretical predictions for the effective scattering 'length' in units of l_{yz}^{2m+1} as a function of the external magnetic field for a 1D-3D system with our experimental parameters. The solid orange line corresponds to the s-wave scattering length ($m = 0$), the dashed cyan line to the p-wave scattering volume ($m = 1$).

and then sweeping the magnetic field.

We found that the agreement with the theoretical predictions is good if we utilise the free-space scattering length calculated in [77]. There is worse agreement if we instead utilise the free-space scattering length inferred in [137]. Since there are many features in our system that are significantly narrower than in the free-space case, our measurements suggest that the position of the free-space resonance is closer to the one indicated in [77]. Remarkably, we can clearly identify both s-wave (orange lines in Figure 7.5 (a), points in Figure 7.5 (b)) and p-wave (cyan lines and points) resonances induced by the s-wave interaction.

By lowering the temperature of the bath until $k_B T/\hbar \leq \min\{\omega^{(K)}\} = \omega_x^{(K)}$, we can bring the K atom close to its quantum ground state, and collisionally freeze all degrees of freedom. This is of particular interest for the implementation of several quantum information protocols. In this configuration, the scattering between the quantum impurity and the bath is in the 0D-3D regime. The anisotropy of the tweezer confinement is reflected in the scattering,

so that resonances are approximately expected to appear when

$$\begin{aligned}
&(1+|m|+2n)\sqrt{\frac{m_K}{m_K+m_{Rb}}}\hbar\omega_{yz}^{(K)} \\
&+\left(\frac{1}{2}+n_x\right)\sqrt{\frac{m_K}{m_K+m_{Rb}}}\hbar\omega_x^{(K)}-|E_b| \\
&=\hbar\omega_{yz}^{(K)}+\frac{\hbar\omega_x^{(K)}}{2}
\end{aligned} \tag{7.4}$$

with an integer $n_x \geq 0$ labelling the new series of resonances caused by the confinement along the weak x axis. These n_x series are in addition to the resonances discussed in the 1D-3D case, that are still present. It is apparent from Equation 7.4 that the spacing and therefore the width and strength of the new series of resonances is approximately a factor $\omega_x^{(K)}/\omega_{xy}^{(K)}$ smaller than for the 1D-3D resonances. Our experimental results for a Rb bath at 100 nK with trapping frequencies $\omega^{(Rb)} = 2\pi \times (42, 157, 142)$ Hz, $\lambda_{SST} = 790.035$ nm, and interaction time 150 ms are shown in Figure 7.8 (a). This value of λ_{SST} generates a more repulsive potential for Rb than the one used for the 1D-3D scan. This is to compensate for the higher density of the Rb cloud at lower temperatures, which generates higher collision rates. We observe that, as expected, the positions of the loss features are approximately unchanged. However, their shape is substantially different due to the additional n_x resonances. These are so narrow and finely spaced that their net effect is to broaden the larger resonances and skew them towards lower magnetic field values. We show this effect in Figure 7.8 (b), which is an enlargement of the grey shaded area of Figure 7.8 (a). Such finely spaced resonances make it extremely challenging to finely control the interactions in the 0D-3D regime using an external magnetic field.

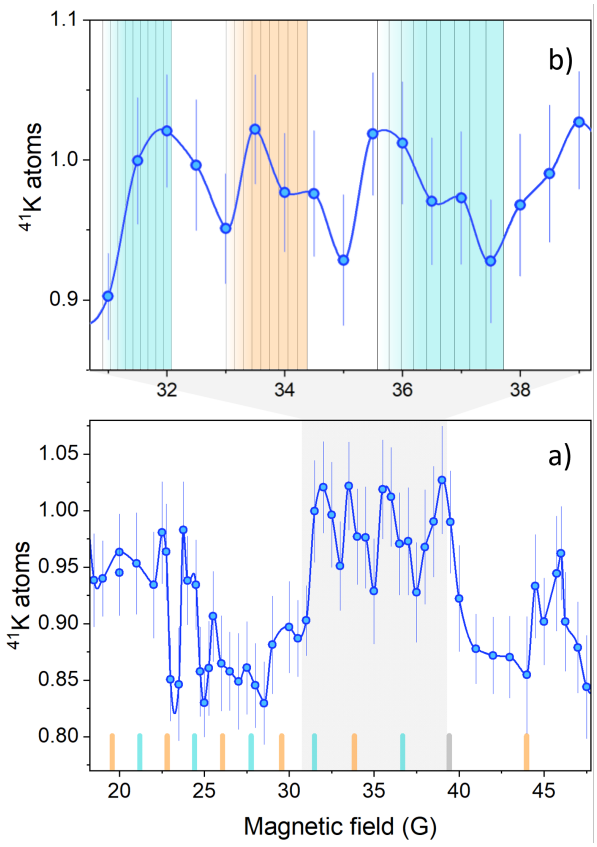

Figure 7.8: a) Feshbach spectroscopy for our quantum impurity system in the 0D-3D regime (100 nK): number of remaining K atoms as a function of the external magnetic field after 150 ms of interaction. For each data point, we average over 30 experimental repetitions. The error bars are the standard deviation of the mean. The solid blue line is a spline curve to guide the eye. The vertical grey line is the position of the free-space resonance according to [77]. The vertical orange (cyan) lines are the positions of the $m = 0$ ($m = 1$) resonances predicted by the theory. b) Zoom in the shaded grey area of (a). The vertical black lines are the positions of the resonances according to Equation (7.4) up to the tenth order. The shading indicates that the net effect is broadened resonances that are skewed towards the left, as observed in the experiment.

7.3 Controlling the Interactions with the Species-Selective Tweezer

The use of Feshbach resonances enables us to tune the scattering length between the quantum impurity and the atoms in the bath, even generating resonant p-wave scattering from the underlying s-wave collisions. It is however challenging to precisely tune the interactions, especially in the 0D-3D regime, because of the many close and narrow resonances. This in turn also implies that the 'zero-crossings' of the scattering length are very narrow, making it even more difficult to tune the interactions to zero. The ability to completely isolate the quantum impurity from the bath is particularly desirable, as it allows one to operate on the two subsystems independently. This is necessary, for example, if we wish to implement quantum engines, where quantum adiabatic transformations require decoupling the working fluid and the bath [2, 6]. As anticipated earlier, the use of the SST provides us with an additional tool to progressively screen the K atom from the atoms in the bath. As shown in Figure 7.9 (a) and Figure 7.9 (b), by changing the wavelength of the tweezer light across λ_0, one can tune the tweezer potential for the Rb atoms from attractive to transparent to repulsive. Specifically, the SST potential becomes attractive (repulsive) for Rb atoms below (above) the tune-out wavelength. The potential for the K atom is instead essentially unaffected in our range of operations, see Figure 7.9 (a). This means that with the SST wavelength, we can control the density of Rb atoms in the tweezer volume, and in turn control the scattering rate between Rb and K.

In Figure 7.9 (c) we show the number of remaining K atoms for a series of lower resolution scans of the magnetic field in the [20-35] G region, for different values of the SST wavelength. The more we tune the SST above λ_0, the higher the average number of K atoms remaining in the tweezer, signalling a lower overall interaction strength. We observe that when changing the wavelength, the position of the features is essentially unchanged, confirming that the

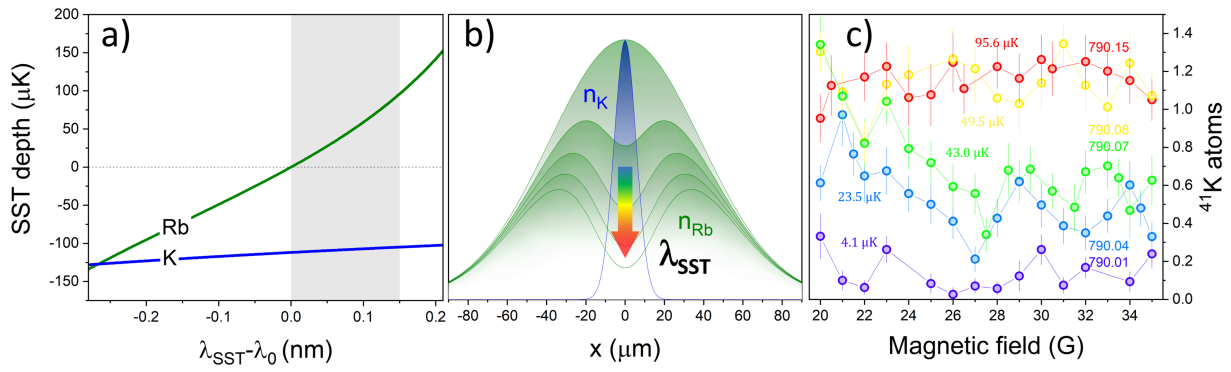

Figure 7.9: Controlling the interaction with the SST wavelength. a) For Rb, the SST potential is attractive (repulsive) at wavelengths below (above) $\lambda_0 = 790$ nm. For K, the SST potential is always attractive and not significantly modified around λ_0. The grey shaded area indicates the wavelengths utilised in this work. b) By tuning the wavelength of the SST across λ_0, we can control the density of Rb in the tweezer volume. The plotted density distributions are evaluated for different values of λ_{SST} (see Figure 7.4). c) Number of K atoms remaining in the SST after 50 ms as a function of the magnetic field, for different values of λ_{SST}, accompanied by the Rb trap depth. The temperature of the Rb sample is 1 μK. Each data point is the average over 30 experimental repetitions, and the error bars are the standard deviation of the mean.

change in wavelength does not affect the K potential. We instead observe that the width of the features in general increases for lower wavelength. This is a saturation effect due to the overall lower number of remaining K atoms. By increasing the wavelength, the contrast of the loss features first increases, and then decreases again when the scattering rate vanishes. For $\lambda_{SST} \geq 790.1$ nm, we are not able to detect any loss features at this interaction time.

To characterize the way the quantum impurity interacts with the thermal bath, we measure the thermalisation rate for different values of the SST wavelength for a fixed value of the magnetic field of 30 G. For this set of measurements $T_{Rb} \simeq 1$ μK. As described earlier, before being immersed in the Rb cloud, the temperature of the K atoms in the tweezer is $T_K \simeq 20\,\mu$K. As reported in Figure 7.10 (a), we observe that, once immersed, the temper-

ature of the K atoms decreases exponentially until it reaches the temperature of the bath. This can be seen by looking at the thermalisation rate $\Gamma = \Gamma_{KRb}/\xi$ using Equations 2.13 and 2.14 from Section 2.3.

To estimate the required number of collisions to thermalise, ξ, we utilise Monte Carlo simulations that take into account the quantization of the degrees of freedom of the K atom [72]. For our set of parameters, we obtain $\xi \simeq 12$. In Figure 7.10 (b) we report the thermalisation time constant $1/\Gamma$ obtained from exponential fits of the curves in Figure 7.10 (a). We observe that $1/\Gamma$ increases exponentially with λ_{SST}. This is expected, because the integral in Equation 2.14 decreases exponentially with λ_{SST}, while ξ remains constant since the initial and final temperatures do not vary. We fit our data with Equation 2.14, calculated using the theoretical value of $a_{eff}^{(0)}$ at 30 G, which is $0.7 l_{yz}$, leaving ξ as free parameter. With this procedure, we find that $\xi = 17.5 \pm 5$, which agrees with the value calculated with the Monte Carlo simulations.

For the same set of parameters, together with thermalisation, we observe losses of K atoms as they interact with the Rb bath. We have indeed used these losses to detect the resonances in Figure 7.5 and Figure 7.9. In our system, three-body losses could occur through two channels, namely KKRb and KRbRb. The rate equation for the K density can be seen in Equation 2.15 It was stated that, because we only have $\simeq 1$ K atom in our system, we expect the first term in Equation 2.15 to be negligible. This can be verified by fitting the decay of the number of K atoms, shown in Figure 7.10 (c) with the non-exponential solution of $\dot{n}_K = -2\alpha_{KKRb} n_K^2 n_{Rb}$. In our case, such a procedure delivers unphysical results. Our data are instead well-fitted by an exponential decay, for which we conclude that the second term in Equation 2.15 is the dominant contribution for our atom losses. This is further confirmed by the quadratic dependence of the decay constant $1/K_3 = 1/(\alpha_{KRbRb}\tilde{n}_{Rb}^2)$ on λ_{SST}, shown in Figure 7.10 (d). Indeed, across λ_0, the Rb potential grows approximately linearly, therefore $\tilde{n}_{Rb}$ decreases linearly, implying the quadratic growth of $1/K_3$. The quadratic dependence

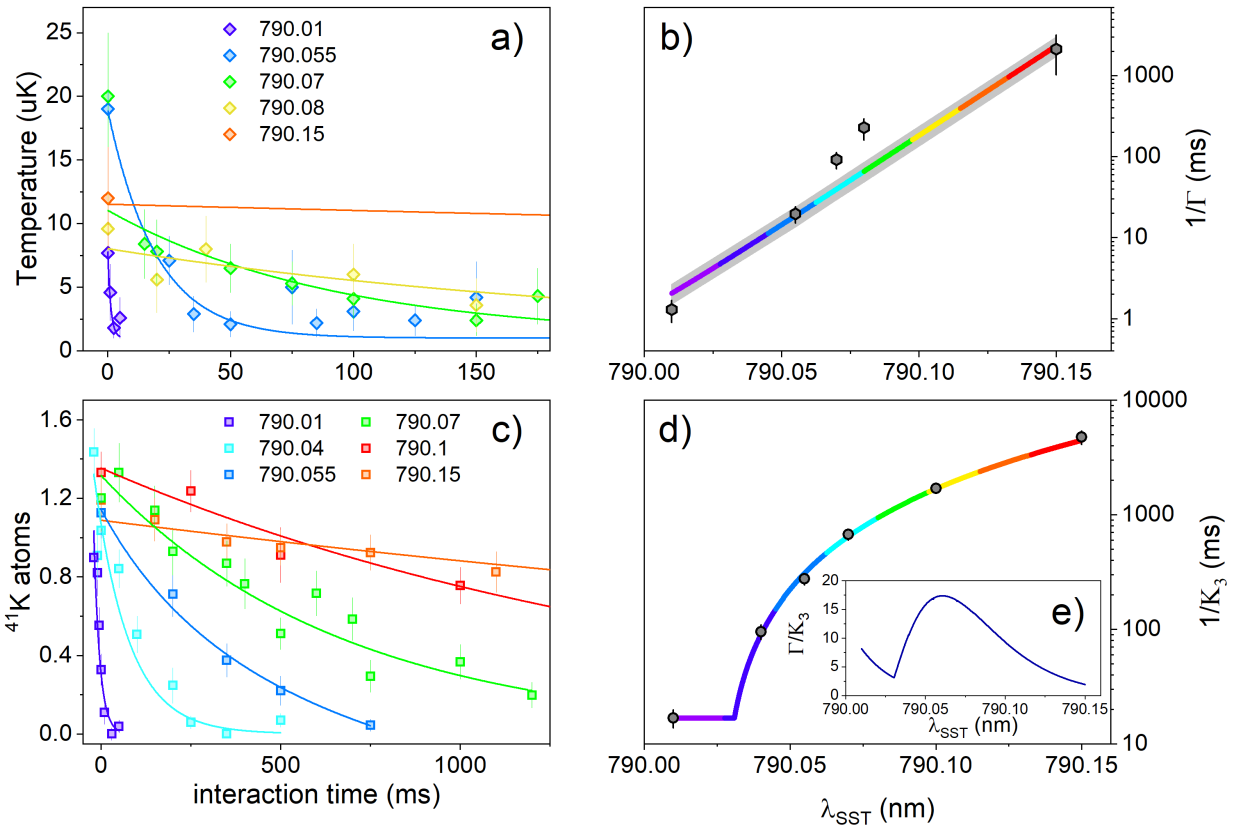

Figure 7.10: a) Temperature of the K atom in the SST as a function of the interaction time with the Rb bath, for different wavelengths of the SST. The magnetic field is set to 30 G, the starting temperature of the K atoms is $\simeq 20$ μK, the bath is composed of 10^5 Rb atoms at 1 μK. The K temperatures and relative error bars have been estimated with release-recapture thermometry and utilizing a Bayesian estimator [71]. Each data point corresponds to 180 experimental repetitions. The solid lines are exponential fits to the data with fixed asymptotic temperature of 1 μK. Most of the data points for $\lambda_{SST} = 790.15$ nm are outside the range displayed. For the full set of data, see Figure 7.11. b) thermalisation time $1/\Gamma$ for K atoms as a function of the SST wavelength. The values of $1/\Gamma$ and the error bars are resulting from fitting the curves in panel a) with exponential decays. The solid line is a fit using Equation 2.14 with our experimental parameters, leaving ξ as free parameter. The grey shaded area accounts for the error in the determination of ξ. c) Number of K atoms trapped in the SST as a function of the interaction time with a bath of 10^5 Rb atoms at 1 μK at 30 G. Each data point corresponds to 30 experimental repetitions. The error bars are the standard deviation of the mean. The solid lines are exponential fits to the data with 0 as the asymptote. d) Three-body loss rate K_3 for the K atoms in the SST as a function of λ_{SST}. The values of $1/K_3$ and the error bars result from fitting the curves in panel (c) with exponential decays. The solid line is a fit to the data with the maximum between a parabolic function and a lower threshold. e) Ratio between Γ and K_3 evaluated as the ratio between the solid curves in (b) and (d).

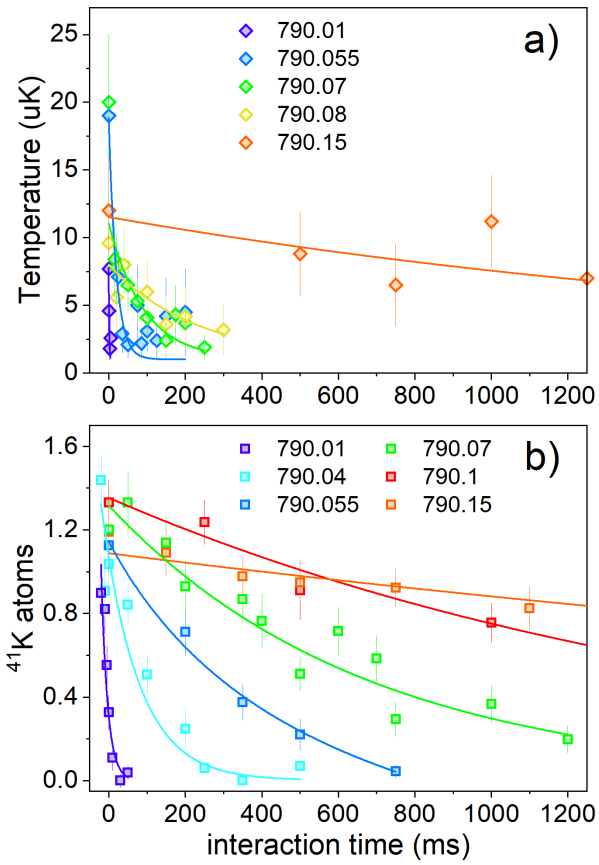

Figure 7.11: The same as Figure 7.10 (a) and (c), but displaying up to 1.2 seconds of interaction time.

breaks down for lower values of λ_{SST}, closer to λ_0, where the three-body loss rate K_3 saturates. This contributes to ensuring that, in our range of operation, the thermalisation rate is always larger than the three-body loss rate, up to more than one order of magnitude, as shown in Figure 7.10 (e). This is a crucial ingredient for achieving thermalisation. For this set of parameters, the optimal wavelength for efficient thermalisation is therefore $\simeq 790.06\,\text{nm}$, corresponding to thermalisation time scales of tens of ms. If faster thermalisation rates are desired, the optimal conditions are achieved by further blue detuning λ_{SST}, exploiting the saturation of the three-body loss rate K_3. This regime is of particular interest for the generation of trapped atomic dressed states like polarons, where strong repulsive interactions could counteract the strong attraction from the SST.

In summary, in the region of parameters that we have investigated, we demonstrated the ability to use the wavelength of the SST to vary the thermalisation rate of the quantum impurity system in the $\Gamma \simeq (1 \rightarrow 5 \times 10^{-4})$ s^{-1} range and, accordingly, the three-body collision rate in the $K_3 \simeq (0.05 \rightarrow 2 \times 10^{-4})$ s^{-1} range. This translates as the ability to tune the screening of the single atom quantum impurity over a broad range, up to completely decoupling the single atom and the bath.

7.4 Conclusions

In this work, we have demonstrated the implementation of a cold atom quantum impurity system by trapping a single K atom in an optical tweezer and immersing it in a cloud of ultracold Rb atoms. We have developed an experimental procedure that allows us to engineer all the parameters of the system, combining optical tweezer techniques with standard ultracold gas methods. We achieved selective manipulation of the quantum impurity and the bath by realizing the optical tweezer with laser light tuned close to λ_0. We have shown that with this experimental architecture it is possible to fully control the interactions between the impurity and the bath acting on three parameters: the external magnetic field, the dimensionality of the motion of the K atom, and the wavelength of the SST.

We performed Feshbach spectroscopy measuring the survival probability of the K atom in the bath as a function of the external magnetic field, detecting several loss features in the 1D-3D regime. We have used a theory including all the experimental parameters, that allowed us to associate the observed loss features to interdimensional Feshbach resonances. We detected two series of resonances, namely s-wave and p-wave, stemming from the underlying free-space s-wave Feshbach resonance. By lowering the temperature, we changed the dimensionality of the motion of the K atom from 1D to 0D. That in turn resulted in the appearance of additional narrow resonances linked to the finer energy level spacing along the weak axis of

the SST. As a result, our measurements and characterization enable the control of the H_{IB} term in Equation 1.1 using the external magnetic field and the dimensionality of the system.

We have shown that the wavelength of the SST can be used to screen the K atom from the atoms in the bath, down to almost completely decoupling them. Above λ_0, the SST becomes increasingly repulsive for the Rb atoms in the bath, and we demonstrated that this leads to an exponential decrease of the elastic scattering rate Γ. We have shown that the three-body loss rate K_3 instead scales quadratically, and that it is always lower than Γ, allowing the achievement of thermalisation in our system over the whole range of parameters explored. We finally discussed that due to the different scaling of K_3 and Γ, there exists an optimal value of the SST wavelength where the Γ/K_3 ratio is maximum and non-hermitian effects are minimized. The tuning of the wavelength of the SST enables a greater degree of control over H_{IB}, notably decoupling the quantum impurity and the bath.

Our work provides crucial elements for the implementation of pristine quantum simulators of quantum impurity models, like the spin-boson model and the Anderson impurity model, where the coupling between the impurity and the bath can be controlled and engineered. Our experimental architecture complements the features of systems like [138, 139], and lends itself to the engineering of open quantum systems, in particular to the realization of environmental dark states, and the manipulation and control of qubits using the environment [56, 57]. All this can have practical applications in quantum information protocols [58–60].

Particularly appealing is the possibility of studying thermodynamics in the quantum regime, more specifically the implementation of single atom quantum engines [6–8], where also the bath can be used as a quantum resource [2, 9, 12, 14], and advanced techniques like shortcuts to equilibration/thermalisation/adiabaticity can further suppress losses [140–142]. In this context, the quantification of the energy cost of quantum technologies is becoming a pressing issue [143]. Our platform could help in the understanding of how to efficiently manage the energy consumption in the quantum regime by acting on the interactions between

the quantum system and the environment. Finally, there is huge potential in extending our methods to tweezer arrays [144, 145], in which the interactions between the single trapped atoms and the common bath could be individually and collectively tuned. This could lead to the creation of environmental resilient many-body entangled states [146–148], the study of bath mediated interactions [149], thermal machines reaching quantum supremacy [150], and novel quantum computation architectures [151].

Chapter 8

Conclusions and Closing Remarks

In this thesis, I have presented and discussed the apparatus that I have built upon and how I used it to explore the area of quantum thermodynamics. The apparatus is capable of producing Bose-Einstein condensates of ^{87}Rb and cold samples of ^{41}K. Following on from the work of the previous PhD students, I have been able to optimise an optical tweezer in order to trap a single ^{41}K atom.

I reported on my successful collaboration with the University of Exeter, where new temperature methods were developed using Bayesian global thermometry techniques. We used our experimental setup consisting of a single ^{41}K atom at μK temperatures tightly confined in an optical tweezer, and performed release-recapture measurements. The conventional least squares method samples the fraction of recaptured atoms evenly across all recapture times evenly, then fits the data to a model of recapture probability. We combined both the experimental data I took with numerical simulations to show that the new methods have three key advantages. Firstly, the variability of estimates extracted from small data sets is largely reduced when compared to the conventional least squares method, leading to more dependable thermometry. Secondly, finding an optimal time leads to a faster convergence towards the true temperature in the asymptotic limit of many measurements. Finally, the

optimisation of the recapture time greatly reduces the number of measurements we need to take for the estimates to stabilise to a final temperature reading. Alternatively, you can view the conventional method as wasting resources by taking and processing numerous uninformative measurements. This was the method being used in the experiment prior to this study. For our experiment, time is an expensive resource, as we need to take a large amount of measurements to find a single temperature. The best temperature results were found using a fully adaptive method, where each release time takes into account all of the previous measurements. Although, we found that an *a priori* optimal protocol could compete with its results. This is desirable as it is quite simple to implement experimentally. One key feature of this work is that the fundamental principles can be applied to other techniques in other temperature ranges on a variety of experiments. As for ongoing applications for these techniques in our experiment, we've since applied the unoptimised Bayesian strategy to our thermalisation data seen in Section 7.3. The *a priori* optimal time method has also been tested, yet has not been displayed within this thesis. The key reason for this is that taking data using the unoptimised Bayesian method may take more actual time, but less user time due to easier data automation. On the other hand, the *a priori* method requires consistent user attention, when taking thermalisation data. Many temperatures need to be taken, and for each temperature, an optimal release time must be found.

I have also shown my exploration of a cold atom quantum impurity system, by looking into the interactions between an ultracold bath of ^{87}Rb atoms and a single ^{41}K atom. I developed an experimental procedure where it's possible to fully control the interactions between the impurity and the bath. This is done mainly through three key parameters, the external magnetic field, the dimensionality of motion of the K atom and the wavelength of the optical tweezer. I first performed Feshbach spectroscopy in the 1D-3D regime, measuring the K atom survival probability, and detecting both s-wave and p-wave resonances. Additional narrow resonances were found when looking at the 0D-3D regime. The wavelength of the SST was also used to control the interactions, being able to screen the K atom from the

atoms in the bath. I used this to achieve thermalisation in the system at a wide variety of parameters. This shows we have control over the Hamiltonian between the bath and the impurity, H_{IB}, using the external magnetic field, the system's dimensionality and the SST wavelength. Indeed, the implementation of a single atom quantum heat engine was the initial goal of this entire project, but the presence of more resonance features than expected will force us to be more resourceful if we wish to continue down this route. Another route would be to use an array of tweezers, where we study the interactions between the single trapped atoms and a common bath. The system built here is incredibly flexible, so a multitude of experiments are certainly possible.

Bibliography

[1] D Frese et al. "Single atoms in an optical dipole trap: Towards a deterministic source of cold atoms". In: *Physical review letters* 85.18 (2000), p. 3777.

[2] Hai-Tao Quan et al. "Quantum thermodynamic cycles and quantum heat engines". In: *Physical Review E* 76.3 (2007), p. 031105.

[3] Haitao T Quan. "Quantum thermodynamic cycles and quantum heat engines. II." In: *Physical Review E* 79.4 (2009), p. 041129.

[4] Sai Vinjanampathy and Janet Anders. "Quantum thermodynamics". In: *Contemporary Physics* 57.4 (2016), pp. 545–579.

[5] Ronnie Kosloff and Amikam Levy. "Quantum heat engines and refrigerators: Continuous devices". In: *Annual Review of Physical Chemistry* 65 (2014), pp. 365–393.

[6] Giovanni Barontini and Mauro Paternostro. "Ultra-cold single-atom quantum heat engines". In: *New Journal of Physics* 21.6 (2019), p. 063019.

[7] Johannes Roßnagel et al. "A single-atom heat engine". In: *Science* 352.6283 (2016), pp. 325–329.

[8] Quentin Bouton et al. "A quantum heat engine driven by atomic collisions". In: *Nature Communications* 12.1 (2021), p. 2063.

[9] Raam Uzdin, Amikam Levy, and Ronnie Kosloff. "Equivalence of quantum heat machines, and quantum-thermodynamic signatures". In: *Physical Review X* 5.3 (2015), p. 031044.

[10] J. Roßnagel et al. "Nanoscale Heat Engine Beyond the Carnot Limit". In: *Phys. Rev. Lett.* 112 (3 Jan. 2014), p. 030602.

[11] Lídia del Rio et al. "The thermodynamic meaning of negative entropy". In: *Nature* 474.7349 (2011), pp. 61–63.

[12] Marlan O Scully et al. "Extracting work from a single heat bath via vanishing quantum coherence". In: *Science* 299.5608 (2003), pp. 862–864.

[13] Raoul Dillenschneider and Eric Lutz. "Energetics of quantum correlations". In: *Europhysics Letters* 88.5 (2009), p. 50003.

[14] A del Campo, John Goold, and Mauro Paternostro. "More bang for your buck: Superadiabatic quantum engines". In: *Scientific Reports* 4.1 (2014), p. 6208.

[15] Jennifer Koch et al. "A quantum engine in the BEC–BCS crossover". In: *Nature* 621.7980 (2023), pp. 723–727.

[16] J-W Zhang et al. "Dynamical control of quantum heat engines using exceptional points". In: *Nature Communications* 13.1 (2022), p. 6225.

[17] Tim Langen et al. "Local emergence of thermal correlations in an isolated quantum many-body system". In: *Nature Physics* 9.10 (2013), pp. 640–643.

[18] Tim Langen, Remi Geiger, and Jörg Schmiedmayer. "Ultracold atoms out of equilibrium". In: *Annu. Rev. Condens. Matter Phys.* 6.1 (2015), pp. 201–217.

[19] Quentin Bouton et al. "Single-atom quantum probes for ultracold gases boosted by nonequilibrium spin dynamics". In: *Physical Review X* 10.1 (2020), p. 011018.

[20] Wolfgang Niedenzu et al. "Quantized refrigerator for an atomic cloud". In: *Quantum* 3 (2019), p. 155.

[21] Sepehr Ebadi et al. “Quantum phases of matter on a 256-atom programmable quantum simulator”. In: *Nature* 595.7866 (2021), pp. 227–232.

[22] Pascal Scholl et al. “Quantum simulation of 2D antiferromagnets with hundreds of Rydberg atoms”. In: *Nature* 595.7866 (2021), pp. 233–238.

[23] Friedhelm Serwane et al. “Deterministic preparation of a tunable few-fermion system”. In: *Science* 332.6027 (2011), pp. 336–338.

[24] Adam M Kaufman, Brian J Lester, and Cindy A Regal. “Cooling a single atom in an optical tweezer to its quantum ground state”. In: *Physical Review X* 2.4 (2012), p. 041014.

[25] G Li et al. “Crossed vortex bottle beam trap for single-atom qubits”. In: *Optics letters* 37.5 (2012), pp. 851–853.

[26] Steven Chu et al. “Three-dimensional viscous confinement and cooling of atoms by resonance radiation pressure”. In: *Physical review letters* 55.1 (1985), p. 48.

[27] Paul D Lett et al. “Observation of atoms laser cooled below the Doppler limit”. In: *Physical review letters* 61.2 (1988), p. 169.

[28] M Mudrich et al. “Sympathetic cooling with two atomic species in an optical trap”. In: *Physical review letters* 88.25 (2002), p. 253001.

[29] F Binder et al. *Thermodynamics in the Quantum Regime: Fundamental Aspects and New Directions*. Springer International Publishing, 2018, p. 503.

[30] Mohammad Mehboudi, Anna Sanpera, and Luis A Correa. “Thermometry in the quantum regime: recent theoretical progress”. In: *Journal of Physics A: Mathematical and Theoretical* 52.30 (2019), p. 303001.

[31] Samuel L Braunstein and Carlton M Caves. “Statistical distance and the geometry of quantum states”. In: *Physical Review Letters* 72.22 (1994), p. 3439.

[32] Carl W Helstrom. "Quantum detection and estimation theory". In: *Journal of Statistical Physics* 1 (1969), pp. 231–252.

[33] Edwin T Jaynes. *Probability theory: The logic of science*. Cambridge university press, 2003.

[34] Udo Von Toussaint. "Bayesian inference in physics". In: *Reviews of Modern Physics* 83.3 (2011), p. 943.

[35] Marcin Płodzień, Rafał Demkowicz-Dobrzański, and Tomasz Sowiński. "Few-fermion thermometry". In: *Physical Review A* 97.6 (2018), p. 063619.

[36] Mark T Mitchison et al. "In situ thermometry of a cold fermi gas via dephasing impurities". In: *Physical Review Letters* 125.8 (2020), p. 080402.

[37] Mohammad Mehboudi et al. "Using polarons for sub-nk quantum nondemolition thermometry in a bose-einstein condensate". In: *Physical review letters* 122.3 (2019), p. 030403.

[38] KDB Higgins et al. "Superabsorption of light via quantum engineering". In: *Nature communications* 5.1 (2014), p. 4705.

[39] Mohammad Mehboudi et al. "Thermometry precision in strongly correlated ultracold lattice gases". In: *New Journal of Physics* 17.5 (2015), p. 055020.

[40] Jesús Rubio. "Quantum scale estimation". In: *Quantum Science and Technology* 8.1 (2022), p. 015009.

[41] Thomas Hewitt et al. "Controlling the interactions in a cold atom quantum impurity system". In: *Quantum Science and Technology* 9.3 (2024), p. 035039.

[42] Philip Warren Anderson. "Localized magnetic states in metals". In: *Physical Review* 124.1 (1961), p. 41.

[43] Ferdinand Evers and Alexander D Mirlin. "Anderson transitions". In: *Reviews of Modern Physics* 80.4 (2008), p. 1355.

[44] Jun Kondo. "Resistance minimum in dilute magnetic alloys". In: *Progress of Theoretical Physics* 32.1 (1964), pp. 37–49.

[45] Kenneth G Wilson. "The renormalization group: Critical phenomena and the Kondo problem". In: *Reviews of Modern Physics* 47.4 (1975), p. 773.

[46] Anthony J Leggett et al. "Dynamics of the dissipative two-state system". In: *Reviews of Modern Physics* 59.1 (1987), p. 1.

[47] Ronald Hanson et al. "Spins in few-electron quantum dots". In: *Reviews of Modern Physics* 79.4 (2007), p. 1217.

[48] Stephanie M Reimann and Matti Manninen. "Electronic structure of quantum dots". In: *Reviews of Modern Physics* 74.4 (2002), p. 1283.

[49] Johannes Bauer, Christophe Salomon, and Eugene Demler. "Realizing a Kondo-correlated state with ultracold atoms". In: *Physical Review Letters* 111.21 (2013), p. 215304.

[50] Juliette Billy et al. "Direct observation of Anderson localization of matter waves in a controlled disorder". In: *Nature* 453.7197 (2008), pp. 891–894.

[51] Giacomo Roati et al. "Anderson localization of a non-interacting Bose–Einstein condensate". In: *Nature* 453.7197 (2008), pp. 895–898.

[52] Felix Schmidt et al. "Quantum spin dynamics of individual neutral impurities coupled to a Bose-Einstein condensate". In: *Physical Review Letters* 121.13 (2018), p. 130403.

[53] André Schirotzek et al. "Observation of Fermi polarons in a tunable Fermi liquid of ultracold atoms". In: *Physical Review Letters* 102.23 (2009), p. 230402.

[54] Christoph Zipkes et al. "A trapped single ion inside a Bose–Einstein condensate". In: *Nature* 464.7287 (2010), pp. 388–391.

[55] Takeshi Fukuhara et al. "Quantum dynamics of a mobile spin impurity". In: *Nature Physics* 9.4 (2013), pp. 235–241.

[56] Frank Verstraete, Michael M Wolf, and J Ignacio Cirac. "Quantum computation and quantum-state engineering driven by dissipation". In: *Nature Physics* 5.9 (2009), pp. 633–636.

[57] Markus Müller et al. "Engineered open systems and quantum simulations with atoms and ions". In: *Advances in Atomic, Molecular, and Optical Physics*. Vol. 61. Elsevier, 2012, pp. 1–80.

[58] John Goold et al. "The role of quantum information in thermodynamics—a topical review". In: *Journal of Physics A: Mathematical and Theoretical* 49.14 (2016), p. 143001.

[59] Robert Alicki et al. "Thermodynamics of quantum information systems—Hamiltonian description". In: *Open Systems & Information Dynamics* 11 (2004), pp. 205–217.

[60] Daniel Loss and David P DiVincenzo. "Quantum computation with quantum dots". In: *Physical Review A* 57.1 (1998), p. 120.

[61] Sai Vinjanampathy and Janet Anders. "Quantum thermodynamics". In: *Contemporary Physics* 57.4 (2016), pp. 545–579. DOI: 10.1080/00107514.2016.1201896.

[62] Jeffrey Douglas Thompson et al. "Coherence and Raman sideband cooling of a single atom in an optical tweezer". In: *Physical review letters* 110.13 (2013), p. 133001.

[63] Oliver Morsch and Markus Oberthaler. "Dynamics of Bose-Einstein condensates in optical lattices". In: *Reviews of Modern Physics* 78 (1 Feb. 2006), pp. 179–215.

[64] Immanuel Bloch, Jean Dalibard, and Wilhelm Zwerger. "Many-body physics with ultracold gases". In: *Reviews of Modern Physics* 80 (3 July 2008), pp. 885–964.

[65] Cheng Chin et al. "Feshbach resonances in ultracold gases". In: *Reviews of Modern Physics* 82.2 (2010), p. 1225.

[66] Thorsten Köhler, Krzysztof Góral, and Paul S Julienne. "Production of cold molecules via magnetically tunable Feshbach resonances". In: *Reviews of Modern Physics* 78.4 (2006), p. 1311.

[67] J Catani et al. "Entropy exchange in a mixture of ultracold atoms". In: *Physical Review Letters* 103.14 (2009), p. 140401.

[68] Cheng Sheng et al. "Defect-free arbitrary-geometry assembly of mixed-species atom arrays". In: *Physical Review Letters* 128.8 (2022), p. 083202.

[69] Jorge Mellado Muñoz. "Non-equilibrium quantum thermodynamics in ultracold atomic mixtures". In: *University of Birmingham* (2020).

[70] Jorge Mellado Muñoz et al. "Dissipative distillation of supercritical quantum gases". In: *Physical Review Letters* 125.2 (2020), p. 020403.

[71] Jonas Glatthard et al. "Optimal cold atom thermometry using adaptive bayesian strategies". In: *PRX quantum* 3.4 (2022), p. 040330.

[72] Rahul Sawant, Anna Maffei, and Giovanni Barontini. "Thermalization of a trapped single atom with an atomic thermal bath". In: *Applied Sciences* 11.5 (2021), p. 2258.

[73] Gregory Breit and Isidor Issac Rabi. "Measurement of nuclear spin". In: *Physical Review* 38.11 (1931), p. 2082.

[74] Temo Vekua. "Breit-Rabi diagram for alkali-metal atoms". In: *MATLAB Central File Exchange* (2025).

[75] Andrea Simoni et al. "Magnetic control of the interaction in ultracold K-Rb mixtures". In: *Physical review letters* 90.16 (2003), p. 163202.

[76] G Ferrari et al. "Collisional properties of ultracold K-Rb mixtures". In: *Physical Review Letters* 89.5 (2002), p. 053202.

[77] Andrea Simoni et al. "Near-threshold model for ultracold KRb dimers from interisotope Feshbach spectroscopy". In: *Physical Review A* 77.5 (2008), p. 052705.

[78] Francesca Ferlaino et al. "Feshbach spectroscopy of a K-Rb atomic mixture". In: *Physical Review A—Atomic, Molecular, and Optical Physics* 73.4 (2006), p. 040702.

[79] G Thalhammer et al. "Double species Bose-Einstein condensate with tunable interspecies interactions". In: *Physical review letters* 100.21 (2008), p. 210402.

[80] Pietro Massignan and Yvan Castin. "Three-dimensional strong localization of matter waves by scattering from atoms in a lattice with a confinement-induced resonance". In: *Physical Review A* 74.1 (2006), p. 013616.

[81] G Lamporesi et al. "Scattering in mixed dimensions with ultracold gases". In: *Physical Review Letters* 104.15 (2010), p. 153202.

[82] Yusuke Nishida and Shina Tan. "Universal Fermi gases in mixed dimensions". In: *Physical review letters* 101.17 (2008), p. 170401.

[83] Yusuke Nishida and Shina Tan. "Confinement-induced p-wave resonances from s-wave interactions". In: *Physical Review A* 82.6 (2010), p. 062713.

[84] Luís Gustavo Marcassa et al. "Collisional losses in a K-Rb cold mixture". In: *Physical review A* 63.1 (2000), p. 013413.

[85] Eric A. Cornell, Jason R. Ensher, and Carl E. Wieman. *Experiments in Dilute Atomic Bose-Einstein Condensation*. 1999. arXiv: `cond-mat/9903109 [cond-mat]`.

[86] A Guttridge et al. "Interspecies thermalization in an ultracold mixture of Cs and Yb in an optical trap". In: *Physical Review A* 96.1 (2017), p. 012704.

[87] Maciej Lewenstein, J Ignacio Cirac, and Peter Zoller. "Master equation for sympathetic cooling of trapped particles". In: *Physical Review A* 51.6 (1995), p. 4617.

[88] T Papenbrock, AN Salgueiro, and HA Weidenmüller. "Rate equations for sympathetic cooling of trapped bosons or fermions". In: *Physical Review A* 65.4 (2002), p. 043601.

[89] Jesús Rubio, Janet Anders, and Luis A Correa. "Global quantum thermometry". In: *Physical review letters* 127.19 (2021), p. 190402.

[90] Edwin T Jaynes. "Prior probabilities". In: *IEEE Transactions on systems science and cybernetics* 4.3 (1968), pp. 227–241.

[91] Rafał Demkowicz-Dobrzański, Wojciech Górecki, and Mădălin Guţă. "Multi-parameter estimation beyond quantum Fisher information". In: *Journal of Physics A: Mathematical and Theoretical* 53.36 (2020), p. 363001.

[92] Harrison Bertrand Prosper. "Temperature fluctuations in a heat bath". In: *American journal of physics* 61.1 (1993), pp. 54–58.

[93] Harold Jeffreys. *The theory of probability*. OuP Oxford, 1998.

[94] Cherif F Matta et al. "Can one take the logarithm or the sine of a dimensioned quantity or a unit? Dimensional analysis involving transcendental functions". In: *Journal of Chemical Education* 88.1 (2011), pp. 67–70.

[95] Daniel A Steck. "Rubidium 87 D line data". In: (2001).

[96] TG Tiecke. "Properties of potassium". In: *University of Amsterdam, The Netherlands, Thesis* (2010), pp. 12–14.

[97] Daryl W Preston. "Doppler-free saturated absorption: Laser spectroscopy". In: *American Journal of Physics* 64.11 (1996), pp. 1432–1436.

[98] G Ritt et al. "Laser frequency offset locking using a side of filter technique". In: *Applied Physics B* 79 (2004), pp. 363–365.

[99] A Banerjee, D Das, and V Natarajan. "Absolute frequency measurements of the D1 lines in 39K, 85Rb, and 87Rb with 0.1 ppb uncertainty". In: *Europhysics Letters* 65.2 (2004), p. 172.

[100] Dipankar Das and Vasant Natarajan. "High-precision measurement of hyperfine structure in the D lines of alkali atoms". In: *Journal of Physics B: Atomic, Molecular and Optical Physics* 41.3 (2008), p. 035001.

[101] Christopher J Foot et al. *Atomic Physics, Volume 7*. Oxford University Press, 2005.

[102] Tomasz M Brzozowski et al. "Time-of-flight measurement of the temperature of cold atoms for short trap-probe beam distances". In: *Journal of Optics B: Quantum and Semiclassical Optics* 4.1 (2002), p. 62.

[103] K Dieckmann et al. "Two-dimensional magneto-optical trap as a source of slow atoms". In: *Physical Review A* 58.5 (1998), p. 3891.

[104] Wolfgang Ketterle et al. "High densities of cold atoms in a dark spontaneous-force optical trap". In: *Physical review letters* 70.15 (1993), p. 2253.

[105] CG Townsend et al. "High-density trapping of cesium atoms in a dark magneto-optical trap". In: *Physical Review A* 53.3 (1996), p. 1702.

[106] Rudolf Grimm, Matthias Weidemüller, and Yurii B Ovchinnikov. "Optical dipole traps for neutral atoms". In: *Advances in atomic, molecular, and optical physics* 42 (2000), pp. 95–170.

[107] Wolfgang Petrich et al. "Behavior of atoms in a compressed magneto-optical trap". In: *JOSA B* 11.8 (1994), pp. 1332–1335.

[108] Bernard Richards and Emil Wolf. "Electromagnetic diffraction in optical systems, II. Structure of the image field in an aplanatic system". In: *Proceedings of the Royal Society of London. Series A. Mathematical and Physical Sciences* 253.1274 (1959), pp. 358–379.

[109] SJM Kuppens et al. "Loading an optical dipole trap". In: *Physical review A* 62.1 (2000), p. 013406.

[110] Nicolas Schlosser, Georges Reymond, and Philippe Grangier. "Collisional blockade in microscopic optical dipole traps". In: *Physical review letters* 89.2 (2002), p. 023005.

[111] YH Fung and MF Andersen. "Efficient collisional blockade loading of a single atom into a tight microtrap". In: *New Journal of Physics* 17.7 (2015), p. 073011.

[112] Nicolas Schlosser et al. “Sub-poissonian loading of single atoms in a microscopic dipole trap”. In: *Nature* 411.6841 (2001), pp. 1024–1027.

[113] Nikolaus Lorenz et al. “Raman sideband cooling in optical tweezer arrays for Rydberg dressing”. In: *SciPost Physics* 10.3 (2021), p. 052.

[114] Jean Dalibard and Claude Cohen-Tannoudji. “Dressed-atom approach to atomic motion in laser light: the dipole force revisited”. In: *JOSA B* 2.11 (1985), pp. 1707–1720.

[115] Elmar Haller et al. “Single-atom imaging of fermions in a quantum-gas microscope”. In: *Nature Physics* 11.9 (2015), pp. 738–742.

[116] Nicholas R Hutzler et al. “Eliminating light shifts for single atom trapping”. In: *New Journal of Physics* 19.2 (2017), p. 023007.

[117] Ivaylo Sashkov Madjarov. *Entangling, controlling, and detecting individual strontium atoms in optical tweezer arrays*. California Institute of Technology, 2021.

[118] Alexander Albert Urech et al. “Single strontium atoms in optical tweezers”. PhD thesis. Alexander Albert Urech, 2023.

[119] Marcel Mudrich. “Interactions in an optically trapped mixture of ultracold Lithium and Cesium atoms: Thermalization, spin-exchange collosions and photoassociation”. PhD thesis. Dissertation, Ruprecht-Karls Universität Heidelberg, 2003.

[120] Samuel L Braunstein, Alistair S Lane, and Carlton M Caves. “Maximum-likelihood analysis of multiple quantum phase measurements”. In: *Physical review letters* 69.15 (1992), p. 2153.

[121] Rafal Demkowicz-Dobrzański, Marcin Jarzyna, and Jan Kołodyński. “Quantum limits in optical interferometry”. In: *Progress in Optics* 60 (2015), pp. 345–435.

[122] Jesús Rubio and Jacob Dunningham. “Quantum metrology in the presence of limited data”. In: *New Journal of Physics* 21.4 (2019), p. 043037.

[123] Jesús Rubio and Jacob Dunningham. "Bayesian multiparameter quantum metrology with limited data". In: *Physical Review A* 101.3 (2020), p. 032114.

[124] Jesús Rubio Jiménez. "Non-asymptotic quantum metrology: extracting maximum information from limited data". PhD thesis. University of Sussex, 2020.

[125] Michael Hohmann et al. "Single-atom thermometer for ultracold gases". In: *Physical Review A* 93.4 (2016), p. 043607.

[126] F Ruschewitz et al. "Statistical investigations on single trapped neutral atoms". In: *Europhysics Letters* 34.9 (1996), p. 651.

[127] D Haubrich et al. "Observation of individual neutral atoms in magnetic and magneto-optical traps". In: *Europhysics Letters* 34.9 (1996), p. 663.

[128] Felix Schmidt et al. "Precision measurement of the Rb 87 tune-out wavelength in the hyperfine ground state F= 1 at 790 nm". In: *Physical Review A* 93.2 (2016), p. 022507.

[129] H-J Miesner et al. "Observation of metastable states in spinor Bose-Einstein condensates". In: *Physical Review Letters* 82.11 (1999), p. 2228.

[130] M-S Chang et al. "Observation of spinor dynamics in optically trapped rb 87 bose-einstein condensates". In: *Physical review letters* 92.14 (2004), p. 140403.

[131] Yuki Kawaguchi and Masahito Ueda. "Spinor bose–einstein condensates". In: *Physics Reports* 520.5 (2012), pp. 253–381.

[132] Daniel Benedicto Orenes. "Realization of a spin-1 Bose-Einstein condensation experiment". PhD thesis. University of Birmingham, 2018.

[133] D. S. Petrov. "Three-Boson Problem near a Narrow Feshbach Resonance". In: *Physical Review Letters* 93 (14 Sept. 2004), p. 143201.

[134] J. Levinsen et al. "Atom-Dimer Scattering and Long-Lived Trimers in Fermionic Mixtures". In: *Physical Review Letters* 103 (15 Oct. 2009), p. 153202.

[135] Elmar Haller et al. "Confinement-induced resonances in low-dimensional quantum systems". In: *Physical Review Letters* 104.15 (2010), p. 153203.

[136] Deborah Capecchi et al. "Observation of confinement-induced resonances in a 3D lattice". In: *arXiv preprint arXiv:2209.12504* (2022).

[137] C Weber et al. "Association of ultracold double-species bosonic molecules". In: *Physical Review A* 78.6 (2008), p. 061601.

[138] Claudia Weber et al. "Single Cs atoms as collisional probes in a large Rb magneto-optical trap". In: *Phys. Rev. A* 82 (4 Oct. 2010), p. 042722. DOI: 10.1103/PhysRevA.82.042722. URL: https://link.aps.org/doi/10.1103/PhysRevA.82.042722.

[139] Nicolas Spethmann et al. "Dynamics of Single Neutral Impurity Atoms Immersed in an Ultracold Gas". In: *Phys. Rev. Lett.* 109 (23 Dec. 2012), p. 235301. DOI: 10.1103/PhysRevLett.109.235301. URL: https://link.aps.org/doi/10.1103/PhysRevLett.109.235301.

[140] Roie Dann, Ander Tobalina, and Ronnie Kosloff. "Shortcut to Equilibration of an Open Quantum System". In: *Phys. Rev. Lett.* 122 (25 June 2019), p. 250402. DOI: 10.1103/PhysRevLett.122.250402. URL: https://link.aps.org/doi/10.1103/PhysRevLett.122.250402.

[141] A Pedram et al. "A quantum Otto engine with shortcuts to thermalization and adiabaticity". In: *New Journal of Physics* 25.11 (Nov. 2023), p. 113014. DOI: 10.1088/1367-2630/ad0857. URL: https://dx.doi.org/10.1088/1367-2630/ad0857.

[142] Mohamed Boubakour et al. *Dynamical invariant based shortcut to equilibration.* 2024. arXiv: 2401.11659 [quant-ph].

[143] Alexia Auffeves. "Quantum technologies need a quantum energy initiative". In: *PRX Quantum* 3.2 (2022), p. 020101.

[144] Manuel Endres et al. "Atom-by-atom assembly of defect-free one-dimensional cold atom arrays". In: *Science* 354.6315 (2016), pp. 1024–1027.

[145] Daniel Barredo et al. “An atom-by-atom assembler of defect-free arbitrary two-dimensional atomic arrays”. In: *Science* 354.6315 (2016), pp. 1021–1023.

[146] Luigi Amico et al. “Entanglement in many-body systems”. In: *Reviews of Modern Physics* 80.2 (2008), p. 517.

[147] Dmitry A Abanin et al. “Colloquium: Many-body localization, thermalization, and entanglement”. In: *Reviews of Modern Physics* 91.2 (2019), p. 021001.

[148] Leandro Aolita, Fernando De Melo, and Luiz Davidovich. “Open-system dynamics of entanglement: a key issues review”. In: *Reports on Progress in Physics* 78.4 (2015), p. 042001.

[149] Thomas Zell, Friedemann Queisser, and Rochus Klesse. “Distance dependence of entanglement generation via a bosonic heat bath”. In: *Physical Review Letters* 102.16 (2009), p. 160501.

[150] Juan Jaramillo, Mathieu Beau, and Adolfo del Campo. “Quantum supremacy of many-particle thermal machines”. In: *New Journal of Physics* 18.7 (2016), p. 075019.

[151] Adam M Kaufman and Kang-Kuen Ni. “Quantum science with optical tweezer arrays of ultracold atoms and molecules”. In: *Nature Physics* 17.12 (2021), pp. 1324–1333.